

Dissertation zur Erlangung des Doktorgrades
der Fakultät für Chemie und Pharmazie
der Ludwig–Maximilians–Universität München

**Tip-Enhanced Near-Field Optical
Microscopy of Single-Walled Carbon
Nanotube/Polymer Conjugates and
Improvements of the Image Contrast**

von
Xian Shi
aus
Shenyang, Liaoning, China

2017

Erklärung

Diese Dissertation wurde im Sinne von §7 der Promotionsordnung vom 28. November 2011 von Herrn Prof. Dr. Achim Hartschuh betreut.

Eidesstattliche Versicherung

Diese Dissertation wurde eigenständig und ohne unerlaubte Hilfe erarbeitet.

München, den 13. November 2017

.....
(Xian Shi)

Dissertation eingereicht am: 13.11.2017
Erstgutachter: Prof. Dr. Achim Hartschuh
Zweitgutachter: Prof. Dr. Tobias Hertel
Mündliche Prüfung am 15.12.2017

Abstract

Semiconducting single-walled carbon nanotubes (s-SWCNTs) are regarded as a promising candidate for a wide range of applications. Particularly, tailored blends of single-walled carbon nanotubes with polymers are ideally suited for organic solar cells (OSC) due to their inherent stability, high carrier mobility and the tunability of optical band gaps. In the past, the mixing of semiconducting and metallic SWCNTs and their aggregation into bundles strongly hindered their practical applications. More recently, many techniques have been developed to separate SWCNTs into chirality-pure single carbon nanotube samples. Nowadays, the most common approach is non-covalent polymer or surfactant wrapping. However, the characterization of these SWCNT samples is usually limited to a macroscopic level and few studies have looked into the interaction between SWCNTs and the wrapping agent on the single nanotube level. A comparison of the effects of different wrapping agents could provide useful guideline for device fabrication.

Tip-enhanced near-field optical microscopy (TENOM) achieves 10 - 20 nm spatial resolution and substantial signal enhancement by employing an optical antenna such as a gold tip to localize and enhance light-matter interactions. In the first part of the thesis, we utilized TENOM to study the photoluminescence (PL) of single SWCNTs in different sample materials and investigated their optical heterogeneity. We introduced a statistical parameter to evaluate the intensity fluctuation of the near-field PL, which yields information on the occurrence of exciton trapping sites and quenching defects. We compared the results from different wrapping agents and post-synthesis treatment, and found that CVD-synthesized SWCNTs, without further treatment together with PFO-BPy as wrapping agent exhibits the highest level of optical homogeneity.

For TENOM and other types of scanning near-field optical microscopy (SNOM) as well, the presence of a far-field background from laser illumination of the sample lowers the signal to background ratio and decreases detection sensitivity. The second part of the thesis aims at suppressing the far-field background. We implemented a new tuning fork configuration in which the tip oscillates normal to the sample surface in a tuning-fork based TENOM setup, and drove an oscillation amplitude larger than the near-field decay length. A switch with a tunable threshold was used to extract the far-field part, which was subsequently subtracted from the total signal. Theoretical calculations were first performed to find the optimal tip modulation depth and switch threshold. The new configuration was finally applied to SWCNT PL imaging and was proven to significantly enhance the signal to background ratio.

Table of Contents

Abstract	v
0 Introduction	1
1 Single-walled carbon nanotubes	5
1.1 Basic Concepts and Physical Properties	5
1.1.1 Structure of SWCNT	5
1.1.2 Electronic Structure	9
1.1.3 Excitons and Photoluminescence	17
1.1.4 Raman Scattering of SWCNT	22
1.2 Applications of SWCNT in organic solar cells	27
1.2.1 Synthesis and sorting of SWCNT	27
1.2.2 SWCNT-based organic solar cells	28
2 Principles of TENOM	31
2.1 The diffraction limit derived by the angular spectrum representation	32
2.2 Principles of optical antennas	36
2.2.1 Characteristics of an optical antenna	36
2.2.2 Near-field of optical antennas	39
2.2.3 Gap plasmon mode	40
2.3 Signal enhancement	42
2.3.1 Signal enhancement based on electromagnetic field enhancement	43
2.3.2 Other proposed enhancement mechanisms	45
3 Experimental Approach	49
3.1 Sample Preparation	49
3.2 Experimental Setup	50
3.2.1 Confocal Microscope	50
3.2.2 Tip-enhanced near-field Optical Microscope	52
3.2.3 Gold tip fabrication	55
4 Near-field Optical Imaging of (6,5) SWCNT/Polymer Conjugates	57
4.1 Observation of Near-field PL intensity variations along SWCNTs	58

4.2	Statistical analysis of near-field PL heterogeneity of different SWCNT samples	61
4.3	Photo-induced defects and their influence on near-field PL	66
5	Near-field and far-field Separation via Tip-sample distance modulation	71
5.1	Near-field signal extraction using Lock-in amplifier	74
5.2	Far-field signal separation and subtraction exploiting tunable switch	77
5.2.1	Theoretical calculations	78
5.2.2	Experimental Realization	84
6	Summary and Outlook	87
	Appendix: Matlab Scripts	91
	Bibliography	94
	Acronyms	114
	List of Figures	118
	List of Publications	123
	List of Conferences	125
	Acknowledgements	126

Introduction

We are facing a global energy crisis. According to *Renewables 2016 Global Status Report*, we just witnessed the highest world's annual fossil fuel consumption in 2015 which takes up more than 80% of total energy usage. Even if we neglect the effect of our growing population, the detected oil and gas on earth will run out by 2060. Among renewable energy sources, solar energy has attracted much attention due to its huge amount (3.5 - 7.0 KWh/ m^2 per day) and cleanness. Nowadays, the mainstream solar energy panels are based on monocrystalline silicon, but their applications are limited by several issues such as the high cost for silicon purification. As a new kind of device, organic solar cells (OSC) feature several advantages over silicon solar cells: low cost, energy effective production, low weight and semi-transparency. This makes them apt for novel applications like, building-integrated photovoltaics (BIPV) with high market potential.

Semiconducting single-walled carbon nanotubes (s-SWCNTs) are regarded as a promising candidate for a wide range of applications, such as biological imaging[1], gene or drug delivery[2], energy storage[3], high-performance field effect transistors (FETs)[4], elements in telecommunication systems[5], molecular sensors[6] and so on. Moreover, tailored blends of single-walled carbon nanotubes with polymers have great potential for organic solar cells (OSC) due to their inherent stability, high carrier mobility and the tunability of optical band gaps. However, it's still challenging to control the chirality, aggregation, electronic energy alignment and nanoscale morphology of SWCNT samples, and researchers have not been able to manufacture profitable SWCNT-based OSCs with a satisfying efficiency and long-term stability yet.

Since their invention in early 17th century, optical microscope have been widely used to detect the optical properties of materials. While enormous progress in manufacturing of optical components has been made, all glass-based microscopes have an ultimate limit for spatial resolution, which origins from the diffraction of light and is therefore denoted as diffraction limit. In confocal laser scanning microscopy, the diffraction limit can be improved by reducing the excitation wavelength and exploiting an on objective lens with a larger numerical aperture (NA). Nevertheless, the best diffraction limited spatial resolution that can be achieved in this way is still a few hunderd nanometers, which is much larger than the size of single molecules or low dimensional nanostructures. This size mismatch prevents us from detailed investigations of nanomaterials and therefore must be overcome. Both far-field and near-field techniques have been developed to achieve this goal. The setup we use is named tip-enhanced near-field optical microscopy (TENOM) as

one of the near-field techniques. By employing the locally enhanced electric field at the apex of a sharp gold tip, 10 -20 nm spatial resolution and substantial signal enhancement could be realized[7]. TENOM has been applied to a variety of nanomaterials including single molecules[8], 0D nanomaterials such as quantum dots[9], 1D nanomaterials such as SWCNTs[10, 11] and inorganic semiconducting nanowires[12], 2D nanomaterials including graphene[13] and transition metal dichalcogenides (TMDCs)[14]. In addition, it is not only applicable to purely optical spectroscopy but also to photocurrent and electroluminescence detection[15].

The European initial training network POCAONTAS (Polymer-Carbon Nanotubes Active Systems for Photovoltaics) aimed at developing highly efficient and stable OSCs based on tailored blends of polymers with SWCNTs. It involves 14 research institutions and industrial partners all over Europe. The first three years of my PhD was sponsored by POCAONTAS. In this network we were responsible for nanoscale characterization and our main tasks included investigating: (1) the optical and structural heterogeneity of polymer wrapped SWCNT; (2) the influence of defects and quenching sites; (3) SWCNT-polymer interactions with the help of TENOM.

This thesis is structured as follows. The first section of Chapter 1 focuses on basic concepts and physical properties of SWCNT. Starting from the discussion of the electronic energy dispersion relation of graphene using the tight-binding approach, the band structure of SWCNTs is obtained from zone-folding. Afterwards, the optical response of SWCNTs - Raman scattering and photoluminescence (PL) is described and an emphasis is put on excitons and PL. Since the first part of the experimental work was conducted under the framework of POCAONTAS, in the second section we briefly review the development of SWCNT-based organic solar cells.

Chapter 2 describes the principles of tip-enhanced near-field optical microscopy (TENOM). Firstly we discuss the diffraction limit of conventional optical microscopy using the angular spectrum representation. Then we introduce the principles of optical antennas and describe the near-field distribution of them, which gives rise to sub-diffraction spatial resolution. The gap plasmon mode, with its stronger field confinement and improved spatial resolution, has attracted much attention in the past years. A short summary about its mechanism is given. Subsequently we describe the signal enhancement in near-field measurements. Here, the conventional model based on electromagnetic enhancement is briefly reviewed, and then a few recently proposed new mechanisms which could better explain the sub-nanometer resolution and substantially high enhancement in experimental works are addressed.

Chapter 3 is a summary of all the experimental approaches used in this thesis. The synthesis procedures of different SWCNT samples are presented in the first section. In the second section we start from the confocal microscope, which is the fundamental part of the TENOM setup. A sketch showing the excitation, detection path and all the optical elements is included. Following that we move to the additional features of TENOM, including the laser mode conversion, the scanning head, the tip-sample distance control by shear-force

feedback and shortly described how to align the tip position in x,y plane (tip centering). In the last section we introduce the fabrication and characterization of sharp gold tips used as optical antenna in TENOM.

Chapter 4 and 5 present the experimental results. Chapter 4 is related to the experimental work conducted under the framework of POCAONTAS. As-synthesized SWCNTs consist of a mixture of metallic and semiconducting ones, and they tend to aggregate into bundles. A large number of polymers and surfactants have been applied to sort the SWCNTs into chirality-pure single nanotube samples in the literature. We utilized TENOM with 10 - 20 nm spatial resolution and substantial signal enhancement to study the local PL along single wrapped SWCNTs in different samples. A statistical parameter was introduced to evaluate the optical heterogeneity of these nanotubes for the first time, which indicates the occurrence of exciton trapping sites. We then compared the results from different wrapping agents and different post-synthesis treatment, and found the combination exhibiting the highest level of optical homogeneity. In addition, defects are known to quench the PL of SWCNT and are detrimental to solar cell device performance. We generated photo-induced defects with high excitation power on single nanotubes and observed how these defects affect the near-field PL.

Chapter 5 addresses the question of how to suppress the far-field background and improve the signal to background ratio in TENOM. We implemented a new tuning fork configuration in which the tip oscillates normal to the sample surface in the TENOM setup and drove a large oscillation amplitude so that the far-field signal is much stronger than the remaining near-field signal during the upper part of the oscillation. In order to separate near-field and far-field contributions, we explored two methods, one using a lock-in amplifier and the other based on a tunable switch. It was found that the first method was valid only for high signal intensities, while the second is much more versatile due to the tunable threshold of the switch. Theoretical calculations were first performed to determine the optimal modulation depth and switch threshold. Subsequently, the new configuration was applied to SWCNT PL imaging and was proven to significantly enhance the signal to background ratio after far-field subtraction.

Finally, we summarize the most important experimental results in the thesis and give an outlook suggesting further investigations for the discussed subjects. The appendix contains the Matlab scripts for the theoretical calculations in chapter 5.

Chapter 1

Single-walled carbon nanotubes

Single-walled carbon nanotubes (referred to as SWCNTs from now on) are hollow cylinders of rolled-up graphene sheets. They were first discovered in 1993 [16]. Although it is already two decades ago, the research interest in its fundamental properties and exploitation through a huge number of applications never stopped due to their exceptional mechanical, optical, electronic and optoelectronic properties.

In this chapter, we first describe the geometric structure of carbon nanotubes and then obtain their band structure from the known graphene properties through the so-called zone-folding procedure. Afterwards, we introduce the two most important optical processes namely Raman scattering and Photoluminescence. Finally we give a review about SWCNT-based photovoltaic devices with an emphasis on recent developments in the last few years.

1.1 Basic Concepts and Physical Properties

1.1.1 Structure of SWCNT

SWCNTs can be regarded as seamless cylinders that are rolled up from a single narrow graphene ribbon. Fig. 1.1 shows how to construct a single nanotube from a graphene sheet. Obviously, there are many different rolling up directions with respect to the lattice, which will result in different structures and thus properties. The roll-up direction is characterized by the chiral vector \vec{C}_h , which can be expressed by the two graphene lattice vectors \vec{a}_1 and \vec{a}_2 as:

$$\vec{C}_h = n \cdot \vec{a}_1 + m \cdot \vec{a}_2 \quad (1.1)$$

Here the two positive integers n and m are called chiral indexes and (n,m) is commonly used to uniquely define a particular tube, known as the chirality. The graphene will be rolled in the way that the starting point of the vector meets the endpoint, in other words the length of \vec{C}_h is the circumference of the nanotube. Then we could easily calculate the

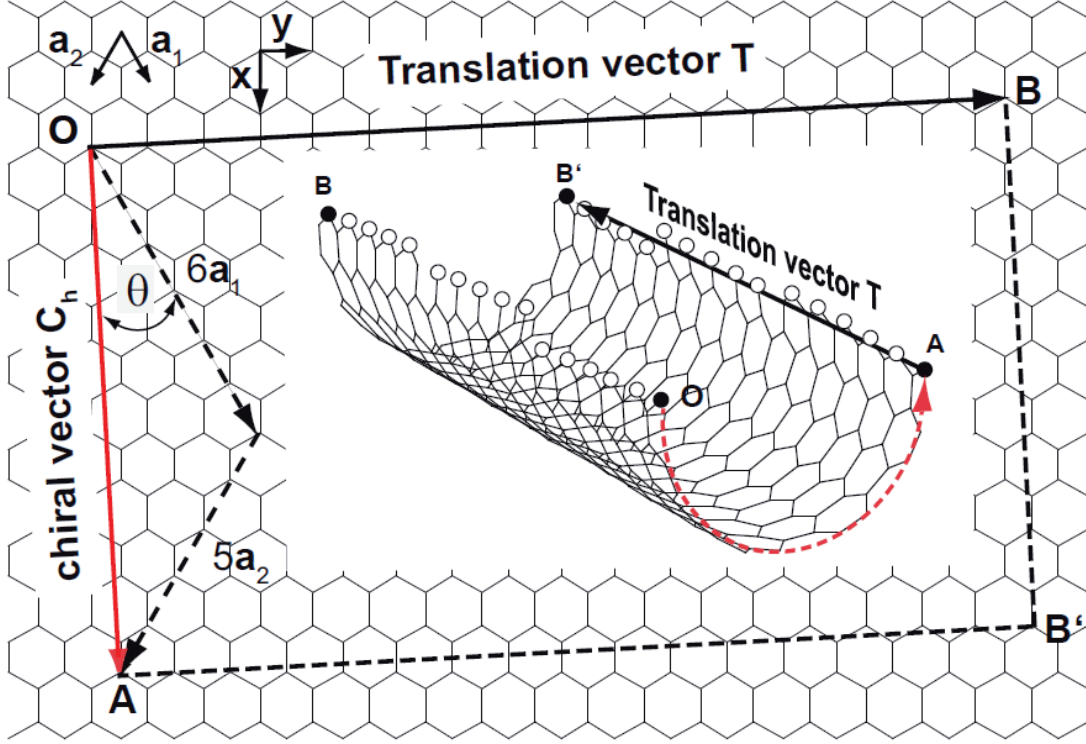


Figure 1.1: Construction of a (6,5) SWCNT unit cell by rolling up a rectangular stripe of graphene. The edges of the sheet are defined by the chiral vector \vec{C}_h and the translation vector \vec{T} perpendicular to \vec{C}_h . The chiral vector is defined by the graphene lattice vectors \vec{a}_1 and \vec{a}_2 . For the case of a (6,5) SWCNT: $\vec{C}_h = 6 \cdot \vec{a}_1 + 5 \cdot \vec{a}_2$. Rolling up the rectangular sheet, so that point O coincides with point A and point B with point B', resulting in the quasi-1D cylindrical unit cell of the SWCNT. Figure is generated from an online source[17].

nanotube diameter d :

$$d = \frac{|\vec{C}_h|}{\pi} = a \frac{\sqrt{n^2 + m^2 + nm}}{\pi} \quad (1.2)$$

The directional relation of the chiral vector \vec{C}_h to the graphene lattice vector \vec{a}_1 is defined by the chiral angle θ_{Ch} :

$$\theta_{Ch} = \arccos \frac{2n + m}{2\sqrt{n^2 + m^2 + nm}} \quad (1.3)$$

Due to the symmetry of the graphene 2D honeycomb lattice, (n,m) and (m,n) represent the same kind of nanotube. Thus all the possible chiralities can be described within the limit $n \geq m \geq 0$. According to equation 1.3, we have $0^\circ \leq \theta_{Ch} \leq 30^\circ$.

Depending on the value of θ_{Ch} , nanotubes can be categorized into three different groups:

- zig-zag nanotubes: $m = 0, \theta_{Ch} = 0^\circ$
- armchair nanotubes: $n = m > 0, \theta_{Ch} = 30^\circ$
- chiral nanotubes: $n \neq m > 0, 0^\circ < \theta_{Ch} < 30^\circ$

The names come from the pattern of the nanotube's edge. For example, zig-zag tubes exhibit a zig-zag pattern along the circumference. Both zig-zag and armchair tubes are achiral tubes in contrast to other chiral tubes. Right-handed and left-handed nanotubes with the same chirality can be distinguished by circular dichroism[18].

The translational vector \vec{T} is the basis vector along the nanotube axis. Its length represents the shortest distance between two equivalent carbon atoms in this direction. \vec{T} is expressed by:

$$\vec{T} = \frac{2m+n}{d_r} \vec{a}_1 - \frac{2n+m}{d_r} \vec{a}_2 \quad (1.4)$$

$$|\vec{T}| = \frac{\sqrt{3} \cdot |\vec{C}_h|}{d_r} \quad (1.5)$$

Here d_r is the greatest common divisor of $(2m+n)$ and $(2n+m)$. Since \vec{C}_h and \vec{T} respectively connect two equivalent carbon atoms around the tube and along the tube, the unit cell of the tube can be seen as a rolled up rectangle with C_h and T as two sides, as is shown in fig 1.1. The number of carbon atoms in a unit cell can be calculated by dividing the rectangle surface area by half the area of graphene hexagons (one graphene hexagon contains two carbon atoms):

$$N_c = \frac{4(n^2 + m^2 + nm)}{d_R} \quad (1.6)$$

We can see that for chiral nanotubes, the unit cell can get much larger than the graphene hexagon. For instance, a (6,5) nanotube has 182 carbon atoms per unit cell. However, this means in reciprocal space, the first Brillouin zone is much smaller than that of graphene.

Fig. 1.2 shows the real space and reciprocal space lattice of graphene.

The reciprocal lattice vectors \vec{k}_1 and \vec{k}_2 are given by:

$$\vec{k}_1 = \left(\frac{1}{\sqrt{3}}, 1 \right) \frac{2\pi}{a_0}, \quad \vec{k}_2 = \left(\frac{1}{\sqrt{3}}, -1 \right) \frac{2\pi}{a_0} \quad (1.7)$$

In the direction of tube axis, which we denote as z-axis, the reciprocal lattice vector \vec{k}_z corresponds to the translation vector \vec{T} and its length is

$$k_z = \frac{2\pi}{|\vec{T}|} \quad (1.8)$$

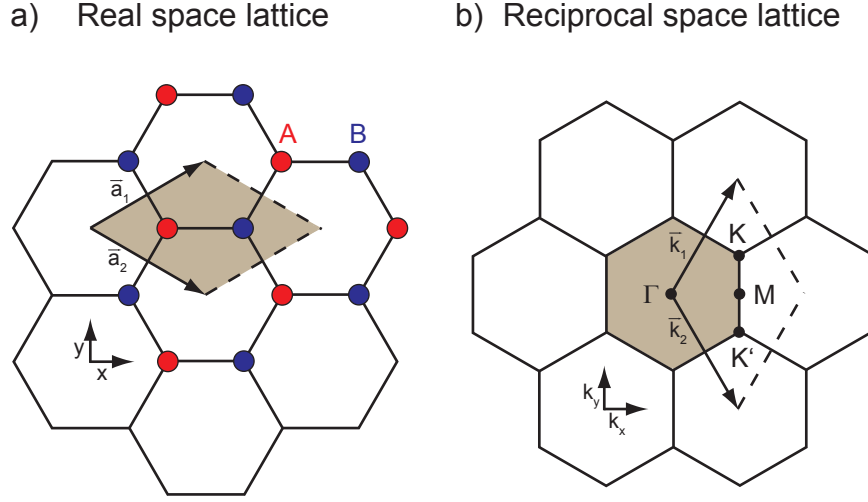


Figure 1.2: a) Real space unit cell of graphene. The unit cell (grey shaded area) is defined by real space lattice vectors \vec{a}_1 and \vec{a}_2 . One unit cell contains two unequal carbon atoms, each belonging to two intersecting sublattices, labeled as A (red circles) and B (blue circles). b) The first Brillouin zone (BZ) of graphene (grey shaded area) with the high symmetry points Γ , M and K (K'). \vec{k}_1 and \vec{k}_2 are the reciprocal lattice vectors. Figures adapted from ref[19, 20].

Since the tube length is regarded as infinite, the wave vector k_z is continuous, while the first Brillouin zone in z-direction lies within $\left(-\frac{\pi}{|\vec{T}|}, \frac{\pi}{|\vec{T}|}\right]$. Along the circumference, the wave vector \vec{k}_\perp is quantized due to the periodic boundary condition

$$m \cdot \lambda = |\vec{C}_h| \implies k_\perp = m \cdot \frac{2\pi}{|\vec{C}_h|} \quad (1.9)$$

where m is an integer with values $-N/2 + 1, \dots, 0, 1, \dots, N/2$ given that $2N$ is the number of carbon atoms in a unit cell. The boundary condition can be explained in the following way: the wave function of a quasi-particle such as an electron must have a phase shift of multiples of 2π along the circumference, otherwise it will vanish due to destructive interference. From another perspective, the number of carbon atoms in the unit cell limits the number of nodes the wave function can have, thus constrains the wave vector within a certain range.

The quantized wave vector \vec{k}_\perp and reciprocal lattice vector \vec{k}_z are derived from the conditions:

$$\begin{aligned} \vec{k}_z \cdot \vec{C}_h &= 0 & \vec{k}_z \cdot \vec{T} &= 2\pi \\ \vec{k}_\perp \cdot \vec{C}_h &= 2\pi & \vec{k}_\perp \cdot \vec{T} &= 0 \end{aligned} \quad (1.10)$$

which yields

$$\vec{k}_z = \frac{m}{N}\vec{k}_1 - \frac{n}{N}\vec{k}_2 \quad \vec{k}_\perp = \frac{2n + m}{Nd_r}\vec{k}_1 + \frac{2m + n}{Nd_r}\vec{k}_2 \quad (1.11)$$

Then the first Brillouin zone can be defined by wave vectors \vec{k} :

$$\vec{k} = m \cdot \vec{K}_\perp + t \cdot \frac{\vec{K}_z}{|\vec{K}_z|}, \quad -\pi/|\vec{T}| \leq t \leq \pi/|\vec{T}| \quad (1.12)$$

It consists of N lines parallel to tube axis with a length of $2\pi/|\vec{T}|$, and separated by $2\pi/|\vec{C}_h|$. As an example, figure 1.3 shows the first Brillouin zone of a (4,2) nanotube. Here $N = 2 * (4^2 + 2^2 + 4 * 2)/2 = 28$ so there are altogether 28 lines labeled from -13 to 14. This has a huge effect on the electronic band structure of the nanotube, which will be discussed in details in the next section.

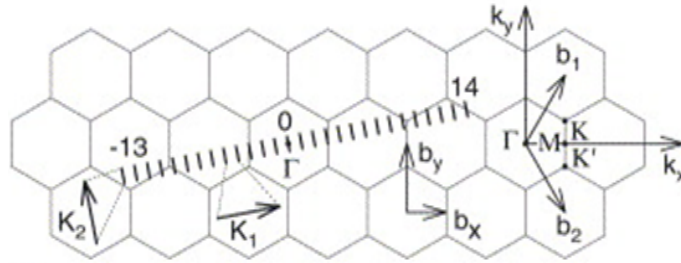


Figure 1.3: The Brillouin zones of (4,2) nanotube with respect to the reciprocal lattice. Along the nanotube circumference, the k values are quantized due to the boundary condition. Along the tube axis the k values are continuous. Figures adapted from ref [21].

1.1.2 Electronic Structure

In this section we focus on the electronic states of SWCNTs. As a starting point, the electronic energy dispersion relation of graphene will be discussed, with the help of tight-binding approach. Then we introduce the concept of zone folding, from which the band structure of carbon nanotubes can be directly obtained from that of graphene. This will explain why there are semiconducting and metallic nanotubes. Finally we calculate the density of states (DOS) in SWCNTs and show that the DOS is characterized by a series of van-Hove singularities.

In graphene the $2s$, $2p_x$ and $2p_y$ orbitals of carbon atoms form 3 in-plane sp^2 hybridized orbitals, while the $2p_z$ orbitals stick out of the plane and form delocalized π bonds with neighbouring $2p_z$ orbitals. In the unit cell of graphene which involves two carbon atoms, all the three σ bonding orbitals are filled with six valence electrons and the π bond is filled

with the other two electrons. The σ bonds are too far away from the Fermi energy level to influence electronic transport, at least in the visible energy range[22]. The transitions between π and π^* orbitals have a dominating effect on the optical and electrical properties of graphene.

We start from the well-known Schrödinger's equation:

$$\hat{H}\psi(\mathbf{k}) = E(\mathbf{k})\psi(\mathbf{k}) \quad (1.13)$$

The wave function can be written as a linear combination of Bloch functions $\Phi_l(\mathbf{k})$:

$$\psi(\mathbf{k}) = \sum_l C_l \Phi_l(\mathbf{k}) \quad (1.14)$$

$$\Phi_l(\mathbf{k}) = \frac{1}{\sqrt{N}} \sum_{i=1}^N e^{i\mathbf{k}\cdot\mathbf{R}_{j,i}} \phi_j(\mathbf{r} - \mathbf{R}_{j,i}) \quad (1.15)$$

where N is the number of atoms in a unit cell, and ϕ is the normalized $2p_z$ orbitals of an isolated carbon atom. There are only two carbon atoms in a unit cell, so here $l = 1$ or 2 . If we substitute the wave function in Eq. 1.13 by the expression of the Bloch functions in Eq. 1.14, and multiply $\Phi_l(\mathbf{k})^*$ from left, we get:

$$\begin{aligned} C_1[H_{11}(\mathbf{k}) - E(\mathbf{k})S_{11}(\mathbf{k})] + C_2[H_{12}(\mathbf{k}) - E(\mathbf{k})S_{12}(\mathbf{k})] &= 0 \\ C_1[H_{21}(\mathbf{k}) - E(\mathbf{k})S_{21}(\mathbf{k})] + C_2[H_{22}(\mathbf{k}) - E(\mathbf{k})S_{22}(\mathbf{k})] &= 0 \end{aligned} \quad (1.16)$$

where H_{ij} are the matrix elements of the Hamiltonian, S_{ij} are the overlaps between Bloch functions and $E(\mathbf{k})$ is the eigen energy. The subscript 1 and 2 represent the two kinds of carbon atom.

$$H_{ij} = \langle \Phi_i | H | \Phi_j \rangle \quad S_{ij} = \langle \Phi_i | \Phi_j \rangle \quad (1.17)$$

From Eq. 1.16 one can see that in order to have a non-trivial solution of E , $\det[H - ES]$ must equal 0. Then one needs to solve the elements of H and S . For the case of H_{11} :

$$H_{11} = \frac{1}{\sqrt{N}} \sum_{i=1}^N \sum_{j=1}^N e^{i\mathbf{k}\cdot(\mathbf{R}_{1,j}-\mathbf{R}_{1,i})} \langle \Phi_1(\mathbf{r} - \mathbf{R}_{1,i}) | H | \Phi_1(\mathbf{r} - \mathbf{R}_{1,j}) \rangle \quad (1.18)$$

Note that $N=2$ for graphene. Here we apply the ‘‘nearest neighbour’’ approximation in the sense that one atom will only interact with its nearest neighbours. Since one carbon atom is always surrounded by 3 atoms of another type in the unit cell, in equation 1.18 we only need to consider the condition when $i=j$. Then we have

$$H_{11} = \langle \Phi_1(\mathbf{r} - \mathbf{R}_1) | H | \Phi_1(\mathbf{r} - \mathbf{R}_1) \rangle = \xi_{2p} \quad (1.19)$$

ξ_{2p} is the Fermi energy. Similarly, we have

$$S_{11} = \langle \Phi_1(\mathbf{r} - \mathbf{R}_1) | \Phi_1(\mathbf{r} - \mathbf{R}_1) \rangle = 1 \quad (1.20)$$

Atoms type 1 and 2 are chemically identical so $H_{22} = H_{11}$, $S_{22} = S_{11} = 1$. For the off-diagonal elements we have:

$$H_{12} = \frac{1}{\sqrt{N}} \sum_{i=l}^N \sum_{j=l}^3 e^{i\mathbf{k} \cdot (\mathbf{R}_{2,j} - \mathbf{R}_{1,i})} \langle \Phi_1(\mathbf{r} - \mathbf{R}_{1,i}) | H | \Phi_2(\mathbf{r} - \mathbf{R}_{2,j}) \rangle \quad (1.21)$$

For each neighboring pair the interaction should be the same, so we can define

$$\gamma_0 = - \langle \Phi_1(\mathbf{r} - \mathbf{R}_{1,i}) | H | \Phi_2(\mathbf{r} - \mathbf{R}_{2,j}) \rangle \quad (1.22)$$

Then Eq. 1.21 can be rewritten as:

$$H_{12} = -\frac{\gamma_0}{N} \sum_{i=l}^N \sum_{j=l}^3 e^{i\mathbf{k} \cdot \delta_j} = -\gamma_0 f(\mathbf{k}) \quad \delta_j = \mathbf{R}_{2,j} - \mathbf{R}_{1,i} \quad (1.23)$$

Here δ_j represent the position of atom type 2 with respect to atom type 1. From figure 1.1 one can find the possible δ_j :

$$\delta_1 = (0, \frac{a}{\sqrt{3}}), \quad \delta_2 = (\frac{a}{2}, -\frac{a}{2\sqrt{3}}), \quad \delta_3 = (-\frac{a}{2}, -\frac{a}{2\sqrt{3}}) \quad (1.24)$$

Then

$$f(\mathbf{k}) = e^{ik_y a / \sqrt{3}} + 2e^{-2k_y a / 2\sqrt{3}} \cos(k_x a / 2) \quad (1.25)$$

Similarly we have $S_{12} = s_0 f(\mathbf{k})$. Finally the matrix of H and S are:

$$H = \begin{bmatrix} \xi_{2p} & -\gamma_0 f(\mathbf{k}) \\ -\gamma_0 f(\mathbf{k})^* & \xi_{2p} \end{bmatrix} \quad S = \begin{bmatrix} 1 & -s_0 f(\mathbf{k}) \\ s_0 f(\mathbf{k})^* & 1 \end{bmatrix} \quad (1.26)$$

Then we obtain the energy:

$$E_{\pm} = \frac{\xi_{2p} \pm \gamma_0 |f(\mathbf{k})|}{1 \pm s_0 |f(\mathbf{k})|} \quad (1.27)$$

Here ξ_{2p} marks the origin of the energy axis and is often set to 0. γ_0 and s_0 can be determined from experimental results, for example in ref [23] $\gamma_0=3.033$ eV and $s_0=0.129$. It is noteworthy that the valence band and conduction band are actually not symmetric with respect to the Fermi level due to the existence of s_0 . Since it doesn't affect our conclusion, in the following discussion we will take the simplified condition with $s_0=0$. Fig. 1.4(a) shows the band structure of graphene in the first Brillouin zone. π and π^* bands intersect at \mathbf{K} and \mathbf{K}' points, which makes graphene a zero-bandgap semiconductor. Close to these points the dispersion relation has a linear slope and the energy surface has a cone-like shape, as is shown in figure 1.4(b). The dispersion relation deviates from linear behavior when the position moves away from K point. As we can see, at Γ point the splitting between

π and π^* bands is the largest, and the energy difference decreases faster from Γ to K than from M to K. This phenomenon is named *trigonal warping*.

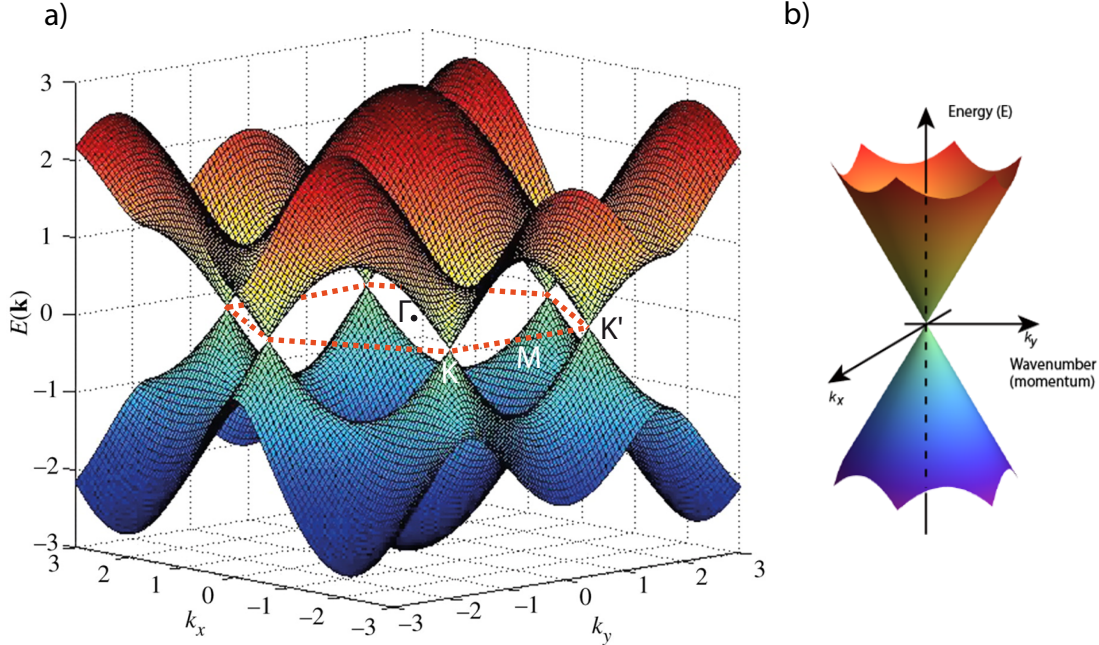


Figure 1.4: a) Electronic energy dispersion relation of graphene in the first Brillouin zone with nearest neighbour tight-binding approximation. The high symmetry points Γ , M , K and K' are also indicated. The valence and conduction band cross at K and K' points. b) Linear energy dispersion relation near the K points. Figures adapted from ref [24].

In section. 1.1.1 we mentioned that the first Brillouin zone of carbon nanotubes are parallel lines with a length of $2\pi/|\vec{T}|$, and separated by $2\pi/|\vec{C}_h|$. The length and orientation of these lines depend on the chirality (n,m). The basic idea of zone-folding is that the electronic band structure of a nanotube is determined by the graphene electronic energies along the allowed k lines. Figure 1.5 illustrates the allowed k lines of a (3,3) nanotube on graphene's dispersion relation.

From the zone folding approximation one can understand the metallic and semiconducting character of SWCNTs. Previously we mentioned that the valence band and conduction band cross at the K point of the Brillouin zone. If the allowed k lines go through the K point, then the nanotube is metallic; otherwise it's semiconducting with a band gap. According to figure 1.2, $\mathbf{K} = \frac{2}{3}\mathbf{k}_1 + \frac{1}{3}\mathbf{k}_2$, thus a (n,m) nanotube is metallic if \mathbf{K} satisfies the

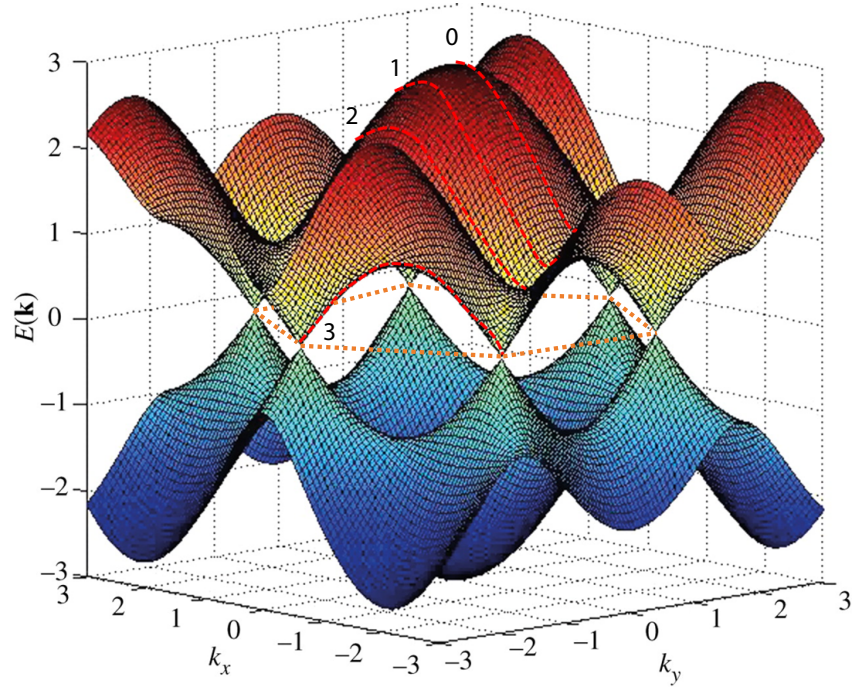


Figure 1.5: Illustration of the zone-folding approach for a (3,3) nanotube. The red dashed lines are the allowed k values which represent the first Brillouin zone. Each line cuts through the graphene dispersion relation and creates a pair of conduction and valence band. Due to limitation of space, only the lines with $m=0,1,2,3$ in Eq. 1.12 in the upper half of graphene band are shown here. In this case, the allowed k lines go through \mathbf{K} point.

boundary condition:

$$\mathbf{K} \cdot \mathbf{C}_h = \frac{1}{3}(2\mathbf{k}_1 + \mathbf{k}_2)(n\mathbf{a}_1 + m\mathbf{a}_2) = \frac{2\pi}{3}(2n + m) = t \cdot 2\pi \quad (1.28)$$

So $2n+m$ needs to be a multiple of three. This was firstly reported by Hamada[25] and Saito[26]. Figure 1.6 (a) shows the conductivity of some low index chiralities. It's easy to see that one third of all possible SWCNTs are metallic. The nanotubes can be further divided into three categories: metallic, semiconducting type I (S_1), semiconducting type II (S_2), depending on the relative position of the allowed k lines with respect to the \mathbf{K} point as illustrated in figure 1.6 (b) to (d). For semiconducting SWCNTs, the \mathbf{K} point is always between two adjacent cutting lines with a distance of $1/3 |\vec{K}_\perp|$ to the closest one. S_1 type refers to the SWCNTs with the closest cutting line on the left of the \mathbf{K} point, thus the first energy band comes from cutting the $\mathbf{K} \rightarrow \Gamma$ energy contour. On the contrary, the closest cutting line of S_2 type is on the right side of \mathbf{K} , so their first energy band is the intersection of $\mathbf{K} \rightarrow \mathbf{M}$ energy contour. Due to trigonal warping, type I and II pos-

sess different energy separations of the bands and hence different optical transition energies.

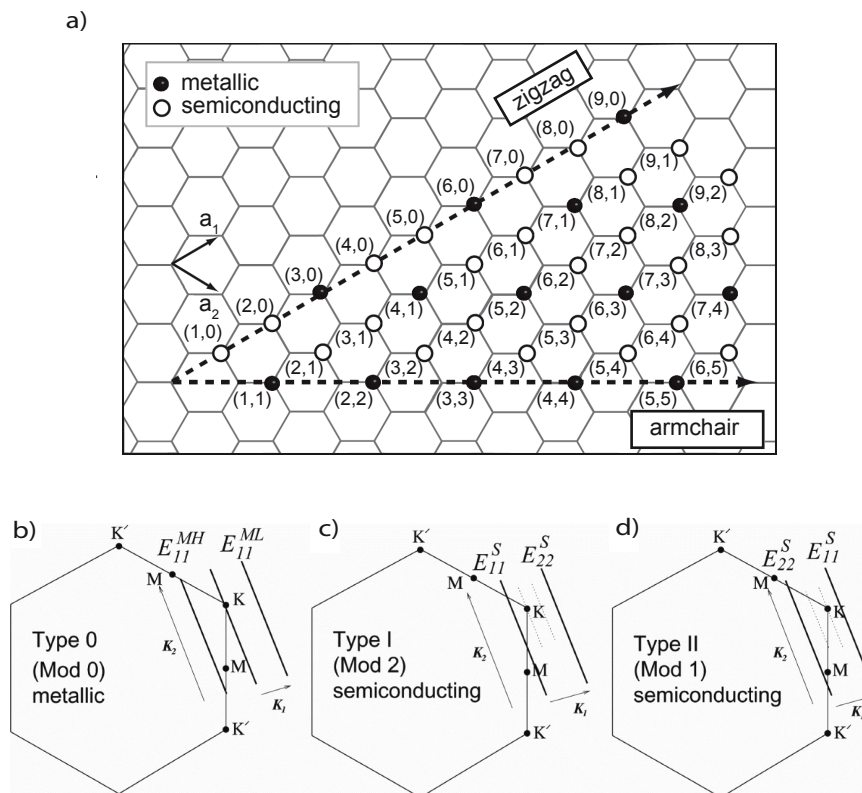


Figure 1.6: a) The conductivity of some low index nanotubes. The black and white circles respectively represent metallic and semiconducting SWCNTs. All the armchair SWCNTs with $n=m$ are metallic. Figure is adapted from ref[19]. b) When the allowed wave vector k lines go through K point, the SWCNT is metallic. c)-d) When the allowed k lines don't go through K point, the SWCNT is semiconducting. Depending on the relative position of closest line with respect to K , left (S_1) or right (S_2), the lines cut through different energy dispersion relation. For S_1 and S_2 SWCNTs with similar diameters, this results in different energy bandgap and optical transition energies. Figures adapted from ref[27].

Generally, zone folding approach is a fast and reliable method for electronic states close to Fermi level and large diameter nanotubes with $d \sim 1.5\text{nm}$. It should be pointed out that zone folding has its limitations: it doesn't take the curvature of nanotube into consideration. The curvature of SWCNT changes the C-C distance and the angle of hexagons, then the assumption of equivalent neighbors is not valid[28]. In addition, the mixing of σ and π bonds will take place due to non-orthogonality, which moves \mathbf{k}_F away from the K -point along the circumferential direction and opens a small bandgap at the K -point[29]. The cur-

vature effect becomes stronger as the tube diameter decreases. For tubes with $d \leq 0.5\text{nm}$, zone folding results are not trustworthy any more. In these cases ab-initio calculations usually provide a more accurate solution and obtain good agreements with experimental results[22, 30].

Another important electronic property tightly linked to the optical transition of SW-CNTs is the electronic density of states (DOS). The DOS is defined as the number of electronic states between energy E and $E + \Delta E$ and it depends on the slope of the dispersion relation. The DOS $n(E)$ for a one-dimensional system is[31]:

$$n(E) = \frac{2}{q |k_z|} \sum_i \int dk_z \delta(k_z - k_i) \left(\left| \frac{\partial E^\pm(k_\perp, k_z)}{\partial k_z} \right| \right)^{-1} \quad (1.29)$$

Here $q |k_z|$ is the total area of the Brillouin zone and k_i are the roots of $E - E^\pm(k_\perp, k_z) = 0$. Close to Fermi energy, we approximate the energy bands to be straight lines close to \mathbf{K} . Then $n(E)$ is derived to be:

$$n(E) = \frac{4a_0}{\pi^2 d \gamma_0} \sum_{m=-N/2}^{N/2} \begin{cases} |E| / \sqrt{E^2 - (E_m)^2}, & |E| > |E_m| \\ 0, & |E| < |E_m| \end{cases} \quad (1.30)$$

Where $m \cdot \vec{K}_\perp + t \cdot \vec{K}_z$ is the allowed wave vector (Eq. 1.12) of a (n_1, n_2) chirality nanotube, and E_m is expressed by:

$$E_m = \frac{a_0 \gamma_0}{\sqrt{3}d} |3m - n_1 - n_2| \quad (1.31)$$

For metallic nanotubes, $E_m = 0$ refers to the valence and conduction band which cross each other at the \mathbf{K} point. It is important to note that for $E_m = 0$, $n(E)$ is a constant and different from zero. For semiconducting nanotubes, $E_m > 0$ so the density of states will be zero when $|E| < |E_m|$. For both kinds of tubes, at $E = E_m$ $n(E)$ exhibits a single spike, this is referred to as *van-Hove singularity*. Fig. 1.7 shows the energy band and corresponding density of states of metallic and semiconducting SWCNT. Generally, a van-Hove singularity (vHs) is a non-smooth point in density of states of a crystalline solid. In carbon nanotubes, they represent the discontinuous peaks at different E_m values. The existence of vHs was first experimentally proved by scanning tunneling microscopy[32] and resonance Raman scattering[33].

Apparently, strong optical transitions will happen between mirror imaged pairs of van Hove singularities. We use E_{ii} to note the transition energy between number i peaks. Based on linear approximation near \mathbf{K} point, E_{11} of metallic and semiconducting CNTs can be written as:

$$E_{11}^M \approx 6a_0 t / \sqrt{3}d_t \quad E_{11}^S \approx 2a_0 t / \sqrt{3}d_t \quad (1.32)$$

This equation is valid if the tube diameter is large enough ($\geq 1.5\text{nm}$) such that the distance from the \mathbf{K} point lies within linear dispersion range, then the transition energy is

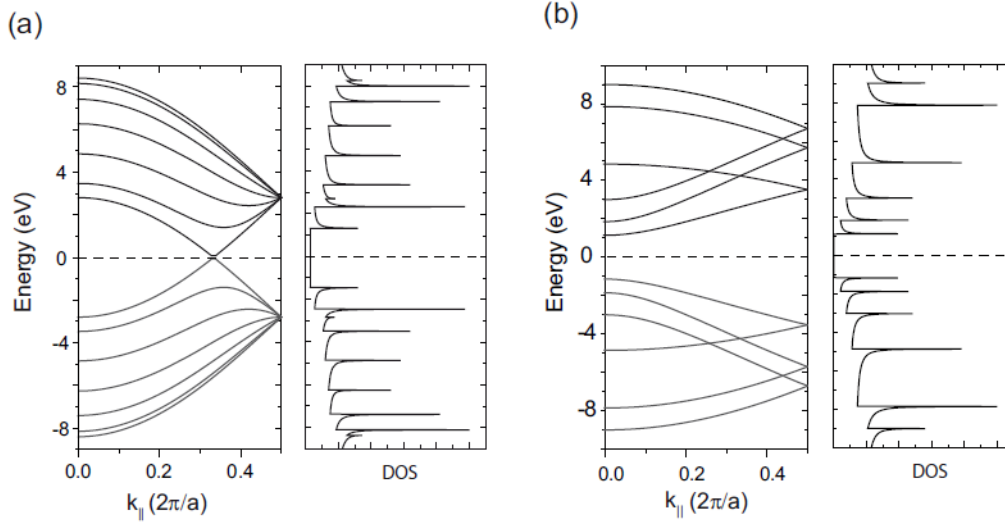


Figure 1.7: Energy bands and corresponding density of states of a) a metallic (6,6) SWCNT and b) semiconducting (5,0) SWCNT. The results are calculated according to the nearest neighbor tight-binding model with parameters $\xi_{2p} = 0$, $s_0 = 0$ and $\gamma_0 = 3.0$. Van-Hove singularities appear at local maxima or minima of the band energy relation. For a metallic nanotube, valence and conduction bands meet and the DOS is constant between the first pair of vHs; while for a semiconducting nanotube the DOS is zero within this region, leading to a clear direct band gap.

inversely proportional to the tube diameter. When the tube diameter gets smaller, a certain amount of deviation occurs. In addition, E_{ii} of S1 and S2 CNTs with similar diameter will split because of the trigonal effect. In 1999, Hiromishi Kataura firstly calculated E_{ii} of a wide range of tube chiralities according to the tight-binding model and plotted them against the tube diameter, which is named Kataura plot[34].

Figure 1.8 shows the latest Kataura plot containing both experimental and calculation results[35]. It could be seen that deviations from the linear relationship emerges when $1/d_t$ gets larger, also the energy difference between S1 and S2 becomes much more clear. For higher transitions, some data points tend to gather together. These data points come from the chiralities with the same $(2n+m)$ value, commonly referred to as the same family. These tubes have similar diameters but various chiral angles and thus different influence of trigonal warping which results in slight energy variation.

The optical transitions of SWCNTs have a strong polarization dependence. The E_{ii} (longitudinal) transitions, which are just mentioned above, occur between valence and conduction bands from the same line of Brillouin zone, thus $\Delta k_{\perp} = 0$, these transitions only interact with the field parallel to tube axis, in other words they are polarized along tube axis.

The E_{ij} (transverse) transitions with $i \neq j$ are also possible. In this case, they originate from different cutting lines in the Brillouin zone and $\Delta k_{\perp} \geq 2\pi/C_h \gg \Delta k_{\parallel}$. These transi-

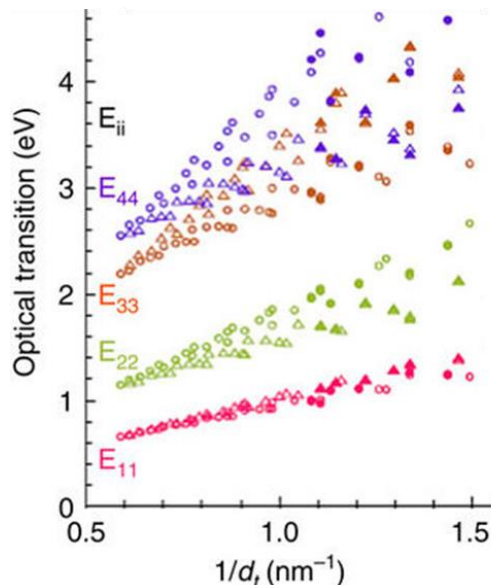


Figure 1.8: Transition energies E_{11} , E_{22} , E_{33} , E_{44} as a function of $1/d_t$. Circles and triangles indicate S1 and S2 type CNTs. Open and solid symbols represent calculation and experimental results, respectively. Figure is adapted from ref [35].

tions are polarized perpendicular to the tube axis. Longitudinal transitions are responsible for most optical features of SWCNT, however, transverse transitions also show small but distinct absorption peaks[36, 37].

Figure 1.9 displays the selection rules for electronic transitions in SWCNTs by excitation with light polarized parallel and perpendicular to the tube axis within the first two pairs of van Hove singularities.

1.1.3 Excitons and Photoluminescence

SWCNT's optical properties are to a large extent determined by excitons (strongly bound electron-hole pairs). Their emission in the NIR or IR region, i.e. photoluminescence (PL) originates from the radiative recombination of excitons. In this section we will first introduce the concept of excitons and their fine structure, and then discuss the important properties of PL.

Excitons

When light illuminates a non-transparent solid, excited electrons and holes are generated by photon absorption. Generally, the negatively charged electron and positive charged hole are stabilized together through the attractive Coulomb force and form a two-particle bound state which is called exciton. The binding energy E_b tells how strong the attractive

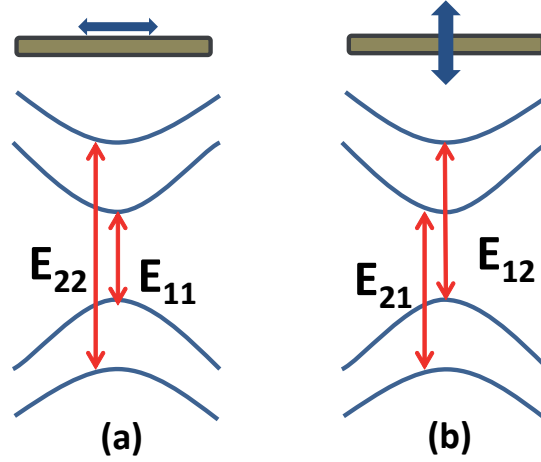


Figure 1.9: Selection rules for transitions in semiconducting SWCNTs depending on incident light polarization. Only transitions between the first two sub-bands are shown here. a) When the light is polarized along the tube axis, E_{11} and E_{22} transitions can occur. b) When the light is polarized perpendicular to the tube axis, E_{12} and E_{21} transitions are possible. Figure is adapted from ref [38].

interaction is. In bulk semiconductors, E_b is usually much smaller than $k_B T$ at room temperature and the optical properties are dominated by free-particle interband transitions. However, in 1D nanostructures such as SWCNT, the reduced dimensionality significantly reduces the separation distance of electrons/holes and leads to strong electronic many-body interactions. Therefore in SWCNTs E_b can be extremely large reaching a few hundred eV[39, 40, 41, 42]. Compared to bulk semiconductors, SWCNTs exhibit clear excitonic transitions at room temperature. Fig. 1.10 (a) is a scheme of the band structure and the exciton energy. Here E_{ex} refers to the energy of the exciton with respect to ground state.

The binding energy of the exciton depends on the mean distance between electron and hole. If the distance decreases, E_b increases but the kinetic energy of electron-hole pair's relative motion also increases because of the uncertainty principle. This situation is very similar to hydrogen atom model, and there are also certain optimum distances at which the system is the most stable, like different orbitals in hydrogen atom. Fig. 1.10 (b) illustrates the energy dispersion relation as a function of exciton center of mass wave vector k_{ex} . In the context of the hydrogen atom model, the lowest exciton state can be identified as 1s ground state with $n=1$, while higher lying states correspond to $n=2,3,\dots$ up to the continuum may occur (grey area). These energy levels have been experimentally observed.[43]

Fig. 1.10 (c) is a qualitative illustration of E_{ii} energy bands against k_{ex} . Only the lowest energy level for each energy band is shown. It is important to note that although SWCNTs absorb strongly at E_{ii} peaks, PL emission predominantly happens at E_{11} due to very efficient and fast non-radiative relaxation from higher order states to the E_{11} state[44, 45].

As mentioned before, there are two unequal carbon atoms in graphene's unit cell, the-

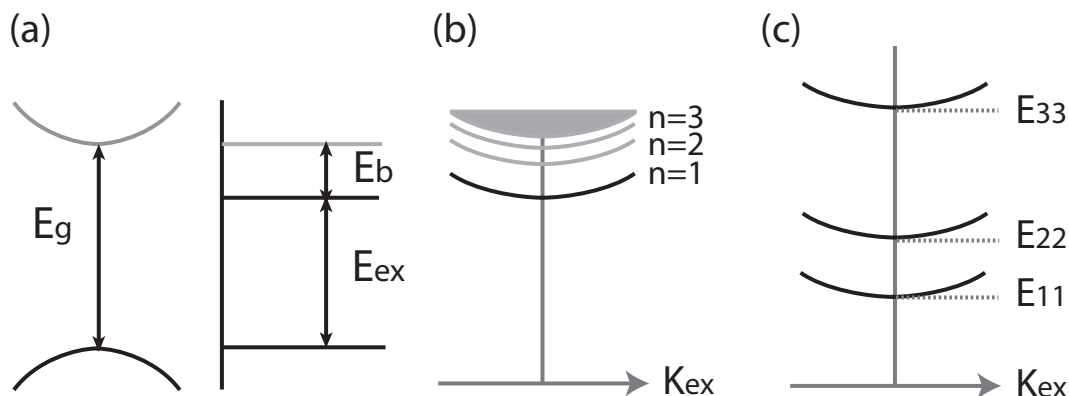


Figure 1.10: a) Band structure and density of states of the first sub-band. Due to the exciton binding energy E_b , optical resonances happen at exciton energy E_{ex} instead of E_g . b) Schematic of the exciton energy as a function of exciton center of mass wave vector k_{ex} . Similar to the hydrogen atom, different excitonic energy levels correspond to different electron-hole separation distance and symmetries. c) Exciton states from the first three sub-band transitions. Figure is adapted from ref [38].

before in the momentum space of SWCNT there are two equivalent valleys (labeled as K and K' in Figure 1.11 (a)). This has important consequences for the optically allowed excitonic transitions. The concept of direct exciton transitions described above refers to electron-hole pairs in the same valley, i.e. KK or K'K' configuration. Indirect excitons refer to KK' or K'K. Altogether there exist 4 singlet and 12 triplet exciton states for a particular sub-band of SWCNT[46, 47]. The two degenerate direct excitons KK and K'K' will couple and form different states with higher or lower energies. Only one state is optically allowed and referred to as bright exciton, while all the other states including indirect ones are optically forbidden and named as dark excitons. The relative ordering of bright and dark direct excitons, however, can be quite complicated. It was found that for the 1st sub-band transition, the dark exciton has a lower energy than the bright one for all SWCNT chiralities[48]. This is shown in Figure 1.11 (b). On the other hand, the indirect excitons possess a large momentum linking K and K' valleys and have the largest energy. These “K-momentum” dark excitons have been experimentally confirmed[49]. Figure 1.11 (c) is a scheme of exciton energy levels containing both direct and indirect excitons.

PL

Quantum Yield. The excitons in SWCNTs can't exist for very long time, they will decay either radiatively or non-radiatively. Non-radiative pathways include intrinsic processes (exciton-phonon coupling, trap states of defect/impurity/tube end, Auger recombination, etc) and extrinsic processes (e.g. energy transfer to neighbouring molecules). The lifetimes

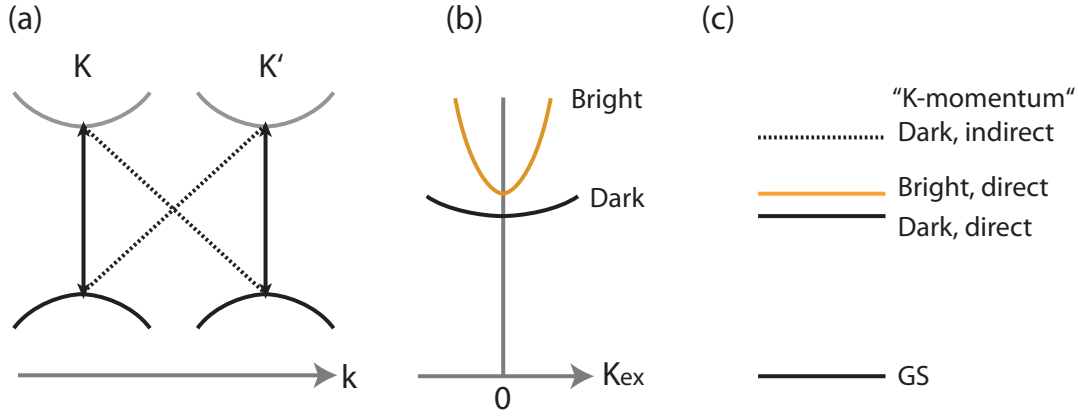


Figure 1.11: a) K and K' valleys give rise to 4 electron-hole configurations. b) Bright and dark excitons energy dispersion relation close to the point $k_{ex} = 0$. The energy of dark exciton is below the bright one. c) The distribution of indirect and direct exciton energy levels. Indirect (KK' or K'K) excitons are marked as K-momentum excitons (dotted line) and they have the highest energy. Figure is adapted from ref [38].

τ_r , τ_{nr} describe the time scales on which the ground state is repopulated by photon or phonon emission through specific processes. From this, one can get the decay rates $k_r = 1/\tau_r$, $k_{nr} = 1/\tau_{nr}$ representing how fast the radiative and non-radiative decay occur. The quantum yield (QY) η is an important parameter, which is the ratio of emitted photons to absorbed photons:

$$\eta = \frac{n_{emitted}}{n_{absorbed}} = \frac{k_r}{k_r + k_{nr}} \quad (1.33)$$

SWCNTs have been regarded as a poor emitter for a long time due to the low quantum yield of less than 1% observed in early works[50, 51, 52]. The reported exciton lifetime is at picosecond level[53], while the radiative lifetime is usually a few magnitudes larger with the value between 10 to 100 ns[50, 51, 52]. However, the most important reason for the low quantum yields turned out to be the low sample quality, i.e. poor chirality sorting, high defect density and high impurity concentration. In 2009, Ju et al. used an aliphatic (dodecyl) analog of flavin mononucleotide FC12 to separate the SWCNTs and protect them from oxygen. A PL QY as high as 20% was reached[54].

Mobility. The exciton coherence length is defined as the distance within which the exciton can capture the oscillator strength. In highly isolated SWCNT ensembles it was found to be as small as 10 nm[55], so the exciton motion shall be treated as diffusive transport of a point-like object. Given the reduced dimensionality of SWCNT, one can safely assume exciton diffusion following a quasi-1D random walk. Diffusion constant D is commonly used to characterize exciton transport properties in SWCNTs. In various literature time-resolved PL decay and subsequent global fitting were used to determine

the value of D , the results are widely ranged between 1 and 40 cm^2/s with corresponding diffusion length $L = \sqrt{2D\tau}$ between 10 and 300 nm[56, 57, 58, 59, 60]. D and L significantly depend on material quality and environmental effects. The diffusional exciton migration leads to exciton quenching at defect sites and nanotube ends[61, 62, 63] and exciton-exciton annihilation under strong excitation power[64, 57, 65], which we will address in details in the following sections.

Local modifications & Environmental effects.

In early works, chemical reactants were used to attack SWCNT and to induce defects, upon which substantial PL intensity quenching[61, 62] was observed. Crochet and co-workers introduced mid-gap and shallow impurity levels and imaged exciton quenching in both cases. In addition, they found that the quenching sites can be mobile[63]. Generally, defect sites are considered to enhance non-radiative recombination and thus reduce PL intensity. In recent years, it was found that a small number of sp^3 defects below the dark exciton energy level can act as luminescent exciton traps and remarkably brighten the PL of SWCNTs. These defects have been introduced via covalent functionalization with oxygen (ether and epoxide groups)[66, 67], hexanoic acid[68] and substituted aryl species[69, 70, 71]. Figure 1.12 is a typical example of aryl diazonium functionalized SWCNTs. Michael Rohlfinger's group also confirmed that the new PL peaks stem from impurity levels via theoretical calculations[72]. We note that these sp^3 defects need to be elaborately designed and don't exist in standard SWCNT synthesis procedures.

Electron-electron and electron-hole Coulomb interactions are much stronger in SWCNTs than bulk semiconductors and they highly depend on the dielectric environment, therefore the surrounding medium has a large effect on the exciton energy. Experimental results display that air or vacuum suspended SWCNTs have a blue-shifted emission compared with SWCNTs on dielectric substrates[73, 74]. According to Michael Rohlfinger, a homogeneous change of the dielectric background actually shifts the band gap and exciton binding energy to the same amount and it is the electronic polarization by neighboring systems, especially physisorbates, that leads to exciton energy shift[75]. This also explains why bundling or incomplete surfactant wrapping also lead to a red shift of the exciton energy.

In ambient air at room temperature, blinking, bleaching and spectral diffusion behavior of SWCNT PL is very commonly observed, which in general can be attributed to the complicated interaction between SWCNT and a variety of species in air, such as oxygen/water under laser illumination. In 2008, Georgi et al. investigated the blinking and bleaching behavior of sodium cholate wrapped SWCNTs in air and argon[56]. They demonstrated that photo-induced oxidation is the primary reason for bleaching, with the rate depending on laser intensity. Nan et al. compared the PL of SWCNTs on SiO_2 substrate in vacuum at 7K with and without a PMMA capping layer. The capped ones exhibited 5-fold enhancement of PL intensity and suppression of blinking[76]. After two weeks exposure in air, they displayed blinking and spectral diffusion but this behavior could be suppressed again by heat treatment. They concluded that the physisorbed water molecules which act as charge trap states are the primary reason for spectral diffusion. Finnie and Lefebvre systematical-

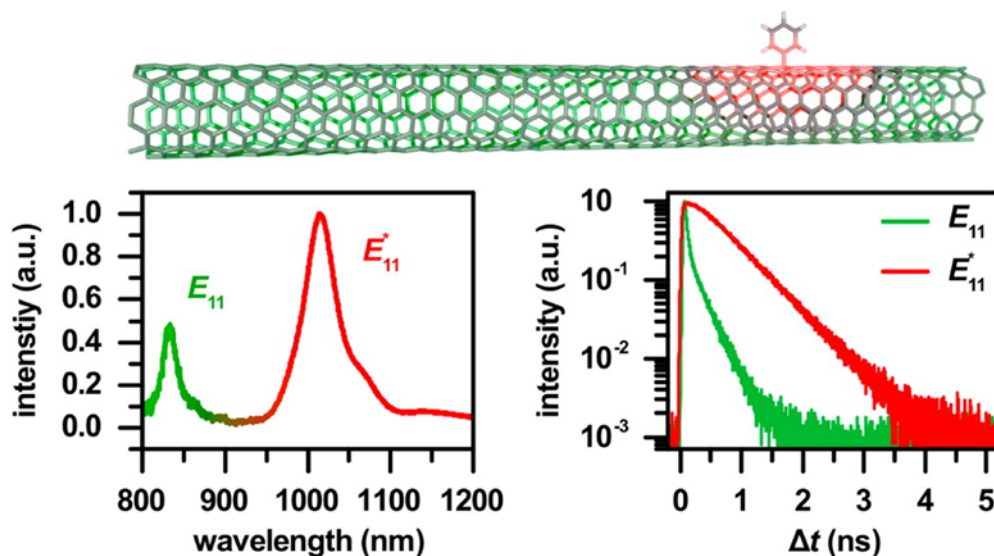


Figure 1.12: Illustration of Aryl sp^3 defected SWCNTs. top: A schematic of locally doped SWCNT. down left: Representative PL spectra for doped (5,4) SWCNTs with the E_{11} emission peak (green) and the stronger E_{11}^* luminescence peak caused by aryl diazonium doping (red). down right: E_{11}^* has a much longer lifetime than E_{11} . Figure is adapted from ref [71].

ly studied the spectral changes of air-suspended SWCNTs under constant excitation[77]. They demonstrated that light-induced atmospheric physisorbates are responsible for a red shift and that the fluctuations of the charge state of oxygen chemisorption sites result in the blinking. To sum up, during PL emission the nanotube usually interacts with various species/reactions at the same time and more efforts are required to fully understand the picture.

1.1.4 Raman Scattering of SWCNT

Raman spectroscopy is a non-destructive experimental technique for investigating the structure and physical properties of nanomaterials. Especially in carbon science, it is one of the most widely used tools[78, 27, 79]. In this section, we will first briefly illustrate the basics of Raman scattering and then review the characteristic Raman bands of SWCNTs.

Raman scattering is the inelastic scattering of light. In a standard Raman process, an incident photon with energy E_i and momentum k_i hits the sample and gets inelastically scattered, resulting in a different photon with energy E_s and momentum k_s and the creation of a lattice vibration (phonon) or a molecular vibration. The energy and momentum must

be conserved:

$$E_s = E_i + E_q \quad k_s = k_i + q \quad (1.34)$$

where E_q and q are the energy and momentum change of the phonon.

The Raman process which absorbs or emits one phonon is named a first-order Raman process. It consists of three steps: firstly an incoming photon with a frequency ω_1 excites an electron-hole pair, then the electron or hole is inelastically scattered and emits a photon with wave vector q and frequency ω_{ph} . Finally the electron and hole recombines and emits a photon at frequency ω_2 . Raman shift is usually denoted as the difference between wavenumbers of original photon and emitted photon with the unit of cm^{-1} . Similar with Eq. 1.34, here we have:

$$\omega_2 = \omega_1 \pm \omega_{ph} \quad k_2 = k_1 \pm q \quad (1.35)$$

+ sign means the emitted photon has a higher frequency and energy than the original one. In other words, A new photon is created whose energy is higher than the incident phonon energy. This is referred to as anti-Stokes process. In the other case, a photon is emitted at a lower energy, which is referred to as Stokes process. Figure 1.13 is a simplified illustration of these two processes.

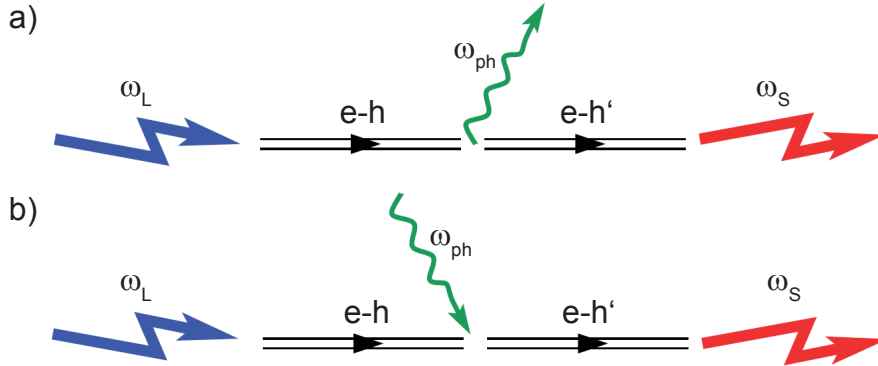


Figure 1.13: a) Stokes: The incident light excites the system and emits a phonon. b) Anti-Stokes: The system is already excited and a phonon is absorbed. Figure is adapted from ref [79].

The probabilities of Stokes p_S and anti-Stokes p_{AS} depend on the phonon population[27]:

$$\frac{p_S}{p_{AS}} \approx \exp\left(\frac{\hbar\omega_{ph}}{kT}\right) \quad (1.36)$$

with k as the Boltzmann constant and T as the temperature. At room temperature $p_S \gg p_{AS}$, the Stokes process is much stronger. This equation only applies to the case of non-resonant Raman scattering.

It should be noted that Raman scattering is an extremely weak process. However, if the energy of incident photon or scattered photon matches an electronic transition, the probability for an incoming photon to be scattered will be enhanced by orders of magnitude and results in a stronger Raman intensity. This is called resonant Raman scattering. If no energy match exists, the process is called non-resonant scattering. Raman processes can be further categorized depending on the energy match condition. Figure 1.14 (b)-(d) shows the energy diagram of resonant Raman scattering.

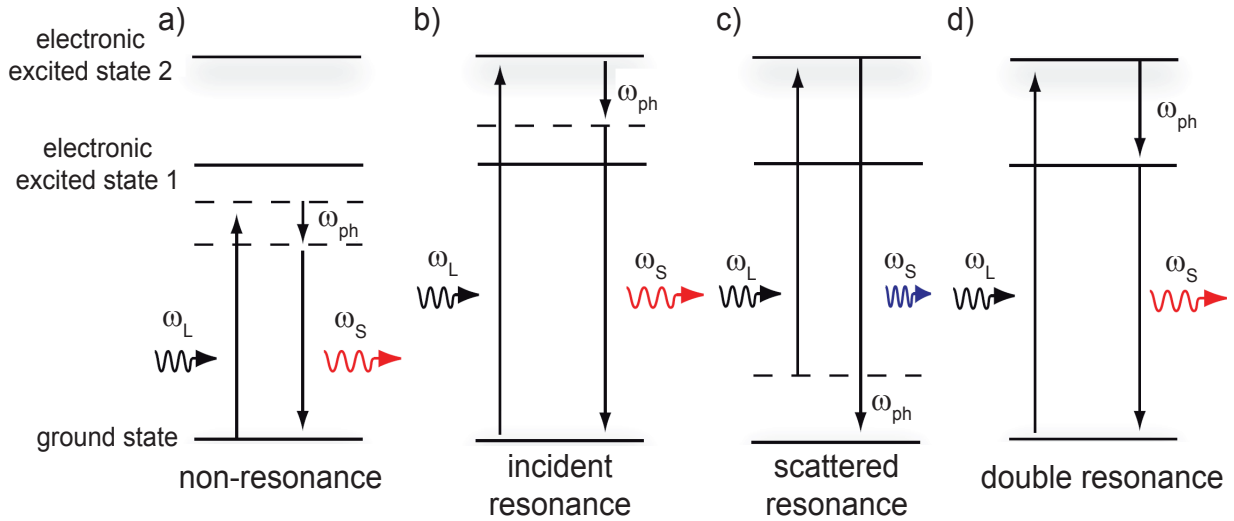


Figure 1.14: a) Non-resonant Raman scattering, neither ω_L or ω_S matches the transition energy. This process is very weak. b) Stokes resonant Raman scattering with the incident photon matching one transition. c) Anti-Stokes resonant Raman scattering with the scattered photon matching another transition. d) Double resonant Raman scattering when both the incident and scattered photons have an energy match. Figure is reprinted from ref [19].

In the following we briefly discuss the 4 characteristic Raman features of SWCNT: the radial breathing mode(RBM), the graphite-like G band, the defect-induced D band and the overtone of D band which is named G' or 2D band. There are several other weaker Raman bands such as the intermediate frequency modes scattered by acoustic phonons[80]. Since Raman detection is not the main focus of the work, they will not be discussed here.

The Radial Breathing Mode

The radial breathing mode is associated with the vibration of all the carbon atoms in the radial direction, as if the tube is breathing. Since this vibrational motion doesn't break tube symmetry, the RBM is a totally symmetric mode. The RBM mode only occurs in CNTs among all the nanocarbon material, thus it can be used to distinguish CNTs in a mixed sample. It was found that the RBM frequency is inversely proportional to tube

diameter:

$$\omega_{RBM} = A/d_t + B \quad (1.37)$$

A and B are parameters that can be determined from experimental results[81, 82] with their values varying in different literature. Generally A is around $227 \text{ cm}^{-1}nm$ and B is related to environmental interactions from 0 to 30 cm^{-1} . Because of its dependence on tube diameter, the position of the RBM mode is often used for investigations of (n,m) chiralities in dense nanotube samples.

G band

The G band is related to the in-plane stretching vibration of the C-C bond. In graphene, the longitudinal optical (LO) phonon and transverse optical (TO) phonon at $q=0$ are degenerate, and the G band exhibits a single Lorentzian peak. While in SWCNTs, because the symmetry is broken by the curvature, LO and TO phonon have different energies and the G band splits into two peaks, usually denoted as G^+ and G^- for the higher and lower frequency part. For semiconducting and metallic nanotubes, the lineshape and frequency of the G band can be substantially different.

For semiconducting SWCNTs, G^+ and G^- emerge as two separate narrow Lorentzian peaks and G^+ is usually much stronger. Here G^+ corresponds to the LO phonon mode and has a frequency of 1590 cm^{-1} which doesn't strongly depend on tube diameter. G^- corresponds to the TO phonon and significantly relies on tube diameter following $\omega_{G^-} = \omega_{G^+} - C/d_t^2$ with $C = 47.7 \text{ cm}^{-1}nm^2$.

For metallic SWCNTs, due to strong electron-phonon coupling near the Fermi energy[83, 84], the correspondence of G^+ and G^- to LO and TO phonons is opposite to the situation in semiconducting SWCNTs. Instead of a Lorentzian shape, G^- exhibits a much broader Breit-Wigner-Fano (BWF) peak and its frequency can be described by $\omega_{G^-} = \omega_{G^+} - C/d_t^2$ with $C = 79.5 \text{ cm}^{-1}nm^2$. On the other hand, G^+ has a similar behavior with a narrow lineshape and weak dependence on tube diameter, but its intensity is much weaker and often covered by G^- .

D band

Many defect structures that can scatter photo-excited electrons exist in a real crystal lattice. For carbon nanotubes, these defects can be impurities, vacancies, edges and molecules connected to the nanotube walls. As long as there is no elementary excitation or annihilation at a defect point, the scattering is elastic and the electron only changes its momentum from k to $k + q$ with q depending on the defect potential $V(q)$. There is the possibility that one scattering event in a second-order Raman process is replaced by the aforementioned elastic scattering. In this case, the limitation of $q = 0$ is eliminated and many different phonon modes with $q \neq 0$ can contribute to the Raman process. The D band of CNTs is a good example of this process. It involves an inelastic scattering by

iTO phonons near the K point and an elastic inter-valley scattering by defect sites. The D-band frequency is dependent on the incident laser energy E_L [85]. With a laser excitation wavelength at 632.8 nm, it's around 1350 cm^{-1} .

It is important to note that the I(D)/I(G) ratio can be used to determine the defect density of carbon nanotubes and to evaluate material quality. More details are discussed in ref [86, 87, 88].

2D band

2D band (or G' band) is a second-order double-resonance Raman process in which the electron is scattered respectively by two phonons with opposite momentum q and $-q$ for the sake of momentum conservation. Its frequency is $2\omega_D$ lying between 2600 and 2700 cm^{-1} with strong dependence on laser excitation energy. Sometimes the G' band is observed to split into two peaks when two different van Hove singularities are involved in the process, one in resonance with the excitation energy and the other one in resonance with the scattered photon[89].

A typical Raman spectrum of semiconducting SWCNTs is shown in Figure 1.15.

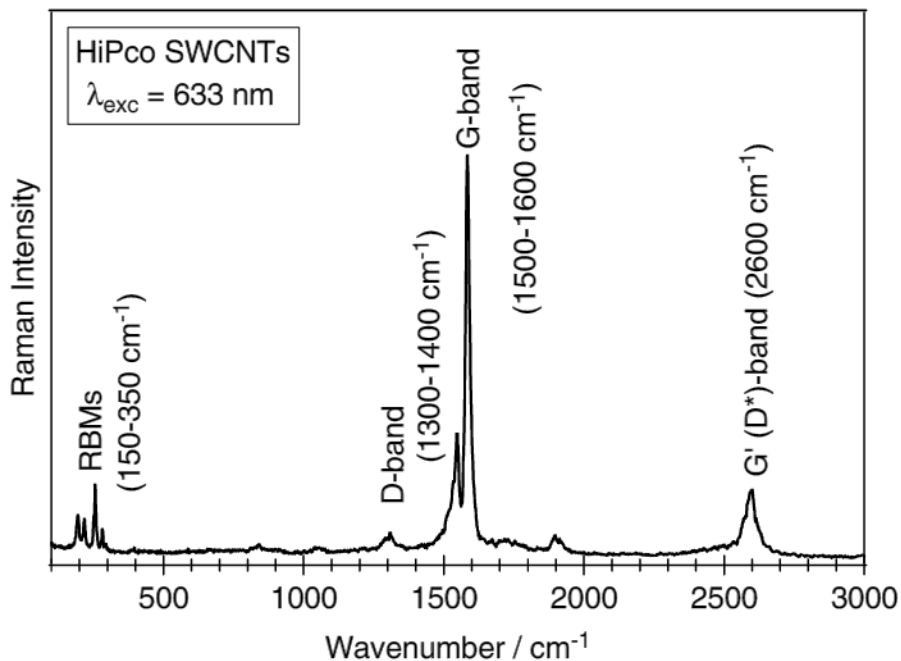


Figure 1.15: Raman spectrum of HiPco SWCNTs with a laser excitation wavelength at 633nm. The G band splits into two individual peaks. Figure is reprinted from ref [90].

1.2 Applications of SWCNT in organic solar cells

1.2.1 Synthesis and sorting of SWCNT

This section is mainly based on a few recent reviews[91, 92, 93].

Arc-discharge[16] and laser ablation[94] are the two earliest synthesis approaches for preparing SWCNTs. They both start from a solid carbon source and stimulate the evaporation of carbon atoms under critical experimental conditions such as high temperature and low pressure. They are almost not used anymore. Nowadays Chemical vapor deposition (CVD) is the dominant approach[95], which involves sending a hydrocarbon gas flow through a tube furnace with heated metal catalysts on which the reaction takes place. Many different kinds of catalysts were used in the CVD approach, among them the most representative one is the mixture of cobalt and molybdenum (CoMoCat). The production yield of CVD process has reached more than 90% with preferential synthesis of metallic or semiconducting SWCNTs. However, the SWCNTs prepared by large-scale CVD methods often contain contaminants that can influence CNT properties and thus require costly thermal annealing and/or chemical treatment for their removal[96]. These steps can introduce defects in CNT sidewalls and break the nanotubes into smaller segments. Generally, it is still not clear how to control chirality, diameter and purity by adjusting catalyst composition and process conditions. Up to now, the synthesized SWCNTs must undergo purification and/or separation processes.

Given the mixed nature and bundled structures of the as-synthesized SWCNTs, it is necessary to separate and disperse them in solvents using small molecules or polymers. This can be done via covalent and non-covalent ways[91]. The covalent bonding mostly involves chemical reactions such as grafting of carboxyl groups on the surface by oxidation. The covalent approach yields a higher dispersion stability but inevitably changes the intrinsic properties of SWCNTs and causes structural damage. Therefore the non-covalent approach is much more widely used. Despite a weaker dispersion stability, it is simple to operate and does little damage to the nanotubes. According to Fujigaya and Nakashima[91], most polymers non-covalently bind to the SWCNT surface through enthalpy-driven interactions such as $\pi - \pi$ conjugation, and they show a static dispersion able to survive filtration or dialysis. In contrast, small molecules and surfactants on the surface are in a dynamic equilibrium with their concentration in the bulk solution, therefore they are easily removed after filtration.

The most common type of polymer for SWCNT wrapping is the π -conjugated polymer. The mechanism of the selective dispersion is not fully understood yet, but from MD calculations it is assumed that π -conjugated polymers exhibit the selectivity for particular diameter or chirality by aligning the polymer backbone along the SWCNT surface with an dihedral angle that maximizes the interaction[97, 92, 98, 99]. One representative of π -conjugated polymers is polyfluorene (PFO). The PFO family has been greatly expanded by incorporating a large number of monomers into the molecular structure[100, 101]. The extraction of semiconducting SWCNTs by PFO derivatives features high yield and

easy procedures[102]. The high-quality of PFO wrapped SWCNTs has led to an enhanced efficiency of solar cells derived from these materials[103]. It is noteworthy that the PFO polymers might need to be removed for a better device performance in some applications. Recently, a few tailored polymers with specific bonds between monomer units which break during post-extraction treatment have been reported[104, 105].

Another example of π -conjugated polymers is poly(3-hexylthiophene) (P3HT) which has been extensively applied to organic photovoltaics. MD calculations showed that, aside from $\pi - \pi$ interactions, the sulfur atom also contributes to the interaction[106]. According to Pradhan et al., the $\pi - \pi$ interaction significantly improves the stability of the SWCNT/P3HT system and prevents photosensitization[107]. Lee and co-workers found that regioregular P3HT is able to selectively disperse semiconducting SWCNTs as well[108].

Other polymers used in SWCNT separation include aromatic polymers, cationic polymers, block polymers, pendant polymers and so on. A detailed description is available in the review paper[91].

1.2.2 SWCNT-based organic solar cells

SWCNTs, together with other nanocarbon materials, have been widely used in photovoltaic devices. Since POCAONTAS is focused on organic solar cells (OSCs), here we will give a very brief review on the OSC systems with SWCNTs. This section is mainly based on a few recent reviews[109, 93].

Regardless of the materials and configurations, all the excitonic solar cells need to fulfill the following steps for a substantial voltage output: (1) exciton generation from photon absorption, (2) exciton diffusion to the interface, (3) exciton dissociation into charge carriers, and (4) charge migration to the electrode. On the other hand, the undesired pathways which can cause a loss of energy include: (1) exciton recombination, (2) exciton trapping, and (3) exciton-exciton annihilation. All the optimizations of solar cell devices aim at promoting the four fundamental processes and/or suppressing the undesired pathways.

The devices with SWCNT-incorporated photoactive layers can be divided into two types: SWCNT/polymer conjugates with SWCNT being electron acceptors and SWCNT/fullerene blends with SWCNT being electron donors. For the first kind of device, Ren and co-workers demonstrated SWCNT/P3HT polymer bulk heterojunction solar cells with power conversion efficiency at 0.72%[110]. The open-circuit voltage V_{OC} and short-circuit current density J_{SC} can be modulated by the concentration of SWCNTs in the composite. They pointed out the near absence of metallic SWCNTs and the debundling effect of P3HT are the key reasons for a better performance. The system of SWCNT/P3HT has been intensively studied and modified in different ways. Ham et al. fabricated a planar SWCNT/P3HT heterojunction solar cell with ultralong nanotube arrays horizontally aligned. By doing this they suppressed the formation of bundled aggregates and tube-tube heterojunctions which are main obstacles for exciton dissociation into free charge carriers[111]. An efficiency as much as 3% was reached. The dispersion of CNT in the polymer matrix is also an important factor. Chang et al. demonstrated that the device performance strongly relies on the

interaction between solvent and SWCNT or polymer[112]. Functionalization of SWCNTs improves their solubility in organic media and thus results in a higher efficiency[113].

The second kind was first reported by Bindl et al.[114]. Highly purified semiconducting SWCNTs were used as near-infrared optical absorbers in heterojunction with electron acceptor C_{60} . This device showed a high external quantum efficiency (more than 12%) and power conversion efficiency at 0.6% in the NIR region. A large number of investigations were focused on the photophysics and further development of this system. A comprehensive study was done by Koleilat and co-workers[115]. They proposed three main factors limiting the efficiency of SWCNT-incorporated photo-active layers: (1) the residual high bandgap polymer traps the excitons within polymer-SWCNT matrix, (2) The small bandgap offset between SWCNT and C_{60} doesn't provide enough driving force for the exciton to split into electron and hole, and (3) The small exciton diffusion length around 5nm, which limits carrier extraction. To solve these problems, they did the following: (1) updated the solution sorting process with a reduction of the polymer content, (2) enhanced the internal field bias with a heavily doped region of C_{60} to move carriers away, and (3) fabricated a dense nanoporous mesh of SWCNTs by solution shearing method, which allowed the acceptor to infiltrate into the film and hence increased the interfacial area. A 10-fold improvement in performance was observed.

SWCNTs have also been used as transport materials for both electrons and holes in OSCs. Including them into fullerene-polymer solar cells brought a higher J_{SC} due to the efficient charge transfer between SWCNT and C_{60} [116]. This approach can be further developed with an elaborate design of the device structures. Chen and co-workers prepared SWCNT-polythiophene(PT) core-shell nanowires by growing PT around the 3D interconnected metallic SWCNTs. The electron donor PCBM filled into the openings of the network structure. With photoexcitation, the hole travels across the thin PT shell, is collected by SWCNT and transported to the electrode. The power conversion efficiency was raised to 3.07%[117]. Individual SWCNT layer were also used in OSCs. Compared with commonly used poly(3,4-ethylenedioxythiophene):polystyrene sulfonate (PEDOT:PSS) HTLs, they are more resistant to light-induced degradation. It was reported that an extra SWCNT layer on the cathodic side of the active layer yields a better efficiency[118]. When the orientation of SWCNT was aligned perpendicular to the electrode, the efficiency of P3HT/SWCNT/PCBM device approached 4.5%[119].

Although not directly related to the topic, it is worth mentioning that very recently semiconducting SWCNTs have been used as charge extraction layers in hybrid organic-inorganic perovskite solar cells. Very interestingly, they exhibited a fast hole extraction and slow recombination rate on $MAPbI_3$ active layers and thus further improved the device performance[120]. More information can be found in these review papers[93, 121].

Chapter 2

Principles of TENOM

The following chapter is based on the paper “*Advances in Tip-Enhanced Near-Field Raman Microscopy Using Nanoantennas*” published in *Chem. Rev.* (2017, 117 (7), pp 4945-4960).

Optical microscope has been widely used in natural sciences. Since its invention in the early 17th century, a large number of technological and manufacturing advances have continuously improved the image quality and reduced aberration. However, all glass-based microscopes are limited to an ultimate limit for spatial resolution, which results from the diffraction of light at the objective lens. This resolution limit originates from the wave nature of light, and are governed by physical laws. It is usually referred to as diffraction limit.

In confocal laser scanning microscopy, the diffraction limit is determined by the excitation and detection wavelength and the numeric aperture (NA) of the objective lens. In general, a shorter laser and detection wavelength together with a larger NA value will improve both lateral and axial resolution. Nevertheless, the best resolution achieved in this way still has the magnitude of few hundred nanometers, which is way larger than the size of single molecules or nanostructures. Therefore a higher resolution overcoming the diffraction limit is needed for the investigation of nanoscale materials. This required super-resolution can be achieved by both far-field techniques and near-field techniques. Representative far-field techniques include photoactivated localization microscopy (PALM), stochastic optical reconstruction microscopy (STORM) and stimulated emission depletion microscopy (STED). Their applications are mainly limited to fluorescent samples. Near-field techniques, such as (elastic) scattering scanning near-field optical microscopy (s-SNOM) and tip-enhanced near-field optical microscopy (TENOM) could be applied to a broader range of samples and spectroscopic signals. However, since they exploit evanescent waves existing only in the vicinity of the tip and sample, they can only detect the properties of a sample surface but not of bulk materials.

This chapter will discuss the basic principles of TENOM, together with some recent developments and findings in this field. In the first section, we express the propagation of light in the angular spectrum representation and introduce the important concept of

the diffraction limit. In the second section, we start with the principles of optical nano-antennas and then describe the electrical near-field distribution of them, which leads to sub-diffraction spatial resolution. Afterwards we will focus on the gap plasmon mode, in which the tip is placed above a metallic sample substrate with a ~ 1 nm tip-sample distance, from which stronger field confinement and improved spatial resolution can be achieved. In the last section, we discuss the signal enhancement in different applications based on electromagnetic field enhancement. Recently, it has been demonstrated that the conventional picture of electromagnetic field enhancement doesn't capture the whole physics. Several newly developed signal-enhancement mechanisms such as the optomechanical coupling will be briefly reviewed.

2.1 The diffraction limit derived by the angular spectrum representation

This section is based on the book written by L. Novotny[122]. Applying Heisenberg's uncertainty principle to photons, we have:

$$\Delta p_x \cdot \Delta x \geq h \quad (2.1)$$

Substituting momentum p_x with wavevector k_x with the relationship $p_x = \hbar k_x$, we have:

$$\Delta k_x \cdot \Delta x \geq 2\pi \quad (2.2)$$

This also applies for y and z directions. From equation 2.2 we could see that a larger wavevector range Δk_x leads to a smaller position range Δx , in other words, a higher spatial resolution.

From this perspective, a certain resolution limit of optical microscopy corresponds to a limited range of wavevectors which are able to travel from source to detector. This means that to what extent we can improve the spatial resolution depends on how much we can avoid the loss of spatial frequencies during light propagation. A common approach to mathematically describe the light propagation is the angular spectrum representation, in which an optical field is divided into plane waves and evanescent waves.

The samples we observe with optical microscope can be regarded as the combination of many point light sources. For simplification, in the following discussion we only consider a single point source of light. Figure 2.1 is a schematic of light propagation. We define that the light travels along the z direction. The light source is located at $(x, y, 0)$ with the generated electric field $\mathbf{E}(x, y, 0)$. We use the angular spectrum representation to calculate the electric field in the plane perpendicular to the light propagation with distance z to the light source. It is easier to do this in reciprocal space. The Fourier transformation of the

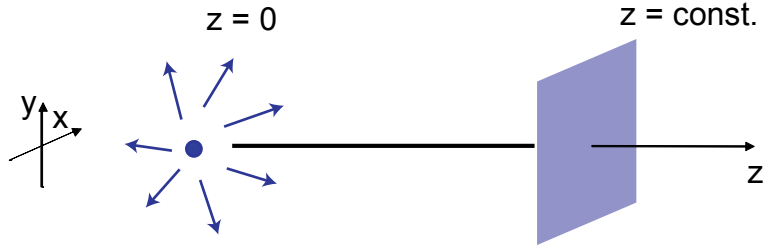


Figure 2.1: Schematic of light propagation from a single point source located at $(x, y, 0)$. The electric field at a random point $\mathbf{E}(x, y, z)$ can be described using the angular spectrum representation.

electric field \mathbf{E} at z is expressed as:

$$\hat{\mathbf{E}}(k_x, k_y; z) = \frac{1}{4\pi^2} \iint_{-\infty}^{+\infty} \mathbf{E}(x, y, z) e^{-i(k_x x + k_y y)} dx dy \quad (2.3)$$

Where x, y, z are real space coordinates and k_x, k_y, k_z are the reciprocal space coordinates. Similarly we can do an inverse Fourier transformation which gives:

$$\hat{\mathbf{E}}(x, y; z) = \iint_{-\infty}^{+\infty} \hat{\mathbf{E}}(k_x, k_y; z) e^{i(k_x x + k_y y)} dk_x dk_y \quad (2.4)$$

Assuming the surrounding medium is homogeneous, isotropic, linear and source-free, the optical field should satisfy the Helmholtz equation:

$$(\nabla^2 + k^2)\mathbf{E}(r) = 0 \quad (2.5)$$

where k is the magnitude of the wavevector given by $k = 2\pi n/\lambda$. λ is the wavelength and n is the refractive index.

The wavevector k_z determines the propagation in this direction. k_z is expressed as:

$$k_z = \sqrt{k^2 - k_y^2 - k_x^2} \quad (2.6)$$

Inserting equation 2.4 and 2.6 into equation 2.5, one could find how the Fourier spectrum changes along z direction:

$$\hat{\mathbf{E}}(k_x, k_y; z) = \hat{\mathbf{E}}(k_x, k_y; 0) \cdot e^{\pm i k_z z} \quad (2.7)$$

The sign \pm represents positive z and negative z directions. This equation means that, the Fourier spectrum in a plane located at z can be described with the electric field in the

object plane multiplied with a propagator $e^{\pm ik_z z}$. Thus the real space electric field for an arbitrary z can be calculated:

$$\mathbf{E}(x, y, z) = \iint_{-\infty}^{+\infty} \hat{\mathbf{E}}(k_x, k_y, 0) e^{i(k_x x + k_y y \pm k_z z)} dk_x dk_y \quad (2.8)$$

This is the so-called angular spectrum representation.

In a purely dielectric medium, n is a fixed, real and positive value. Depending on the value of k_z , there are two cases:

- $k_x^2 + k_y^2 \leq k^2$, k_z is real. The amplitude oscillates but doesn't decay with z . These waves are propagating plane waves. They belong to the far-field of the light source and could be received by a detector.
- $k_x^2 + k_y^2 > k^2$, k_z is imaginary. The propagator $e^{ik_z z}$ turns into $e^{-k_z z}$, indicating that the amplitude will decay exponentially with z . These waves only exist in the vicinity of the light source (near-field) and can't propagate to the detector in far-field optical microscopy. Therefore they are named evanescent waves.

Equation 2.8 can be rewritten into the superposition of plane and evanescent waves:

$$\mathbf{E}(x, y, z) = \iint_{k_x^2 + k_y^2 \leq k^2} \hat{\mathbf{E}}(k_x, k_y, 0) e^{i(k_x x + k_y y) e^{i|k_z z|}} dk_x dk_y + \iint_{k_x^2 + k_y^2 > k^2} \hat{\mathbf{E}}(k_x, k_y, 0) e^{i(k_x x + k_y y) e^{-|k_z z|}} dk_x dk_y \quad (2.9)$$

In confocal microscopy, the evanescent waves with large spatial frequencies decay very fast and can't reach the detector. Thus the spatial information they carry is lost and we have a limited spatial resolution. For plane waves, the maximum of the in-plane wave vector component (equation 2.2) is $k_x = 2\pi n/\lambda$ (See equation 2.6), so the range of k_x is twice of the maximum, $\Delta k_x = 4\pi n/\lambda$. Taking this into equation 2.2 we have the minimum uncertainty of position, i.e. the spatial resolution in x direction:

$$\Delta x_{min} = \frac{2\pi}{\Delta k_{x,max}} = \frac{\lambda}{2n} \quad (2.10)$$

However, not all the plane waves can be detected due to the limited collection angle of our objective lens and other optical elements. The collection ability of an objective lens is characterized by the parameter numerical aperture (NA) given by:

$$NA = n \cdot \sin\alpha \quad (2.11)$$

Here n is the refractive index of the medium between lens and focal plane, α is the maximal half-angle of the cone of light that can enter or exit the lens.

2.1 The diffraction limit derived by the angular spectrum representation 35

It's straightforward that the maximum k_x can be collected by an objective lens with NA is :

$$k_{x,max} = k \cdot \sin\alpha = \frac{2\pi}{\lambda} \cdot NA \quad (2.12)$$

Then the spatial resolution in equation 2.15 has changed into:

$$\Delta x_{min} = \frac{2\pi}{\Delta k_{x,max}} = \frac{\lambda}{2NA} \quad (2.13)$$

This is a theoretical limit of the best spatial resolution. Based on the criteria of definition, there are different formulations of the resolution limit. Among them the most common one is the limit derived by Ernst Abbe in 1873. His derivation is built on the system of two parallel, dipolar emitters with the dipole orientation perpendicular to the optical axis. They are regarded as point sources. The emitted light is focused by the objective lens and imaged onto the image plane, as shown in Figure 2.2. The diffraction pattern from a single point source on the image plane is referred to as an Airy disk, which has a bright spot in the center and alternating dark and bright rings along the radial direction.

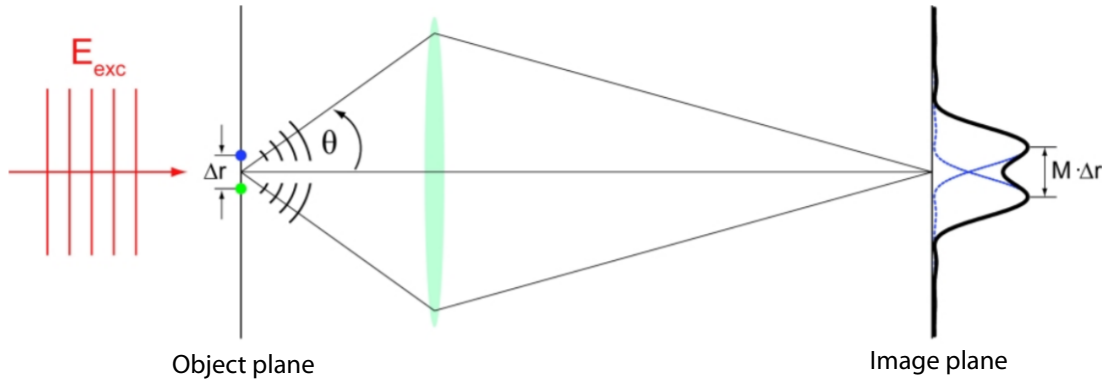


Figure 2.2: Illustration of the Abbe limit in optical microscopy. Two point dipoles are located in the object plane with distance Δr . Their emitted light is collected by the objective lens and focused on the image plane. Due to diffraction, the image of a point source on the image plane consists of a central bright spot and alternating bright and dark rings, referred to as Airy disk. These two point dipoles can be distinguished when the center of the bright spot of one dipole spatially overlaps with the first dark ring of another dipole's Airy disk.

In the far-field (Fraunhofer diffraction), the airy disk is described by the following equation:

$$I(x) \propto 2 \frac{J_1(p)^2}{p} \quad p = \frac{2\pi NA}{M\lambda} x \quad (2.14)$$

Where M is the magnification of the objective lens, NA is the numeric aperture and J_1 is the first order Bessel function. The radius of the central bright spot in the Airy disk is:

$$\Delta x = 0.61 \frac{M\lambda}{NA} \quad (2.15)$$

Abbe stated that two point sources can still be distinguished when the first dark ring of one emitter is located at the center of the bright spot of another one. If the distance between two point sources is Δr , in the image plane they will be displaced by $M\Delta r$. They can be distinguished only when:

$$M\Delta r \geq 0.61 \frac{M\lambda}{NA} \Rightarrow \Delta x \geq 0.61 \frac{\lambda}{NA} \quad (2.16)$$

This is denoted as the Abbe limit. It is worth mentioning that the resolution limit for the z-direction, i.e. the least distinguishable distance between point sources in different object planes is:

$$\Delta r_z \geq 2 \frac{n\lambda}{NA^2} \quad (2.17)$$

In TENOM, one utilizes a nanoscale object which is located very close to the sample in order to achieve efficient coupling between the object's near-field and the emitter, and the emitter's near-field and the object. As a result, a much larger range of spatial frequencies arrive at the detector and the spatial resolution is significantly improved. This nanoscale object is often called optical antenna and its principles will be discussed in the next section.

2.2 Principles of optical antennas

2.2.1 Characteristics of an optical antenna

TENOM exploits the extremely short-ranged near-field interaction between a pointed probe and the sample. The task of efficiently coupling the tip's near-field to the far-field, in which the laser source and the detector are located, is the function of an antenna. More specifically, an optical antenna is defined as an object that converts free-propagating optical radiation to localized energy and *vice versa*[123, 124, 125] (see Figure 2.3). For a comprehensive characterization of an optical antenna, classical antenna theory can be used. To simplify the description of the antenna parameters, a dipole-like behavior of receiver and transmitter is typically assumed.

Two antenna enhanced processes, namely absorption and emission of light, have to be considered in order to get a complete description of the optical antenna function. Enhanced absorption can be quantified in terms of the antenna aperture A , which corresponds to the absorption cross section σ in presence of the tip. It describes the efficiency with which the incident radiation is captured to excite the receiver with the power P_{exc} , where I is the intensity of the radiation with the polarization \mathbf{n}_{pol} incident from the direction (θ, ϕ) corresponding to $A(\theta, \phi, \mathbf{n}_{pol}) = P_{exc}/I = \sigma_A(\theta, \phi, \mathbf{n}_{pol})$. The tip enhances the field at the

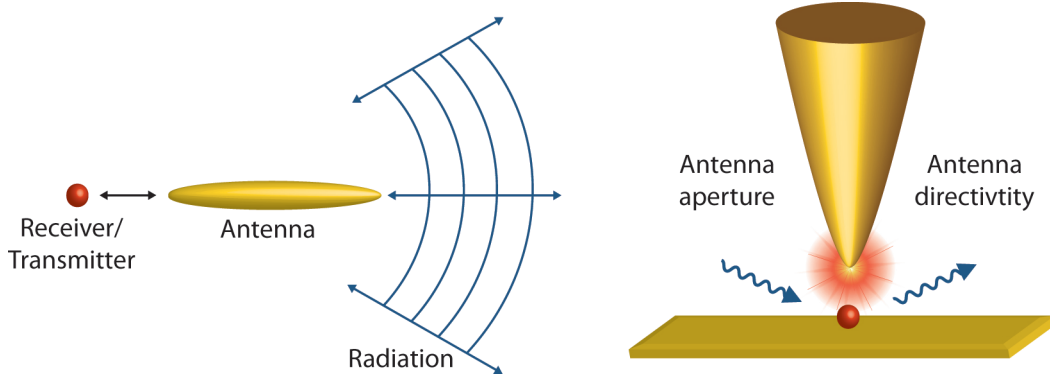


Figure 2.3: Left: Optical antennas convert free propagating electromagnetic radiation in the far-field to strongly localized near-fields and vice versa. Right: The optical antenna can be described by its functional parameters aperture and directivity. Both parameters typically depend on the frequency of the incident and the scattered light. From a functional perspective, the antenna is formed by both the scanning probe and the sample substrate.

absorber, and by defining the field in the absence of the tip as \mathbf{E}_0 and in the presence of the tip with \mathbf{E} the absorption cross section becomes

$$\sigma = \sigma_0 \frac{|\mathbf{n}_p \cdot \mathbf{E}|^2}{|\mathbf{n}_p \cdot \mathbf{E}_0|^2} \quad (2.18)$$

Here \mathbf{n}_p is the orientation of the absorption dipole and the subscript “0” indicates the absence of the antenna. Equation 2.18 shows that the absorption process depends on the incident direction and polarization of light. Neglecting their vectorial character or assuming the same direction of enhanced and non-enhanced fields, the absorption enhancement can then be expressed by the local field enhancement factor $f = E/E_0$ as $\sigma/\sigma_0 = f^2$. For metallic nanoantennas, particularly strong local fields can result in the optical regime from localized surface plasmon resonances, collective electron oscillations that are controlled by their shape and their material composition (see below).

A practical way to characterize the enhanced emission is the antenna efficiency, which is defined in equation 2.19. It describes the ratio between the total power dissipated by the antenna P and the radiative power P_{rad} . The total power P is composed of P_{rad} and the power dissipated through other channels, for example heat P_{loss} [124].

$$\epsilon_{rad} = \frac{P_{rad}}{P} = \frac{P_{rad}}{P_{rad} + P_{loss}} \quad (2.19)$$

The antenna’s ability to emit the radiated power into a certain direction can be measured by the directivity D . It considers the angular power density $p(\theta, \phi)$ with θ and ϕ as the angles of the direction of observation following $D(\theta, \phi) = \frac{4\pi}{P_{rad}}p(\theta, \phi)$. By taking the

polarization into account, one can define the partial directivities as

$$D_\theta(\theta, \phi) = \frac{4\pi}{P_{rad}} p_\theta(\theta, \phi), \quad D_\phi(\theta, \phi) = \frac{4\pi}{P_{rad}} p_\phi(\theta, \phi) \quad (2.20)$$

with p_θ and p_ϕ as normalized angular powers.

The antenna gain G combines the efficiency and directivity of an antenna to yield the radiation relative to the total power as $G(\theta, \phi) = \epsilon_{rad} D(\theta, \phi)$.

Absorption and emission at the same optical frequency can be connected following the reciprocity theorem. This leads to a relationship between the excitation rate Γ_{exc} and its spontaneous emission rate Γ_{rad} .

$$\frac{\Gamma_{exc,\theta}(\theta, \phi)}{\Gamma_{exc,\theta}^0(\theta, \phi)} = \frac{\Gamma_{rad} D_\theta(\theta, \phi)}{\Gamma_{rad}^0 D_\theta^0(\theta, \phi)} \quad (2.21)$$

The index θ refers to one polarization state, but can also be denoted ϕ , which corresponds to a rotation of the polarization by 90° . Neglecting the vectorial character, the spontaneous emission rate enhancement can be expressed by the local field enhancement factor $f = E/E_0$ as $f^2 = \Gamma_{rad}/\Gamma_{rad}^0$ corresponding to the relation for the absorption rate enhancement $f^2 = \Gamma_{exc}/\Gamma_{exc}^0$. Various studies have investigated the field enhancement factor for different antennas and configurations, and values ranging from $f = 2 - 5$ for single spherical particles and up to 1000 for optimized antennas have been reported[126, 127, 128, 129].

Importantly, the discussed antenna parameters will show a pronounced frequency dependence in most cases that can vary substantially between the incident and the emitted frequencies. Examples include resonant antenna structures that feature distinct spectral modes such as metallic nanospheres or nanorods.

In general, three different contributions to the local field enhancement provided by an optical antenna are currently being discussed. First, the lightning rod effect which is due to the geometrical singularity represented by the tip that leads to the spatial confinement of the surface charge density at the apex of a tip or tip-like structure[130]. This process is essentially non-resonant and will depend primarily on the electrical conductivity of the tip material at the frequency of light used in the experiment. Second, the excitation of localized surface plasmon resonances (LSPRs) in metallic nanostructures such as nanospheres and nanorods which depends on the frequency of incident and Stokes-scattered light. And third, length related antenna resonances that occur if the length of the antenna is a multiple of half the wavelength of light. At optical frequencies metals are not perfect conductors and therefore an effective scaling relation has to be used to connect the effective wavelength λ_{eff} with the incident wavelength λ . The effective wavelength shows a linear behavior with the plasma wavelength of the metal λ_p and $n_{1,2}$ as constants that depend on geometry and dielectric properties $\lambda_{eff} = n_1 + n_2 \left(\frac{\lambda}{\lambda_p} \right)$ [131].

2.2.2 Near-field of optical antennas

The antenna's near-field distribution determines the spatial resolution, the signal enhancement and the observed image contrast. In general, the enhanced fields of the optical antenna are highly dependent on the shape, material composition and structure of the used antenna-substrate system. In most cases, the resulting near-field distribution is strongly non-uniform regarding magnitude and polarization as well as phase. Numerous theoretical studies have been performed to characterize the field distribution and the corresponding enhancement for different conditions[132, 133, 134, 135].

The parameters in the aforementioned section show that the field enhancement factor depends on the directivity D and the polarization of the incoming light. For semi-infinite cone-like tip structures, field enhancement is highest when the polarization is parallel to the long axis of the antenna[136, 137, 132]. But the tip also modifies the polarization with respect to the incoming field. Figure 2.4 shows the simulated distribution of the z and x components of the field enhancement in the (xy) plane. Here, the heterogeneity of the near-field becomes visible. While the z component (Figure 2.4(c)) is highly localized beneath the tip, the x component (Figure 2.4(b)) shows two weaker lobes. Especially the in-plane modes result in a spatially heterogeneous polarization which can complicate the contrast formation.

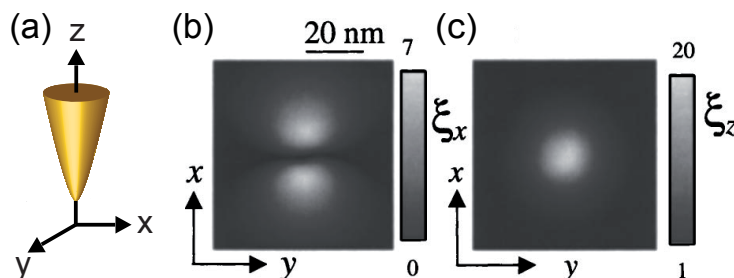


Figure 2.4: (a) System of reference for the x (b) and z (c) component of the field enhancement $\xi_{x,z} = |E_{x,z}| / |E_0|$ on the substrate plane ($z = 0$) for a silver tip with resonant excitation ($\lambda = 505$ nm) and a tip-substrate distance of 2 nm, calculated by Demming et al.[133].

Recently, several studies have been performed on e.g. carbon nanotubes[138, 139] and transition metal dichalcogenide monolayers[140, 141], taking advantage of the heterogeneous polarization of the tip to probe and distinguish differently polarized transitions. Moreover, the polarization sensitivity of both antenna aperture and directivity can be exploited for polarization-selective enhancement[142, 143].

Aside from dielectric substrates, metallic substrates can also be used. In this case, electromagnetic coupling between the surface charges in the tip and the induced charges in

the substrate takes place, and for small distances below 10 nm, a coupled mode named gap mode can arise, which can confine the plasmonic fields substantially below the geometrical size of the tip. It will be introduced in the next section.

2.2.3 Gap plasmon mode

For dielectric sample substrates, the spatial resolution observed in TENOM is mostly determined by the geometrical size of the tip and the tip-sample distance, which defines the lateral extent of the enhanced fields (10 - 20 nm)[144, 145, 8, 146]. From a functional perspective, on the other hand, the concept of an antenna as a (metal) structure that converts free-propagating optical radiation into localized energy and vice versa, can directly be extended to include also the sample substrate. Of particular importance are the so-called gap mode configurations (see ref [147, 148, 149, 150, 151]), in which the tip is placed above a metallic sample substrate separated by an extremely small gap distance on the order of one nanometer. Upon illumination of the tip with a focused laser beam, a surface charge density is induced in the tip apex which can be approximated by a point dipole. Because of the proximity of tip and metal substrate, mirror charges are accumulated at the surface of the metal substrate that can be described by an image dipole[152]. Upon approaching the tip, both the tip apex plasmon mode and the surface plasmon modes cease to exist independently, and a new hybrid mode forms, the so-called gap plasmon mode[151] (see Figure 2.5).

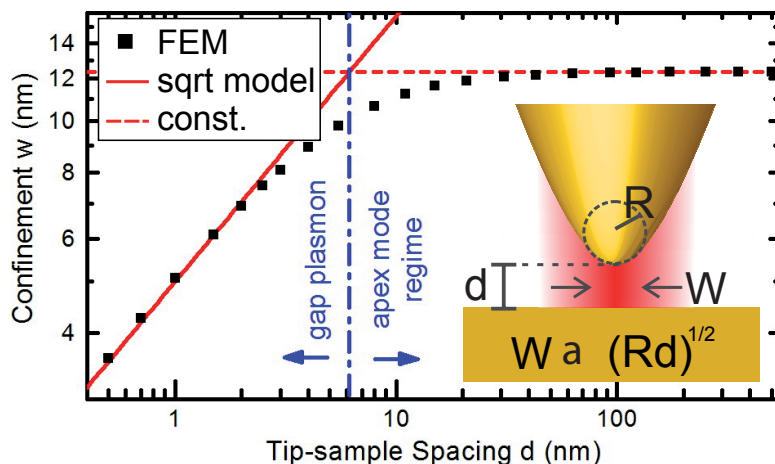


Figure 2.5: Lateral confinement w of the intensity $|E|^2$ obtained as full width at half-maximum from cross-sections through simulated field patterns 0.2 nm away from the apex for different tip-sample spacings d . A square root model for the gap plasmon extent, $w = A\sqrt{Rd}$, was fitted to the data with tip - sample spacing $d \leq 2$ nm, shown as the solid red line. For $R = 10$ nm an optimum value of $A = 1.57$ is found. The red dashed line represents a constant fit to the data with tip - sample spacing $d \geq 100$ nm. Adapted from ref [151].

Compared to dielectric substrates that do not support the formation of a gap mode, far stronger confinement of the field is obtained in the case of metallic substrates, leading to substantially improved spatial resolution[135, 8, 153, 151](see Figure 2.5). At the same time, far higher field enhancement factors can be achieved, which relates to the fact that in surface-enhanced Raman scattering (SERS) the largest enhancement is observed for interstitial sites and small nanogaps, for instance, in metal particle dimers[154, 155, 156]. As a result, gap mode configurations allows confining light to smaller dimensions than the tip diameter.

From the classical electrodynamic description, both electric field enhancement and spatial confinement will continuously increase upon decreasing the tip-sample distance. In other words, a minimized distance is expected to provide the best spatial resolution and signal enhancement. However, this is not true for very small separations due to quantum and atomistic effects, which can significantly alter the plasmonic response of the system. According to Savage et al.[157], 0.3 nm is the smallest tip-sample distance for classical electrodynamics to hold. A quantitative description of the lateral mode confinement in the gap just below the apex was derived in a recent paper[151] (see Figure 2.5). Their simulation results showed that when $0.5 \text{ nm} \leq d \leq 2 \text{ nm}$, the lateral confinement w is proportional to the square root of both the probe's apex radius of curvature R and the gap separation d with the relationship $w = A\sqrt{Rd}$, which was first proposed by Rendell et al.[158].

The first quantum phenomenon influencing the plasmon resonance is the spill-out of electrons. Quantum mechanical treatments such as the Jellium model show that the probability density of electrons extends outside the metal surface, exponentially decaying with distance[159]. This spill-out of electrons allows for electron tunneling accross junctions at separations smaller than $\sim 1 \text{ nm}$, thereby quenching the local field enhancement provided by the gap plasmon[160]. At the same time, a charge transfer plasmon can form with different spectral characteristics.

The second quantum phenomenon worth mentioning is the nonlocal screening of the electric field. Nonlocal screening[161] refers to the fact that, because of electron-electron interactions, the motion of the conduction electrons at a given point in space depends not only on the field applied at that position but also on fields at other locations[160]. The nonlocal screening prevents sharp charge localization at interfaces and is therefore important for small particles[162] and narrow gaps[163]. Time-dependent density functional theory (TDDFT) calculations showed that the plasmon-induced surface charge density is smeared out over quite a broad region of about 10 Bohr around the surface[164]. The width of the smeared plasmon-induced electron density is determined by the electron spill-out. An increased spill-out density will introduce a further smearing of the induced electron density and can thus reduce the field enhancements even further, relative to classical results.

Electron spill-out and the associated non-local screening will create an “effective” gap distance that also differs from the geometrical value[160]. For gap distances of less than 1 nm, electron tunneling across the gap at optical frequencies will further modify the plasmonic response of the system with respect to the classical description. Due to the

screening of localized surface charges by quantum tunneling and a consequent reduction in the plasmonic coupling, the resonances shift towards blue. This phenomenon explains the observed smooth transition of the plasmonic response upon variation of the geometry from a subnanometer gap to touching metal surfaces[160]. Electron tunneling provides an effective “charge transfer” channel, neutralizing the bonding-plasmon-induced charges of opposite signs across the gap and thus quenching the field enhancement[164].

Although the quantum phenomena discussed above are expected to limit the field confinement and signal enhancement, atomic-scale features appear to have the potential to reverse this effect. Barbry et al. found that atomic features such as protruding atoms do localize electromagnetic fields down to atomic-scale dimensions, showing resonant (plasmonic) and nonresonant (lightning-rod effect) field enhancement and beating the typical plasmonic confinement imposed by the nanoparticle size[165]. This means that in a gap plasmon mode, the exact atomistic structure of the junction could induce extra extremely localized “hot spots”. In another recent theoretical study on plasmon-enhanced microscopy, Trautmann and co-workers suggested that protrusions as small as a single atom found on plasmonic particles might act as probing tips[166]. It was also reported that light-activated mobilization of surface atoms in a plasmonic hot spot leads to the formation of additional “picocavities” in SERS measurements[167], which could provide an extreme optical confinement yielding a factor of 10^6 enhancement of optomechanical coupling between the picocavity field and vibrations of individual molecular bonds (see also section 2.3.2). In summary, the details of the interplay between quantum and atomistic effects and their actual contribution to the spatial resolution and signal enhancement observed in experiments are not clearly understood yet.

2.3 Signal enhancement

The locally enhanced electric field from the nanoantenna can be used for different processes, including not only the optical response such as Raman scattering and photoluminescence (PL), but also optoelectronic signals like photocurrent (PC) and electroluminescence (EL). In this section, we will first discuss the relationship between signal enhancement and field enhancement f (See section 2.2.2) for these processes based on electromagnetic enhancement.

More recently, the achieved subnanometer spatial resolution and the observed nonlinear power dependence of the signal in near-field measurements[150], especially in TERS, have arisen great interest because they could not be directly explained by conventional electromagnetic models. This stimulates an improved theoretical understanding of the electric fields on very short length scales in the context of quantum plasmonics (see section 2.2.3). Therefore, in the second section we provide a brief overview of recently proposed signal-enhancement mechanisms that go beyond the f^4 rule.

2.3.1 Signal enhancement based on electromagnetic field enhancement

Tip-enhanced Raman scattering (TERS)

In the case of spontaneous Raman scattering, the detected signal depends on the product of the transition rates $\Gamma_{exc,\theta}(\theta, \phi)\Gamma_{rad}$, the directivity $D_\theta(\theta, \phi)$ and the detection efficiency $\eta_\theta(\theta, \phi)$ of the experimental setup. Furthermore, all these quantities will be wavelength dependent. The total signal at a given wavelength then results from angular integration:

$$S_{Raman,\theta} = 1/(4\pi) \int_0^{2\pi} \int_0^{\phi_m} \Gamma_{exc,\theta}\Gamma_{rad}D_\theta\eta_\theta \sin\theta d\theta d\phi. \quad (2.22)$$

The ϕ integration is limited to the maximum collection / detection angle $\phi_m = a\sin(NA/n)$ determined by the numerical aperture NA of the microscope objective and the refractive index n of the enclosing medium. In an experiment, the excitation profile and angular detection range should match the antenna aperture and directivity[7, 168].

It should be noted that the tip can substantially modify the spectral shape of emission, because of the frequency dependence of the antenna gain G (See section 2.2.1). In case of sharp antenna resonances and emission with large spectral bandwidth, this effect will be quite strong. As a result, both antenna-enhanced Raman and PL can be quite different from their far-field counterparts.

Often, the angular and polarization dependence in equation 2.22 is neglected together with the vectorial character of the electric fields in equation 2.18. As a consequence, the total signal enhancement M is found to scale approximately with the fourth power of the field enhancement for small differences between the excitation and emission wavelengths, assuming that the field enhancement at the tip does not depend sensitively on the wavelength:

$$M_{Raman} \approx \Gamma_{exc}/\Gamma_{exc}^0\Gamma_{rad}/\Gamma_{rad}^0 \approx f^4 \quad (2.23)$$

A semiquantitative analysis of the signal levels that can be expected in TERS from different sample materials and in different experimental geometries was given in ref [168]. The authors discussed how high a signal level could actually be expected within the physical limitations set by field enhancement, damage threshold, tip scattering efficiency, collection and detection efficiency, and the Raman scattering cross section of the sample material for different experimental configurations.

Tip-enhanced fluorescence

Different from TERS, the tip-enhanced fluorescence or photoluminescence intensity is determined by the excitation rate Γ_{exc} and the quantum yield q which denotes the probability of a radiative decay with $q = \Gamma_{rad}/(\Gamma_{rad} + \Gamma_{non-rad})$ (See section 1.1.3). The

excitation rate enhancement scales with f^2 as in Raman scattering. Therefore the total signal enhancement can be expressed as:

$$M_{flu} \approx (\Gamma_{exc}/\Gamma_{exc}^0)(q/q^0) \approx f^2 \frac{q}{q_0} \quad (2.24)$$

We note that the tip doesn't only enhance the radiative decay rate but can also enhance the non-radiative decay rate by metal-induced quenching when it's very close to the sample. From equation 2.24 we could see that TENOM is most suitable for emitters with low intrinsic quantum yield q_0 such as carbon nanotubes and fullerenes. If $q_0 \ll 1$, the radiative rate can be neglected compared to the non-radiative rate, then we have $q = \Gamma_{rad}/\Gamma_{non-rad}$. In this case, equation 2.24 can be rewritten as:

$$M_{flu} \approx (\Gamma_{exc}/\Gamma_{exc}^0)(\Gamma_{rad}/\Gamma_{rad}^0) \approx f^4 \quad (2.25)$$

For emitters with a very high intrinsic quantum yield $q_0 \sim 1$, the quantum yield can't be further enhanced by the tip, so we have:

$$M_{flu} \leq \Gamma_{exc}/\Gamma_{exc}^0 \approx f^2 \quad (2.26)$$

The sign \leq is due to the possible quenching.

Photocurrent (PC) and Electroluminescence (EL)

Photocurrent and electroluminescence only benefit from excitation enhancement and radiation enhancement respectively, therefore their signals are expected to have a smaller enhancement than optical signals, scaling with the square of field enhancement f :

$$M_{PC} \approx \Gamma_{exc}/\Gamma_{exc}^0 \approx f^2 \quad M_{EL} \approx \Gamma_{rad}/\Gamma_{rad}^0 \approx f^2 \quad (2.27)$$

In the case of electroluminescence, metal-induced quenching can also take place and further decrease the actual enhancement.

A stronger signal enhancement comes with a better spatial resolution, because the field enhancement factor f is not constant but depends on the position with respect to the tip end. Assuming the tip is radially symmetric and f_0 is the maximum field enhancement factor underneath the tip, the distance dependence of f can be approximately described by a Gaussian function:

$$f(r) = f_0 \cdot e^{-\frac{r^2}{2w^2}} \quad (2.28)$$

where r is the distance and w is the peak width. For a given tip-sample configuration w is fixed.

If the signal enhancement scales with $M \sim f^4$, as in the case of Raman scattering, then

$$I_{Raman} \propto f^4 \propto e^{-\frac{2r^2}{w^2}} = e^{-\frac{r^2}{2(\frac{1}{2}w)^2}} \quad (2.29)$$

This is still a Gaussian function and the peak width of Raman signal w_{Raman} is $\frac{1}{2}w$.

If the signal enhancement scales with $M \sim f^2$, as in the case of photocurrent, then

$$I_{PC} \propto f^2 \propto e^{-\frac{r^2}{w^2}} = e^{-\frac{r^2}{2(\frac{1}{\sqrt{2}}w)^2}} \quad (2.30)$$

the peak width of the photocurrent signal w_{PC} is $\frac{1}{\sqrt{2}}w$. Obviously we have $w_{PC} = \sqrt{2}w_{Raman}$, meaning that the spatial resolution of the Raman signal is $\sqrt{2}$ times better than that of the photocurrent signal. This is experimentally proved by tip-enhanced photocurrent measurements on single carbon nanotubes[15].

2.3.2 Other proposed enhancement mechanisms

Optomechanical Coupling

In the conventional electromagnetic enhancement mechanism, the optical antenna and scatterer/emitter are treated as independent entities. Very recently, both Roelli et al. and Schmidt et al. studied the coupling between them in plasmon-enhanced Raman scattering[169, 170]. In a microscopic view, the Raman scatterer represents a polarizability that is periodically modulated at its vibrational frequency. This oscillating polarizability will in turn modulate the energy of the plasmon resonance of the metallic nanostructure that couples back to the vibrational excitation inducing a non-linear feedback.

If the plasmon frequency ω_p is substantially larger than the vibrational frequency Ω_v and there is no electronic resonances in the sample material, the vibrational displacement x_v will cause a shift of the plasmon frequency that can be described to the first order as:

$$\omega_P(x_v) = \omega_p - G_v x_v \quad (2.31)$$

This is comparable with optomechanical systems with G_v as the optomechanical coupling rate. Since the polarizability of the molecule depends on the vibrational mode displacement, G_v can be expressed with $\delta\alpha/\delta x_v$ and the mode volume of the optical cavity V_m :

$$G_v = \omega_P \left(\frac{\delta\alpha}{\delta x_v} \right) \frac{1}{V_m \epsilon_0} \quad (2.32)$$

In turn, the plasmon acts back on the vibration through a time-dependent generalized force:

$$F_p(t) = \hbar G_v n_p(t) \quad (2.33)$$

Where n_p is the instantaneous plasmon occupancy.

Although the quality factor of plasmonic resonances is typically low ($Q \approx 10$) due to efficient radiative and non-radiative damping, this can be compensated in part by the extremely small mode volume represented by the plasmonic fields[169]. The corresponding quantum mechanical Hamilton operator of the coupled system is equivalent to that originally developed in the framework of cavity optomechanics. In this context, a typical optical

cavity is formed by two highly reflective mirrors, with circulating photons inside, exerting a radiation pressure on them. Connecting one of the mirrors to a mechanical oscillator, e.g. an AFM cantilever that acts as a spring, the optical force is translated into a mechanical excitation. The mechanical motion shifts the resonance frequency of the cavity, modifying the intensity of the circulating light and therefore the radiation pressure. This feedback mechanism is termed optomechanical backaction. Schematics of the optomechanical systems are shown in Figure 2.6. The delay in the plasmonic cavity field response to changes in the resonance frequency results in a force component out of phase with the molecular vibration, leading to either damping or amplification of the molecular vibration. Roelli and co-workers found that an excitation laser blue-detuned from the plasmon resonance can significantly amplify the molecular vibration and features a non-linear enhancement which is not predicted in the conventional picture.

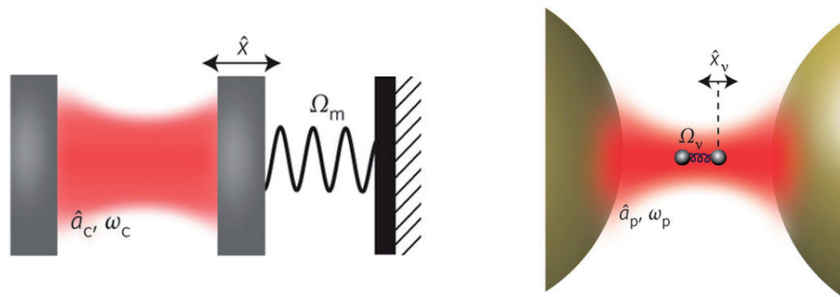


Figure 2.6: Schematics of optomechanical systems. Left: An optical cavity with one edge mechanically connected to a mirror. Right: A Raman-active molecule located in a plasmonic hot spot. The vibrational mode is sketched as two masses linked by a spring. Figure is adapted from ref [169].

Electric field gradient

Raman spectra of materials subject to strong electric field gradients, such as those present near a metal surface, can show significantly altered selection rules. It was found by Ayars et al. that strong electric field gradients could change the Raman spectra of materials. Selection rules can be significantly altered for a Raman scatterer near a metal surface [171]. Meng and co-workers demonstrated that the electric field gradient has an even larger effect than the electric field confinement by the tip in terms of the sub-nanometer spatial resolution observed in ref [150] by theoretical calculations[172]. Figure 2.7 shows the schematics of electric field and electric field gradient intensity distribution in the plane between the tip and substrate in a TERS configuration. In another paper, Duan et al.[173] studied how the electric field gradient on the length scale of a molecule affects the interaction between the molecule and a localized plasmonic field by quantum mechanical calculations. Their results also had a good agreement with the experimental data in ref [150].

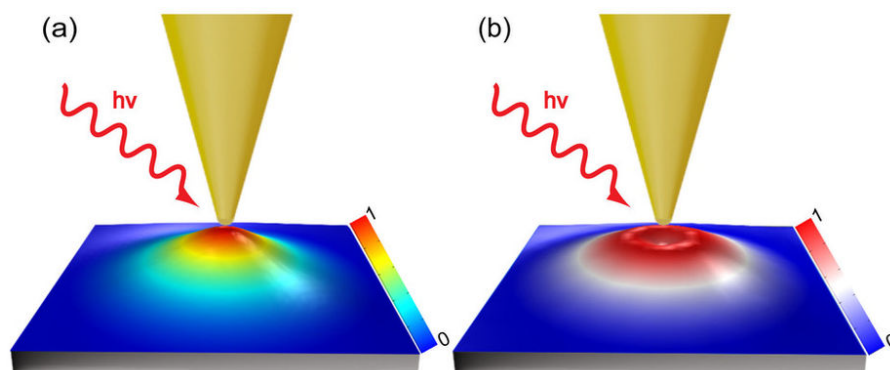


Figure 2.7: The electric field (a) and electric field gradient (b) intensity distribution in the plane between the tip and substrate in a TERS configuration. The maximum of the electric field enhancement locates at the center directly below the tip. In contrast, the maximum of the electric field gradient forms a ring shape below the tip. Figure is adapted from ref [172].

Self interaction

In two recent publications[174, 175], Zhang et al. concluded that if the gap size is comparable with the molecule size, the inelastic scattering of the molecule is so strong that the Stokes-scattered field also influences the optical response of the molecule. This so-called self-interaction process can strongly modulate the signal intensity and spatial sensitivity of Raman response. Based on this, the authors stated the sub-nanometer resolution in TERS could result from the strong optical coupling between the molecule with the plasmonic nanogap.

In general, in the past two years an improved understanding of the mechanisms leading to the substantial signal enhancement is achieved. However, the origin of the sub-nanometer spatial resolution is still under discussion, and the potential influence of quantum and atomistic effects (See section 2.2.3) and the recently proposed theoretical models for signal enhancement are not clear yet.

Chapter 3

Experimental Approach

3.1 Sample Preparation

Three types of SWCNT samples with different nanotube synthesis routes and wrapping polymer/surfactants are used in our work. In this section we will describe their preparation procedures individually.

COMOCAT (6,5) SWCNTs sorted by PFO-BPy

The polymer/SWCNT solution was provided by Imge Namal in the group of Prof. Dr. Tobias Hertel (Julius-Maximilians-Universität Würzburg). It was prepared by mixing 10 mg CoMoCat SWCNTs soot (99.9%, Sigma-Aldrich) and 20 mg PFO-BPy (American Dye Source) in 20 ml of toluene. The mixture was ultra-sonicated by a horn sonicator for 10 h at 0°C. Subsequently, the dispersion was centrifuged at 4000 rpm for 30 min, the supernatant was then selected and re-dispersed in chlorobenzene through 20 min ultra-sonication and 1 h cup sonication.

The deposition of SWCNTs on glass coverslip was done in our chemistry lab via spin-coating. The received solution was diluted 10 times and then mildly sonicated in a water bath sonicator for 5 min. 20 μl of the diluted solution was dropped on a glass coverslip (Marienfeld, refractive index $n \sim 1.52$). The glass coverslip was put still for 20s for the SWCNTs to sink down on the surface. Then spin-coating was taken place at 3000 rpm for 30s. Afterwards the glass was kept rotating, and roughly 2 ml of acetone, toluene and isopropanol was respectively dropped onto it to remove the excess polymer[103].

CVD (6,5) SWCNTs sorted by PFO-BPy

The polymer/SWCNT solution together with drop-casted samples was provided by Kerstin Müller and Matthias Kastner in the group of Prof. Dr. Tobias Hertel (Julius-Maximilians-Universität Würzburg). The SWNT soot was prepared via CVD at 725°C, 12 mbar and the catalyst was FeCo and zeolite. Then 30 mg as-prepared CVD SWCNTs soot and 30 mg PFO-BPy (American Dye Source) were dispersed in 7.5 ml of toluene (Fisher Chemical, quality pa). The mixture was then shear-mixed for 3 h at room tempe-

perature. Afterwards the solution was bench-top-centrifuged at 14000 rpm for 4 min and the supernatant was selected.

The drop-casted sample was made from the following steps. Firstly 10 l of the as-prepared suspension was dropped in the middle of the cover glass (Menzel, type 0). The glass was put still for 30 seconds for a better adsorption of the tubes on the glass surface. Subsequently the second cover glass was put on top of it to uniformly spread the solution onto the glass surface. Some grease was placed at the edges to fix the two glasses together.

COMOCAT (6,5) SWCNTs wrapped with single-stranded DNA

DNA-wrapped SWCNT solution was provided by the group of Prof. Mark C. Hersam (Northwestern University, Illinois). The CoMoCat SWCNT raw soots were dissolved in water and density gradient ultracentrifugation (DGU) sorted the nanotubes by diameter. The SWCNTs were dialyzed and re-dispersed in water using single-stranded DNA ($[GT]_{10}$) as surfactant.

3.2 Experimental Setup

3.2.1 Confocal Microscope

Confocal Microscope setup forms the basis of TENOM. A sketch is shown in Figure 3.1.

For all the work in this thesis, a helium-neon laser (Thorlabs, 17 mW) with emission wavelength at 632.8 nm was used. The laser firstly goes through a laser line filter (LF) to clean out the other wavelengths. Then a pair of lenses with different focal length preliminarily expands the beam diameter. An optional mode convertor is placed after the lenses to turn the linearly polarized beam into radial polarization. (A radially polarized beam is preferred in near-field measurements because it contains more longitudinal components after focusing. We will discuss this further in the next section.) Afterwards, a second pair of lenses expands the beam further to a diameter of 10 mm, so that it fully fills the back aperture of the objective lens to take advantage of its high NA. A pinhole (PH) is put at the focus point between two lenses for spatial filtering.

Subsequently the laser goes into the microscope. We have an inverted optical microscope (Nikon Eclipse TE2000) modified to sample scanning mode. The sample holder is fixed on a piezo scan stage (PI, P-517.3) offering a scan range of $100 \mu\text{m} \times 100 \mu\text{m} \times 20 \mu\text{m}$ with 1 nm resolution in three directions. An SPM controller (RHK Technologies, SPM 1000) administers image acquisition. Inside the microscope, a non-polarizing beam splitter (Melles Griot, 50% transmission, 50% reflection) reflects the laser towards the objective lens. The objective lens (Nikon, CFI Apo TIRF 60X NA 1.49, oil immersion, infinity corrected) focuses the laser on the sample plane. The NA value is as large as 1.49, meaning that the focus is very tight and working distance is pretty small (0.12 mm). The optical response together with reflected and scattered laser light is collected by the same objective lens, then passes the beam splitter and exits the microscope at the side port.

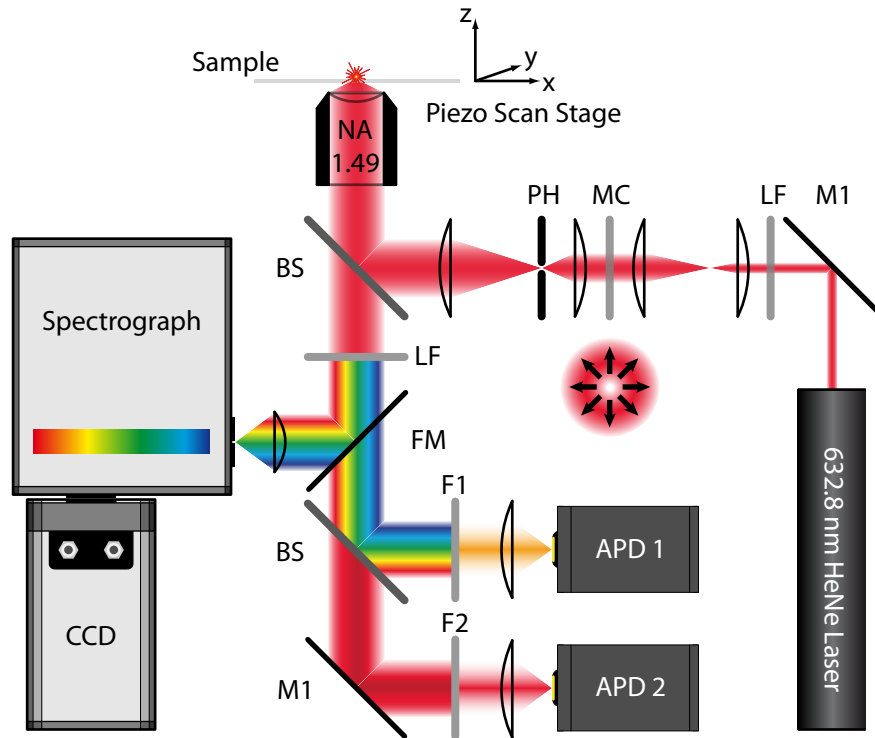


Figure 3.1: A sketch of the confocal microscope setup. The laser is first spectrally cleaned by a laser line filter (LF), then expanded by two pairs of lenses such that the beam fills the back aperture of the objective lens. A mode converter (MC) is placed between two pairs of lenses if a radially polarized beam is needed. In this case a pinhole (PH) is also used to filter out higher-order modes. After entering the microscope, the laser is reflected by a beam splitter (BS) and then focused on the sample by an NA=1.49 objective lens. The optical response is collected by the same objective lens, transmits the beam splitter and leaves the microscope. The first element in the detection path is a 633 nm long pass filter (LF) which removes excess laser light. Afterwards a flippable mirror (FM) determines if the signal goes to two APDs or the spectrometer. On the path to the APDs, the light first passes a dichroic mirror so that the visible part and near-infrared part are separated and detected by two APDs individually. Usually filters (F1, F2) are put in front of the APDs to select a particular spectral window.

Reflected or scattered laser takes up the most part of the light exiting the microscope. Therefore in the detection path a step 633 nm longpass filter (Semrock) is firstly employed to remove the laser signal. Then a flippable mirror (FM) directs the signal either to two identical avalanche photodiodes (APD, Perkin Elmer, SPCM-AQR series) for Raman or PL imaging, or to the spectrometer (Andor shamrock 303i) and a charged-couple-device camera (CCD, Andor iDus) for spectroscopic analysis. If the flippable mirror is down, the light hits a dichroic mirror with cut-off wavelength at 800 nm which separates the visible and near-infrared parts. Then the light is focused by the lenses onto the APDs. Band pass

or long pass filters are put in the path to select a particular spectral window. Usually the first APD detects Raman bands and the second detects PL signals.

The detection efficiency of both APDs and spectrometer significantly decrease towards near-infrared wavelength. The upper detection limit of wavelength is 1000 nm. Particularly, if one measures a broad spectral range, the wavelength dependence of the transmission of various optical elements (objective lens, beam splitter, gratings in spectrometer, etc) must be considered. The solution is to measure the spectra of a calibration lamp with known radiation energy-wavelength relationship. By comparing the measured intensity with real emission intensity at each wavelength, a correction curve could be obtained.

3.2.2 Tip-enhanced near-field Optical Microscope

Our TENOM setup is based on the confocal microscope described above while several additional features have been added to enable tip scanning in the vicinity of sample surface. These features include laser mode conversion, a scanning head together with its tip-sample distance control system. They will be introduced in this section.

Mode Conversion

It is known that the electric field of the incident laser should be polarized along the tip axis (referred to as z axis in the following) to optimize the tip-enhanced near-fields due to lightning-rod effect[176]. A linearly polarized beam only provides very weak z components after being focused, so we exploit a higher laser mode, namely the radially polarized mode.

The mode conversion is achieved by a mode convertor which consists of 4 quadrants of $\lambda/2$ waveplates. As shown in Figure 3.2 (a), these 4 waveplates are placed in the way that the incident electric field is rotated into radial directions. Note that if θ is the angle between the optical axis of waveplate and electric field polarization direction of the incident beam, its orientation is rotated by 2θ . More details could be found in ref [177]. Subsequent spatial filtering with a pinhole removes higher-order laser modes and results in a clear radially polarized beam.

When the radially polarized laser is focused by a high NA objective lens, the z-components of the opposing polarizations interfere constructively resulting in a strong z component. Figure 3.2 (b) displays that the longitudinal field intensity E_z^2 is very strong in the center while the transverse components E_r^2 has a hole there. In the lab when we put a piece of paper perpendicular to the laser propagation direction, the E_r^2 pattern can be observed. That's why the radially polarized beam is also called "donut mode". The transverse in-plane components E_x^2 and E_y^2 exhibit typical double lobe patterns. With the laser wavelength at 632.8 nm, the distance between these two lobes is about 300 nm. This number determines the optical resolution of confocal microscopy with this particular mode.

Scan Head

The scan head is the key part of TENOM setup. During the measurement it stays above the sample with three feet individually standing on the holders fixed to the microscope.

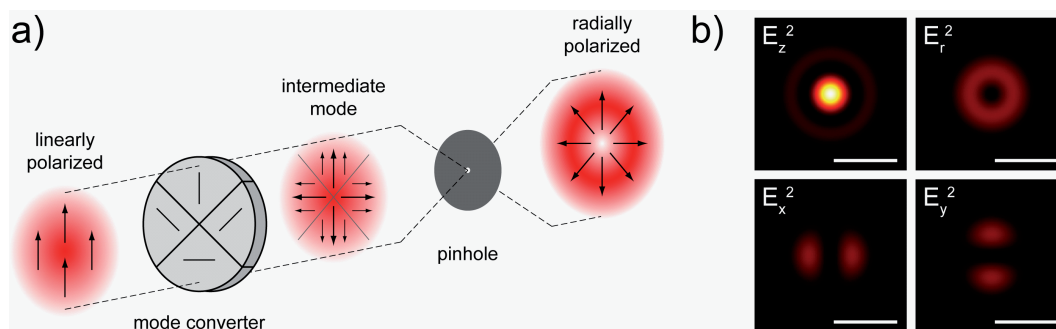


Figure 3.2: (a) Mode conversion from a linearly polarized beam to a radially polarized beam using a composite waveplate. An intermediate mode is formed after the beam passes the mode converter, consisting of four regions with linear polarizations along $\pm x$ and $\pm y$. Undesired higher-order modes are cleaned out by a pinhole. (b) Field distributions after focusing the radially polarized laser with an NA 1.49 objective lens. The peak of the z component E_z^2 is 5 times stronger than that of the radial component E_r^2 . The scale bar is 500nm.

In the center of the scan head is a perpendicularly aligned piezo tube containing x, y, z piezos. The piezo voltages are controlled by the RHK to adjust the tip position. A circuit board, with the tuning fork and other electronic elements, is mechanically attached to the lower end of the piezo tube. The dither piezo sit soldered close to the upper end of the piezo tube is the dither piezo soldered. A periodic voltage signal is applied to the dither piezo by an external device (easyPLL, Nanosurf) and to mechanically excite the tuning fork oscillation. Other elements on the circuit board filters out the noise and are used for a first amplification of the electrical tuning fork signal, which will be described in the next part. The tip is carefully cut to a length of 2 mm and rigidly glued to one leg of the tuning fork following an optimized procedure. In the measurement the tip always vibrates together with the tuning fork.

Tip-sample distance control by shear-force feedback

In all kinds of scanning near-field optical microscope (SNOM), the tip-sample distance needs to be kept very small (a few nm). This means the feedback system must be highly sensitive relying on short-ranged interactions between tip and sample surface. In STM-based systems, the tunneling current is exploited to determine the distance[178, 179]. This only applies to conductive samples. On the other hand, it has been found that if a probe vibrates parallel to the sample surface, the vibration will be influenced by the proximity of the sample. The force between probe and surface is called shear-force and its origin could be a thin water layer on the sample surface and electromagnetic friction[122, 180, 181]. In our TENOM setup, the distance-dependent shear-force is employed as feedback signal to maintain a constant tip-sample interaction.

The magnitude of the shear-force is estimated to be tens of pN [122] and it is thus chal-

lenging to measure it accurately. Nowadays the most commonly used method for shear-force detection is using quartz tuning forks that were originally installed in quartz watches for time standards[182]. A tuning fork has two prongs with electrodes deposited on them. The mechanical oscillation of the two prongs generate time-varying surface charges, producing a current that is subsequently measured by an external electronic circuit. Vice versa, an AC voltage applied to a tuning fork also results in the vibration of two prongs. Therefore the tuning fork is a convertor between mechanical and electrical signals. A bare tuning fork's oscillation frequency is 2^{15} Hz = 32768 Hz. With a gold tip glued, the frequency of tip/tuning fork system reduces to 30-31 kHz due to the increased mass.

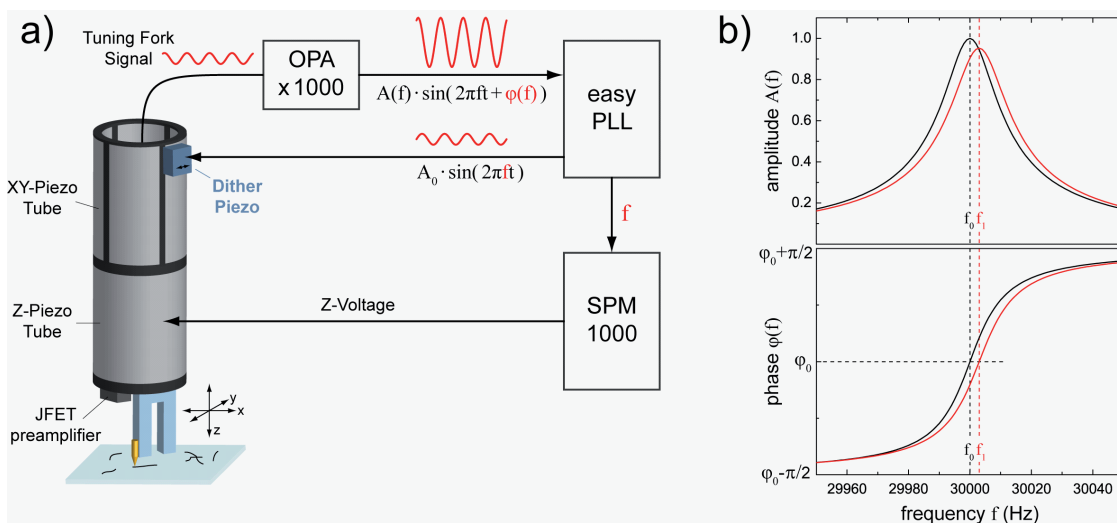


Figure 3.3: Schematic of the shear-force feedback system for tip-sample distance control. (a) The PLL drives the tuning fork to oscillate through a dither piezo. The output voltage from the tuning fork is amplified in two stages and then sent to the PLL detector. The PLL controller changes the driving frequency to keep the phase constant at ϕ_0 . In this way the tuning fork/tip is always driven at its actual resonance frequency. The SPM controller compares this resonance frequency f and accordingly changes the z-piezo voltage to keep a constant frequency shift. (b) The amplitude and phase of the tuning fork vibration against driving frequency in free space (black) and with shear-force applied (red). The existence of shear-force moderately shifts the resonance frequency to the right and leads to a reduced amplitude. However the phase at resonance in both cases is the same ϕ_0 . This enables the employment of the phase-locked-loop technique.

In our experiment, we detect the vibration frequency shift as a measure for the shear-force itself. The schematic of the feedback system is shown in Figure 3.3. The amplitude and phase of the tuning fork oscillation without external perturbation is the black curve in Figure 3.3 (b), its resonance frequency is f_0 and the phase at f_0 is ϕ_0 . When the tip approaches the surface, due to shear-force, the resonance frequency will slightly increase

from f_0 to f_1 and the amplitude will drop a bit. However the phase only shifts in frequency, and the resonance f_1 still corresponds with ϕ_0 . This enables the phase-locked-loop (PLL) technique illustrated in Figure 3.3 (a). The PLL system (easyPLL, Nanosurf) drives the tuning fork at a variable frequency f through the dither piezo. When the tip is far from the sample, f is the resonance frequency f_0 . The output voltage from tuning fork is firstly amplified by a junction field-effect transistor (JFET) and then an operational amplifier (OPA, voltage $\times 1000$) placed in a metal box on the scanning head. The signal is finally handed to PLL. PLL measures the phase with respect to the driving and resets its value back to ϕ_0 by changing the driving frequency f . During the measurement, f is always the actual resonance frequency. f is then given to the SPM controller. The SPM controller varies the z piezo voltage to move the tip up or down such that the frequency shift ($f_1 - f_0$) matches the preset value. In this way the probe-sample distance is kept constant. The z -piezo voltage is recorded and multiplied by the calibration factor to obtain topography data.

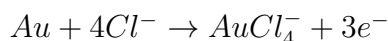
Tip centering

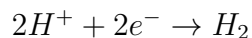
Besides the z position, x and y position of the tip also need to be adjusted so that the tip is centered in the laser focus. This process is named tip centering. In TENOM measurements, we use the gold tip's photoluminescence to align the tip position. Firstly we retract the tip, look through the eyepiece and move the screws of scanning head holder until the shadow of the tip is located in the center of laser pattern. Then we increase the laser power and land the tip. One could see that APD count rate increases as the tip gets closer to the sample surface. After the tip is landed, we manually tune the x,y piezo voltage on RHK. It must be very slow to prevent tip crashing. By changing the voltage, we let the tip move in x - y plane. When the tip comes into the center of laser focus, gold PL is the strongest and we can locate this position by finding the largest APD count rate.

As soon as the tip is successfully centered, the probe scanning can be started. We normally scan over an area of $1\mu\text{m} \times 1\mu\text{m}$ with 128 pixels in each column and row. The pixel size is around 8nm. To avoid tip damage, the scanning speed is set quite low less than $0.5\mu\text{m/s}$ and the tip stays at each pixel for more than 10 ms.

3.2.3 Gold tip fabrication

The sharp gold tips we used in TENOM measurements are prepared via electrochemical etching. A sketch is shown in Figure 3.4 (a). The gold wire (diameter 0.25 mm, Chempur, 99.995%) was dipped into a solution of hydrochloric acid (fuming 37%, Sigma-Aldrich) filled in a quartz cuvette. A platinum ring was made from twisted platinum wire (diameter 0.1 mm, Chempur, 99.995%) and used as counter electrode around the gold wire. A function generator (BK Precision, 4003A) applied square pulses with a duration of 30 μs , repetition rate 3 kHz and an amplitude of 8V between the two electrodes. The main reactions are:





The gold wire loses electrons and gets oxidized, while the H^+ receives electron and turns into hydrogen.

The etching process was observed with an optical microscope in front of the cuvette. The magnification of the microscope is about 80 times. A manual on/off switch was introduced between function generator and gold wire, and one can stop the reaction when the wire diameter reaches the desired size. The microscope is not able to resolve structures below several μm , thus finding the right moment of stopping the etching depends on the user's experience and needs some training. After that, we take the gold wire out and cut off the end with a length of 10 mm. Then the tips are rinsed in DI water and put in a cylinder tip holder.

The final step is to check the diameter and morphology of the gold tips under SEM. Only the tips with symmetric shape and diameter below 30 nm will be used in experiments. Figure 3.4 (b) is an SEM image of a good tip. The diameter is about 20 nm.

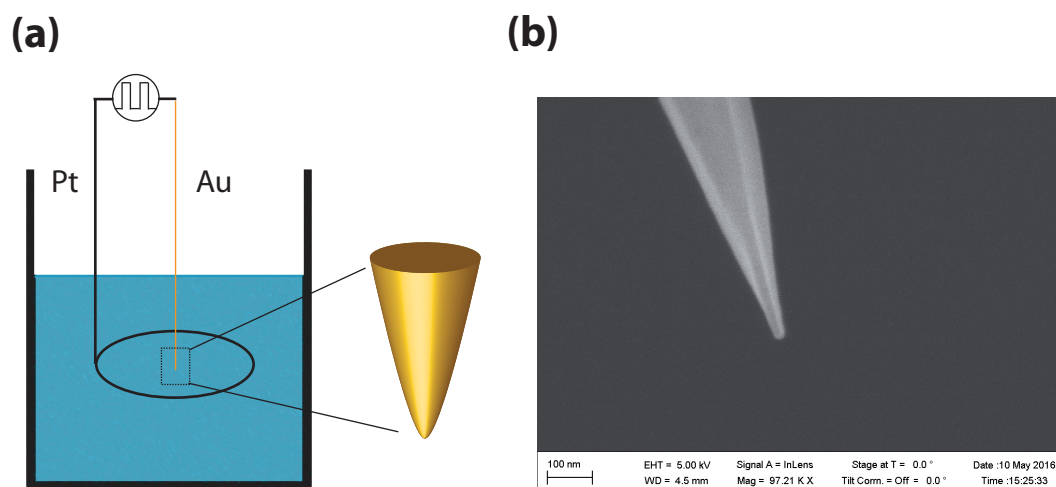


Figure 3.4: (a) A scheme of electrochemical etching setup. Voltage pulses were applied between the gold wire (anode) and platinum rings (cathode) immersed in HCl solution. (b) SEM image of a sharp gold tip with 20 nm diameter.

Chapter 4

Near-field Optical Imaging of (6,5) SWCNT/Polymer Conjugates

As mentioned in Chapter 2, it is very crucial and still challenging to separate single chirality SWCNT for their applications. Various techniques have been invented to realize this goal including chirality-specific polymer wrapping. However, when researchers report their results of nanotube sorting, only macroscopic ensemble methods such as PLE maps, absorption spectra or SEM morphology checks are utilized[100, 183]. In addition, the post-synthesis treatment can alter the properties of SWCNTs as well, but its potential effect has been rarely discussed. Very few papers have experimentally studied polymer/SWCNT interactions and the influence of the wrapping agent on SWCNT's photoactivity at the nanoscale. Our TENOM setup with 10-20 nm spatial resolution and strong signal enhancement offers us the chance to look into these questions on the single nanotube level.

Polyfluorene (PFO)-based extraction of semiconducting SWCNTs has attracted much interest because of its simplicity and high purity[184]. Among PFO derivatives, PFO-BPy was shown to selectively wrap and disperse (6,5) SWCNTs[102]. Aside from polymers, A large variety of amphiphilic surfactants were also used to disperse SWCNTs, such as sodium cholate (SC), sodium deoxycholate (DOC) and single-stranded (ss) or double-stranded (ds) DNA. In our measurements three SWCNT samples are selected: commercially available CoMoCAT (6,5) SWCNTs (referred to as CoMoCAT SWCNTs in the following) sorted by PFO-BPy, CVD-synthesized, without purification (6,5) SWCNTs (referred to as CVD SWCNTs in the following) sorted by PFO-BPy and CoMoCAT (6,5) SWCNTs wrapped with single-stranded DNA. The CoMoCAT nanotubes are treated with acids or oxygen to remove catalyst particles, amorphous carbon etc. This treatment can shorten the tubes and lead to a higher defect density. The CVD tubes are used directly after synthesis without any treatment. The two PFO-BPy wrapped samples represent selective polymer extraction (SPE) method (See section 1.2) which is the most common approach to sort SWCNTs nowadays. The DNA-wrapped nanotubes represent aqueous two-phase extraction (ATPE) technique acting as a control group.

Photoluminescence, as the radiative decay of excitons, is very sensitive to extrinsic

effects arising from the wrapping polymer or adsorbed species (See section 1.3). In the first section of this chapter, we will present typical near-field images of all the three samples. Inhomogeneous PL intensity along the nanotubes is commonly observed. In the second section, we will construct a statistical model to evaluate the PL intensity fluctuations and further assess the influence of different wrapping polymers and SWCNT treatment. A main factor causing the fluctuation are defects. In the third section we will generate photo-induced defects on nanotubes and investigate how they influence SWCNT PL.

4.1 Observation of Near-field PL intensity variations along SWCNTs

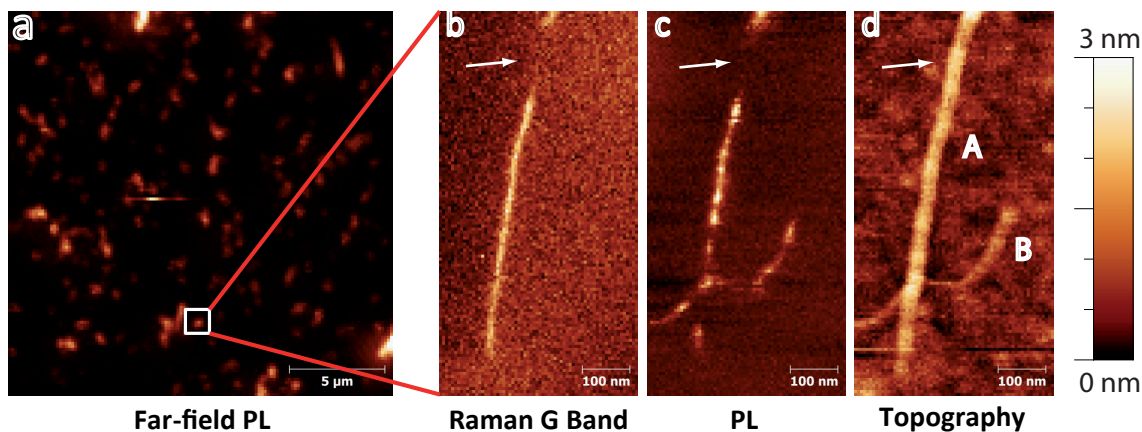


Figure 4.1: Confocal and near-field images of PFO-BPy sorted CoMoCAT (6,5) SWCNTs. a) Confocal PL images indicate the positions of nanotubes. A 950 nm longpass filter was used in the detection path, so most bright spots result from (6,5) nanotubes. The white rectangle marks the position of the subsequent near-field scan. b) - d) Simultaneous near-field Raman, PL and topography images. The λ_{22} of (6,5) SWCNTs is too far from our excitation wavelength to satisfy resonant Raman scattering condition, therefore Raman intensities of (6,5) nanotubes should be very weak. That's why structure B is not visible in (b). The strong near-field Raman signal of structure A probably comes from (7,5) SWCNTs with λ_{22} at 644 nm. Since it also shows bright near-field PL signal in (c), structure A is likely to be a thin bundle of (6,5) and (7,5) SWCNTs. Near-field PL intensities along the nanotubes exhibit significant fluctuations.

Confocal PL image and simultaneous near-field Raman, PL and topography images of PFO-BPy sorted CoMoCAT (6,5) SWCNTs are shown in Figure 4.1. On the left is the diffraction-limited far-field PL image ($20 \times 20 \mu m^2$, 128 pixels per line) with roughly 250 nm spatial resolution (See chapter 2). In the experiment a 950 nm long pass filter was used

because the detection efficiency of the Si-APD drops significantly for wavelengths exceeding 1000 nm (See chapter 3), thus most of the bright spots represent the (6,5) nanotubes with $\lambda_{11} = 975$ nm. A high density of the nanotubes is observed, and the majority of the tubes have a length below 2 μm . The areas showing a bright and extended PL signal in the confocal scan were chosen for further TENOM studies. Figure 4.1 (b) - (d) display the near-field images recorded in the white rectangular area in (a). In (b) and (c) clear near-field signals are shown with 20 nm spatial resolution. The Raman G band signal was detected with a bandpass filter 700 ± 5 nm. The topography in (d) is a bit broad with 35 nm spatial resolution, likely due to slightly broadened tip shape.

Very interestingly, the Raman and PL signals don't exactly follow the topographical data. First of all, two nanotube-like structures (labeled as A, B) are seen in PL and topography while B totally disappears in the Raman image. The reason is that the wavelength corresponding to the energy of the second excited state (λ_{22}) of (6,5) SWCNTs is 567 nm which is quite far from our excitation wavelength 632.8 nm. Therefore it's difficult to achieve resonant Raman scattering condition in the experiment and the Raman intensity for (6,5) nanotube is expected to be very weak. The strong near-field Raman signal of structure A probably comes from (7,5) SWCNTs with λ_{22} at 644 nm. Given that structure A also exhibits a substantial near-field PL signal, it is very likely to be a thin bundle consisting of (6,5) and (7,5) SWCNTs. Its topographic height of around 3 nm also matches the height of a few stacked nanotubes plus the surrounding PFO-BPy layer, which supports our speculation.

In addition, in the upper part of the images, a 100 nm long segment of A (labeled by the white arrow) is totally dark in both Raman and PL images. The first guess would be that this part is deeply covered with surfactants or impurities so that the tip is too far from the nanotube for signal enhancement. However, this cannot be true because the height along structure A is constant. One possibility is that this part only includes (6,5) SWCNTs and that the PL is quenched by intrinsic defects[63, 10] or chemisorbed species[77].

The near-field Raman intensity and topographic height along the nanotubes are quite stable with little variations. On the contrary, the near-field PL intensities along both A and B are fluctuating a lot with alternating bright and dark segments. The shortest segment length is 30 nm. This confirms that the PL is more sensitive to environment and contains more information. The variation of PL will be further discussed in the next section.

Confocal PL image and simultaneous near-field Raman, PL and topography images of PFO-BPy sorted CVD (6,5) SWCNTs are shown in Figure 4.2. The same filters (950 nm long pass for PL, 700 ± 5 nm for Raman G band) were used. The CVD sample has a much lower SWCNTs density on the glass slide, in the sense that only a few nanotubes can be observed in the confocal image within $20 \times 20 \mu\text{m}^2$. Compared with CoMoCAT SWCNTs, these SWCNTs are generally much longer with lengths exceeding 2 μm . They also emit stronger PL probably because they are free from acid or oxygen treatment. In the far-field image there are some nanotube structures exhibiting very bright PL, such as the one in the lower part of Figure 4.2 (a). They are very likely large nanotube bundles and are avoided

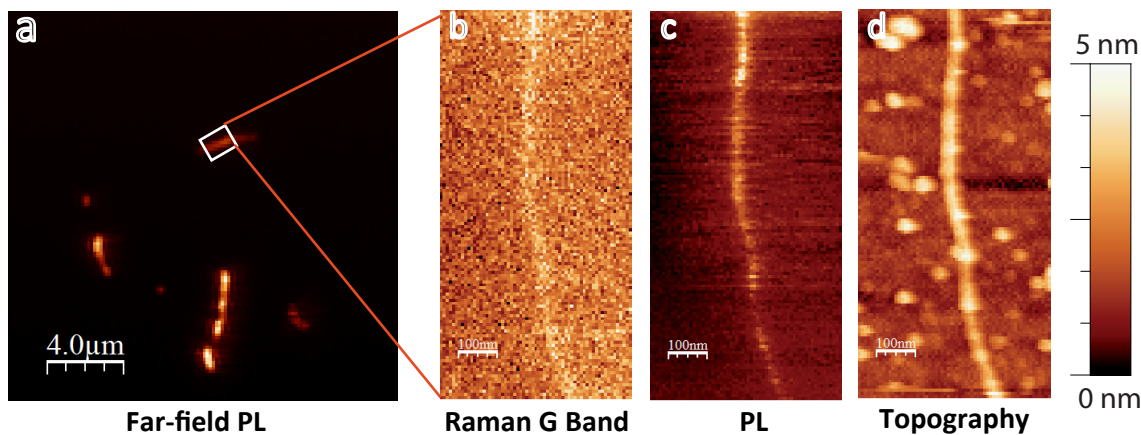


Figure 4.2: Confocal and near-field images of PFO-BPy sorted CVD (6,5) SWCNTs. The used filters are the same as in Figure 4.1. a) Only a few SWCNTs are found in the confocal PL image, which indicates a lower nanotube density. The typical length of CVD nanotubes is a few microns. The extremely bright signals come from nanotube bundles. b) - d) Simultaneous near-field Raman, PL and topography images. One nanotube could be seen in all three images. It exhibits weak near-field Raman intensity but strong near-field PL. The PL intensity along the nanotube fluctuates, but to a smaller extent than in Figure 4.1 (c). Moreover, in some cases the intensity fluctuations affect the whole horizontal scan direction indicating that they are due to blinking of the nanotube rather than spatial variations. In (d) many smaller features with a few nms height exist both on glass substrate and on the nanotube.

in the subsequent near-field tip scans.

Figure 4.2 (b)-(d) show the corresponding near-field Raman, PL and topography images of a single extended PL signal in (a). From the width of the optical signals, the spatial resolution is seen to be about 20 nm. Both the near-field Raman and PL intensity follow the nanotube seen topographically. As we said before, the Raman intensity is quite weak. The near-field PL is sharp, and intensity variations along the nanotube are observed, although the fluctuations are not as strong as in Figure 4.1. In the topography image, besides the nanotube, many particles with 30-50 nm size and a few nms height are seen. They could be excess polymer from the solution or some catalyst residuals from the CVD synthesis. It could be observed that some of these features are attached to or stacked on the nanotube, resulting in a topographical height as much as 5 nm. The part with a larger height doesn't correlate with a lower PL intensity, therefore we know the PL variation doesn't origin from the possible change in tip-sample distance.

A typical set of confocal PL and simultaneous near-field Raman, PL and topography images of DNA wrapped CoMoCAT CVD (6,5) SWCNTs are shown in Figure 4.3. A dense coverage of nanotubes on glass is observed in (a). They have a similar length as the ones in Figure 4.1. A nanotube is seen in the topography image with a height of 2.5 nm. Since no

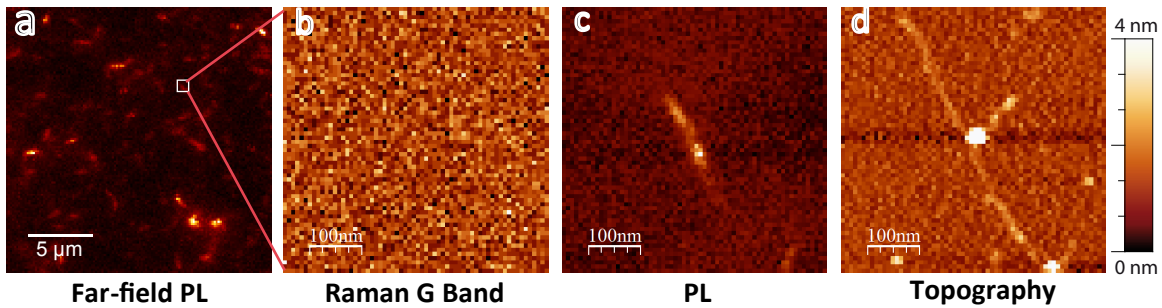


Figure 4.3: Confocal and near-field images of DNA wrapped CoMoCAT (6,5) SWCNTs. The used optical filters are the same as in Figure 4.1. a) Confocal image which is seen to be similar to the one in Figure 4.1. A dense coverage of nanotubes with length around $1 \mu\text{m}$ is observed. b) - d) Simultaneous near-field Raman, PL and topography images. One nanotube is seen in the topography image, but no near-field Raman signal is detected and only a small part in the center emits near-field PL.

near-field Raman signal was detected, its chirality is likely to be a (6,5). However, different from the other two samples, most parts of the nanotube are dark in the near-field PL image except a 250 nm long segment in the center. Within this bright segment, the PL intensity also varies. We note that this is not an extreme example but typical for DNA-wrapped SWCNTs: they mostly exhibit strong intensity fluctuations with a few hundred nms long sections being totally dark. It should be noted that most raw data on DNA-wrapped nanotubes were recorded by a former group member Carsten Georgi and is used here for comparison. The data analysis is done by the writer.

4.2 Statistical analysis of near-field PL heterogeneity of different SWCNT samples

In the last section we noticed that the near-field PL intensities along the nanotube are nearly always heterogeneous regardless of the sample type. Generally, the intensity variations can be further divided into two categories:

- PL quenching, i.e. a particular part of the nanotube doesn't emit any near-field PL in the detection window. This usually results from defects, nanotube ends or local charges, where the original energy band configuration is perturbed and a non-radiative decay path (often related to an intermediate energy state) dominates the exciton relaxation[61, 185, 58, 186].
- rapid PL fluctuations, i.e. the near-field PL intensity varies without being completely quenched due to exciton localization. Exciton localization refers to the fact that exciton energy variations along the nanotube promotes exciton diffusion towards local

energy minima[11, 187]. These local energy minima are called localization sites and they exhibit a locally enhanced PL intensity owing to an increased exciton density. An illustration is shown in Figure 4.4. In general, the exciton energy variations could be induced by intrinsic defects, side-wall functionalization[188, 189], inhomogeneous polymer wrapping[11, 75], physis/chemisorbed species[77, 190], local temperature[191] and strain[192, 193] difference.

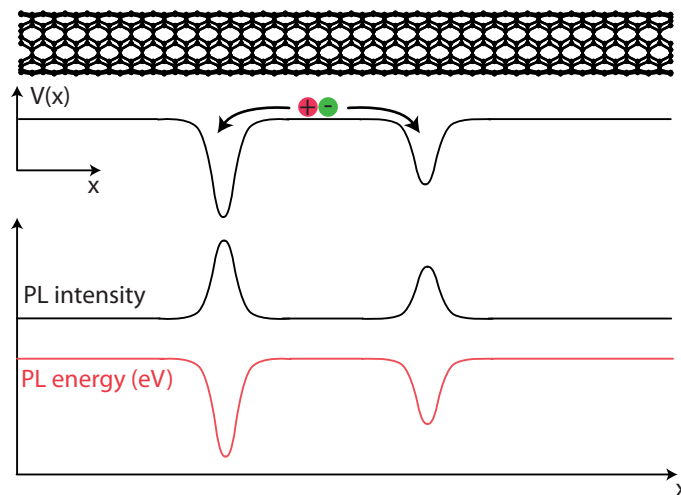


Figure 4.4: A qualitative illustration of exciton localization in SWCNTs. Exciton energy along the nanotube is not constant but fluctuating. The excitons tend to diffuse toward the local minima due to the energy difference. At these sites, the local PL intensity is higher because of a greater exciton density, but the PL emission energy is lower.

In SWCNT-based solar cell devices, a very important requirement after photon absorption is the successful intra- or inter-nanotube exciton transport to the interface. Both of the aforementioned cases involve a trap state which “captures” the excitons and prevents them from traveling, which will be detrimental to the device performance. Therefore, the near-field PL heterogeneity can be an essential indicator for the photoactivity of SWCNT/polymer conjugates and would therefore be of great interest.

In a given near-field image, by defining a profile along a nanotube, one can extract the PL intensities at each pixel $I_1, I_2 \dots I_n$. To quantify the PL intensity heterogeneity, we introduced a statistical parameter, coefficient of variation C_v defined as:

$$C_v = \frac{\sigma}{\mu} \quad (4.1)$$

Where σ is the standard deviation and μ is the mean value. Here we used C_v instead of standard deviation because the enhancement factor can be different among tips. A tip with stronger field enhancement increases the intensity resulting in a larger standard deviation.

This effect can be cancelled out by dividing the standard deviation by the mean value. For an ideal defect-free SWCNT, the PL intensity is always the same, so $\sigma = 0$ and $C_v = 0$. A larger C_v value means a stronger intensity fluctuation, indicating more exciton traps on the nanotube, hence a lower suitability for SWCNT-based solar cell devices.

In Figure 4.5, the PFO-BPy wrapped CoMoCAT SWCNT in Figure 4.2 was taken as an example to show our PL intensity heterogeneity analysis. The nanotube profile is marked by a green dashed line in (a). The extracted PL intensity was plotted against distance along the nanotube axis in (b). It shows apparent fluctuations even reaching zero. An average PL intensity $\mu = 19.1$ kHz and a standard deviation $\sigma = 15.6$ kHz were found. Thus the C_v of this particular nanotube is $\sigma/\mu = 0.82$.

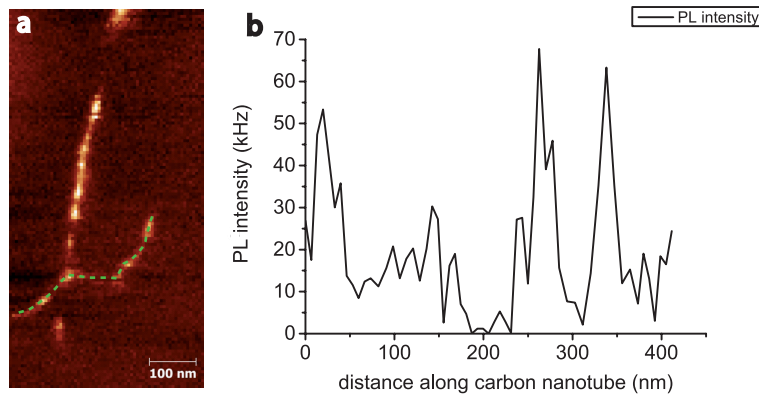


Figure 4.5: Near-field PL intensity heterogeneity analysis on the SWCNT in Figure 4.2. (a) Near-field PL image. A profile is defined along the nanotube and the intensity at each pixel is read out. (b) PL intensity profile along the nanotube axis. Strong fluctuations can be observed.

To ensure the validity of our statistical analysis, we performed measurements and data selection with the following criterion:

- The PL intensity of SWCNTs saturate at high excitation power due to exciton-exciton annihilation[65, 194, 195]. To minimize its influence, in all the TENOM measurements contributing to this work a moderate laser power below $0.2 \text{ mW}/\mu\text{m}^2$ was used.
- The spectra of the SWCNT were checked before or after TENOM measurements. Only the nanotubes with a characteristic (6,5) PL peak were selected for the following statistical analysis. A typical PL peak of (6,5) SWCNT at room temperature is shown in Figure 4.6. The peak center is around 1.27 eV with ~ 30 meV full-width at half-maximum (FWHM). Considering tube-tube variation, we allowed the PL peak center to lie between 1.25 and 1.28 eV (wavelength range $\sim 980\text{-}1000$ nm).
- The nanotube ends also quench PL. Therefore the PL of a short nanotube with a few hundred nms length will be heavily suppressed. There have been several studies on

how the nanotube length affects the quantum yield [57, 58]. To reduce the influence of nanotube ends, we only included nanotubes longer than 500 nm in our analysis.

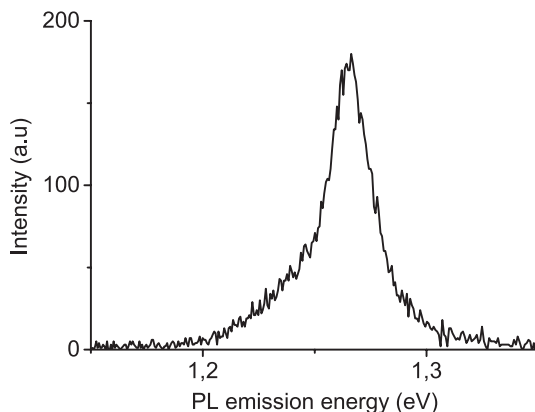


Figure 4.6: A typical PL peak of (6,5) SWCNT at room temperature. The peak is centered at 1.27 eV with a 30 meV half-maximum full-width.

We collected a large amount of TENOM measurement data, then selected at least 15 individual SWCNTs for each of these three sample types and analyzed their near-field PL heterogeneity. Their C_v values are plotted in a histogram shown in Figure 4.7.

From Figure 4.7 it is clear that PFO-BPy wrapped SWCNTs are more optically homogeneous than the DNA wrapped ones. We attribute this to a more uniform wrapping from PFO-BPy. The mechanism of the selective wrapping of SWCNTs by PFO families is not yet fully understood, but from MD simulations it is assumed that the polymer backbone interacts with nanotube surface through $\pi - \pi$ conjugation, and the side alkyl chains promote debundling and dispersion in organic solvents. With an optimal dihedral angle between nanotube axis and polymer backbone, the interaction is maximized and the steric hinderance from large rigid building blocks maintains the contact, resulting in a helical wrapping around the nanotube[92, 98, 99]. On the other hand, the aromatic nucleic-acid base of DNA also interacts with SWCNT through $\pi - \pi$ stacking, but meanwhile leaves its phosphate backbone highly charged[196, 197, 91]. These local charges could be expected to quench the PL. In addition, DNA-wrapped SWCNTs are dispersed in aqueous solution. After spin-coating there could be some residual water adsorbed on both the surface and the inner side of SWCNTs. The water molecules are known to p-dope the nanotubes and enhance nonradiative exciton decay[77]. Another possible reason is that compared with PFO-BPy, single-stranded DNAs have a smaller molecule size and leaves more surface area of SWCNT uncovered, which contributes to the PL fluctuation.

Between the two PFO-BPy wrapped SWCNTs, we could see that their average C_v values are quite close indicating the uniform wrapping for both materials. In the case of CoMoCAT SWCNTs, there are two nanotubes observed with quite large C_v values. As

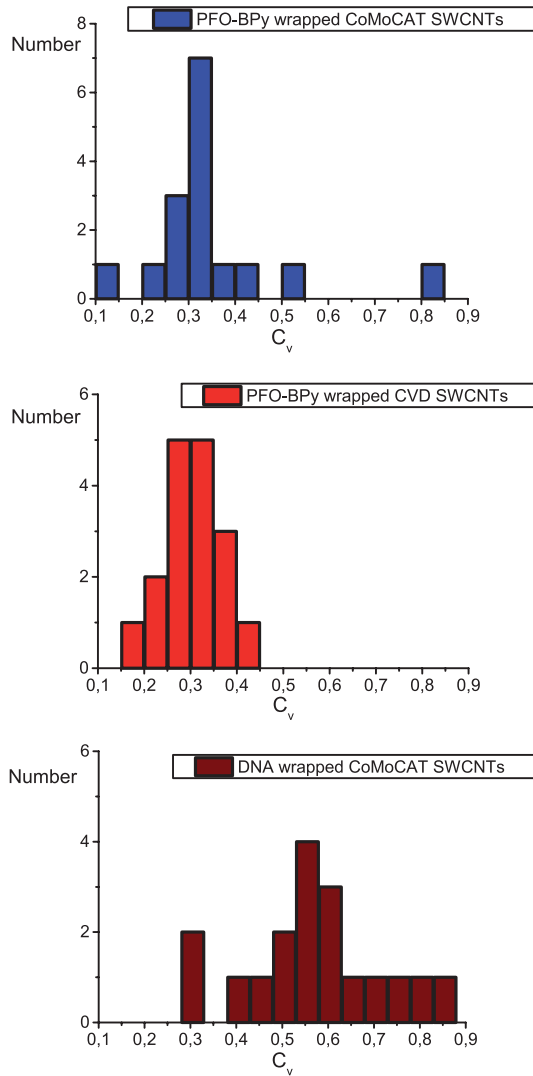


Figure 4.7: The C_v values of individual nanotubes from different samples. From up to down are the C_v distributions of PFO-BPy wrapped CoMoCAT SWCNTs, PFO-BPy wrapped CVD SWCNTs and DNA wrapped CoMoCAT SWCNTs. The PFO-BPy wrapped nanotubes have smaller C_v values than DNA-wrapped ones. The two kinds of PFO-BPy nanotubes have very similar C_v values, but the CVD nanotubes have a narrow distribution.

mentioned before, CoMoCAT SWCNTs are treated with acids or oxygen to remove metal catalysts after synthesis, which could induce defects on them. We attribute the extraordinarily heterogeneous PL distribution of these two SWCNTs to a high defect density. In general, the optical homogeneity is not primarily determined by nanotube material specific properties which could result from different post-synthesis treatment.

To sum up, we introduced a new statistical parameter C_v to characterize the optical heterogeneity of near-field PL of different SWCNT samples for the first time. A larger C_v represents a stronger PL intensity fluctuation, indicating the exciton has a larger probability to be trapped during diffusion or quenched by local defect sites, hence the sample is less suitable for solar cell applications. Based on a large number of TENOM measurements on individual nanotubes, we demonstrated that PFO-BPy is a better wrapping agent than DNA because PFO-BPy wrapped SWCNTs exhibit high optical homogeneity, while the DNA-wrapped ones, typically with totally dark segments at a few hundred nms length, have a larger C_v value. Comparing the results from PFO-BPy wrapped CoMoCAT and CVD nanotubes, we found that the intrinsic homogeneity of SWCNTs is not the determining factor for optical homogeneity, which underlines the importance of choosing a suitable wrapping agent.

4.3 Photo-induced defects and their influence on near-field PL

From previous discussions we know that defects quench PL and prevent exciton diffusion. Aside from the inevitable ones resulting from the synthesis process and post-synthesis treatment, they can also be induced under illumination during device operation. For a SWCNT-based solar cell, the generation of defects can be expected to strongly diminish the transport abilities of nanotubes and heavily harm the device performance. In this section, we will generate localized defects on single SWCNTs using the strong optical near-fields under the gold tip and monitor how these defects affect the near-field PL.

Figure 4.8 shows a series of near-field PL images recorded on the same nanotube under constant illumination. In order to induce the defects relatively fast, a strong excitation intensity of approximately $2 \text{ mW}/\mu\text{m}^2$ was used. The images are plotted on the same scale for intensity comparison.

How the SWCNT is bleached step by step is clearly displayed in these images. The first near-field scan reveals a bright and nearly continuous nanotube profile. Similar with the images in section 4.2, the PL intensity along the nanotube is not homogeneous. Two positions exhibit a local maximum labeled as A and B. They are likely due to exciton localization. In the second scan, a few dark segments start to appear, indicating that photo-induced defects are generated and quench the PL within a certain distance around them. Most part of the nanotube emits PL but not as bright as in scan 1. As the experiment proceeds, in the third scan the PL intensity further drops and the nanotube consists of alternating dark and bright segments. The localization effect at position A has disappeared.

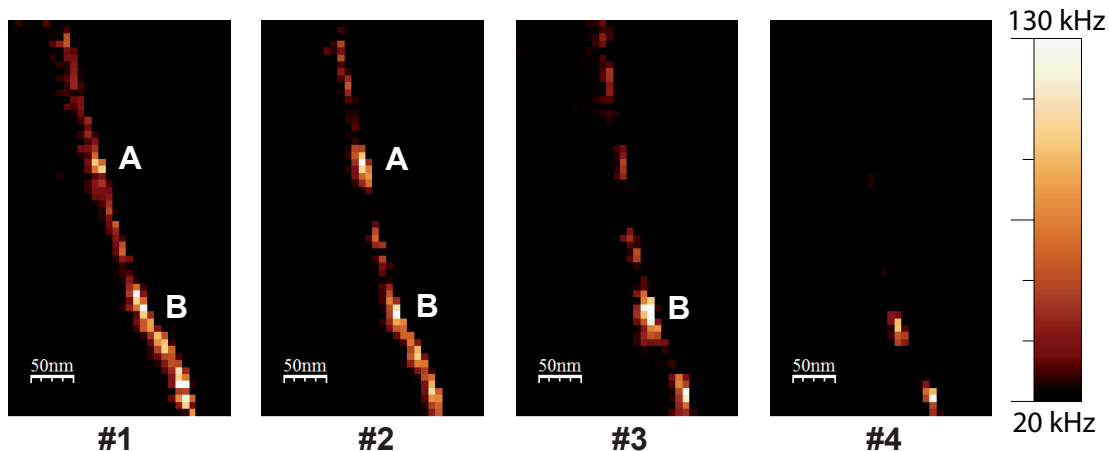


Figure 4.8: Near-field PL images of a PFO-BPy SWNT consecutively recorded at roughly $2 \text{ mW}/\mu\text{m}^2$ excitation intensity. Step-like bleaching is observed within individual segments.

In the fourth scan nearly all the nanotube is “switched off” with only two luminescent spots visible in the image.

From the near-field scan series, we can obtain some information about the exciton diffusion range. When a defect is generated, it will not only trap excitons at this position but all excitons which can reach this defect through diffusion. That’s why in Figure 4.8 the dark segments always have a certain length. In Figure 4.9 the PL intensities along the nanotube in different scans was plotted and compared. For example, nearly all the PL peaks in scan 1 are preserved except the one marked with a green rectangle. This corresponds to a newly appeared quenched segment with about 50 nm length. A similar dark segment length is found from the comparison between scan 2 and scan 3 (right side of Figure 4.9). This measurement was repeated on a few other nanotubes, and the shortest length of quenched segment was always found to be around 50 nm. This is on the same order of magnitude with previous studies on nanotubes deposited on a dielectric substrate[61, 58, 10]. Higher values at a few hundred nms are observed in air-suspended SWCNTs[59, 198]. Due to the finite spatial resolution from the gold tip, the observed length would be the upper limit of the exciton diffusion range.

In section 4.2 we introduced C_v to evaluate the near-field PL heterogeneity. C_v reflects the optical property of a whole nanotube but cannot reveal any information on the length scale of the optical heterogeneity, i.e. cannot distinguish if there’s a regular length of the alternating bright and dark segments. In Fluorescence correlation spectroscopy (FCS), an autocorrelation function is defined to find the temporal fluctuations of the fluorescence intensity[199]:

$$G(\tau) = \frac{\langle \delta I(t) \delta I(t + \tau) \rangle}{\langle I(t) \rangle^2} \quad (4.2)$$

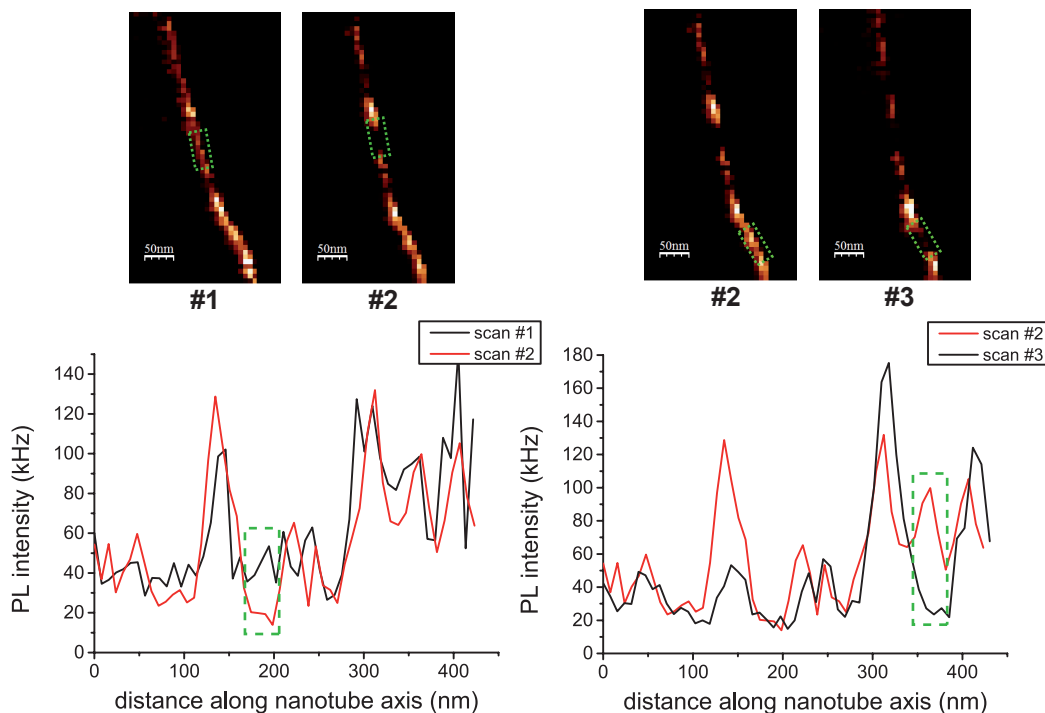


Figure 4.9: The length of PL quenched segments yields information about exciton diffusion range. The quenched parts are highlighted with green rectangles. Left: Near-field PL intensity comparison between scan 1 and 2. Right: Near-field PL intensity comparison between scan 2 and 3. In both cases, a $\sim 50\text{nm}$ quenched segment is observed.

Where $\delta I(t) = I(t) - \langle I(t) \rangle$ is the deviation from the mean intensity. Similarly, we can define an autocorrelation function between intensity I and position x to find the spatial fluctuations of the near-field PL intensity:

$$G(X) = \frac{\langle \delta I(x) \delta I(x + X) \rangle}{\langle I(x) \rangle^2} \quad (4.3)$$

Where $\delta I(x) = I(x) - \langle I(x) \rangle$ is the deviation from mean intensity at one position. In FCS, how fast the autocorrelation function decays with τ indicates the diffusion time for one particle to move out of the detection area or volume. In our analysis, how fast the autocorrelation function decays with X tells us the correlation length from bright to dark.

Applying the function $G(X)$ to the nanotube in Figure 4.8, we obtain the autocorrelation curves shown in Figure 4.10. The corresponding curves of scan 1 and scan 2 are quite alike and decrease very slowly with $\log(X)$. In these two scans most part of the tube is not quenched yet and the PL intensity contains no periodic component so that no correlation length can be resolved. On the contrary, the decay in scan 3 and 4 both is much faster because the defects have separated the nanotube into quenched and bright segments, redu-

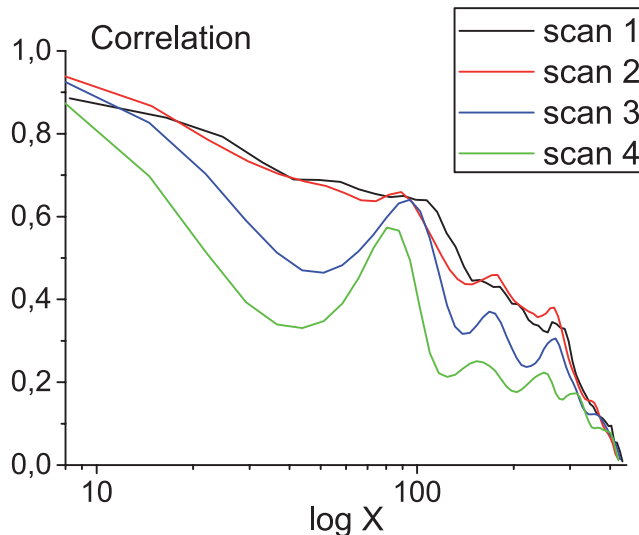


Figure 4.10: Autocorrelation curves of the scan series on the SWCNT in Figure 4.8. From scan 1 to scan 4, the autocorrelation function has a faster decrease with X , because the photo-induced defects quench the PL in individual short segments, bringing more periodicity to the PL intensity profile. Therefore autocorrelation function tends to yield a smaller correlation length.

cing the correlation length of the PL intensity. In addition, from the autocorrelation curves we can see peaks in the autocorrelation functions indicating that intensity fluctuations happen mostly on the scale of 50 - 100 nm.

In conclusion, three different SWCNT samples were investigated: commercially available CoMoCAT (6,5) SWCNTs sorted by PFO-BPy, CVD-synthesized, without treatment (6,5) SWCNTs sorted by PFO-BPy and CoMoCAT (6,5) SWCNTs wrapped with single-stranded DNA. We first conducted TENOM measurements on them and achieved simultaneously near-field Raman, PL and topography images. Although the far-field PL looked homogeneous, their near-field PL showed pronounced intensity fluctuations. To characterize the optical heterogeneity of near-field PL, we introduced a statistical parameter C_v and compared the results from different SWCNT samples. A larger C_v represents stronger PL intensity fluctuations, indicating a large number of exciton traps and/or defects on the nanotube, hence a lower suitability for solar cell applications. Based on a large number of TENOM measurements on individual nanotubes, we demonstrated that PFO-BPy is a better wrapping agent than DNA because PFO-BPy wrapped SWCNTs are optically more homogeneous. The post-synthesis treatment for commercial CoMoCAT nanotubes resulted in extra defects and some CoMoCAT tubes showed high C_v values. However, the effect from the treatment is not as strong as the wrapping polymer. We also generated localized photo-induced defects with high laser excitation power and observed their quenching behavior. Another statistical parameter, the autocorrelation $G(X)$ characterized the

length scale of optical heterogeneity. Our findings confirmed the great application prospect of PFO-BPy for SWCNT sorting and provided useful information on sample synthesis and treatment for the fabrication of all SWCNT based devices. The statistical parameters we used are also applicable to the analysis of near-field data on other nanomaterials.

Chapter 5

Near-field and far-field Separation via Tip-sample distance modulation

Scanning near-field optical microscopy (SNOM) is a technique for nanomaterial investigation featuring high spatial resolution by exploiting the properties of evanescent waves. Commonly used versions of SNOM include (elastic) scattering scanning near-field optical microscopy (s-SNOM) in which elastic scattering of the laser is detected, and tip-enhanced near-field optical microscopy (TENOM) in which Stokes-shifted signals such as Raman and PL are detected. Both types employ a nano-antenna which is mostly based on plasmonic nanostructures such as a noble metal tip.

Nevertheless, SNOM still confronts a few challenges. The most important one is that although the nano-antenna provides an enhanced signal with a high spatial resolution, the far-field background from direct laser illumination on the sample is still present. The existence of far-field signal lowers the signal to background ratio and decreases detection sensitivity. On the other hand, the enhancement ratio is determined by many factors including the particular optical process of the material, the tip dipole orientation and tip surface chemistry, thus it is variable in a wide range[7, 200]. Therefore, if the near-field contribution is not strong in some cases, it could be covered under the far-field background and can't be realized at all. Figure 5.1 shows typical SWCNT confocal and near-field Raman and PL images from our set up. If one takes the intensity profile across a nanotube, it could be observed that the overall signal consists of two parts: widely spread far-field background (black curve) and spatially confined near-field signal (red curve).

To solve this problem, some methods have been developed in the literature to increase near-field/far-field signal ratio. A common approach is based on the signal demodulation at the tip vibration frequency or higher harmonics using lock-in amplifiers[201, 202, 203]. This scheme is based on regular AFM probes operated in tapping mode and can't be directly transferred to shear-force based tuning fork systems. Also the images presented in these works typically don't have a very high signal to background ratio. Another way is to connect the photons with tip oscillation cycle by time-tagged photon counting schemes[204, 205, 206]. However, the setup is usually complicated because it requires storing

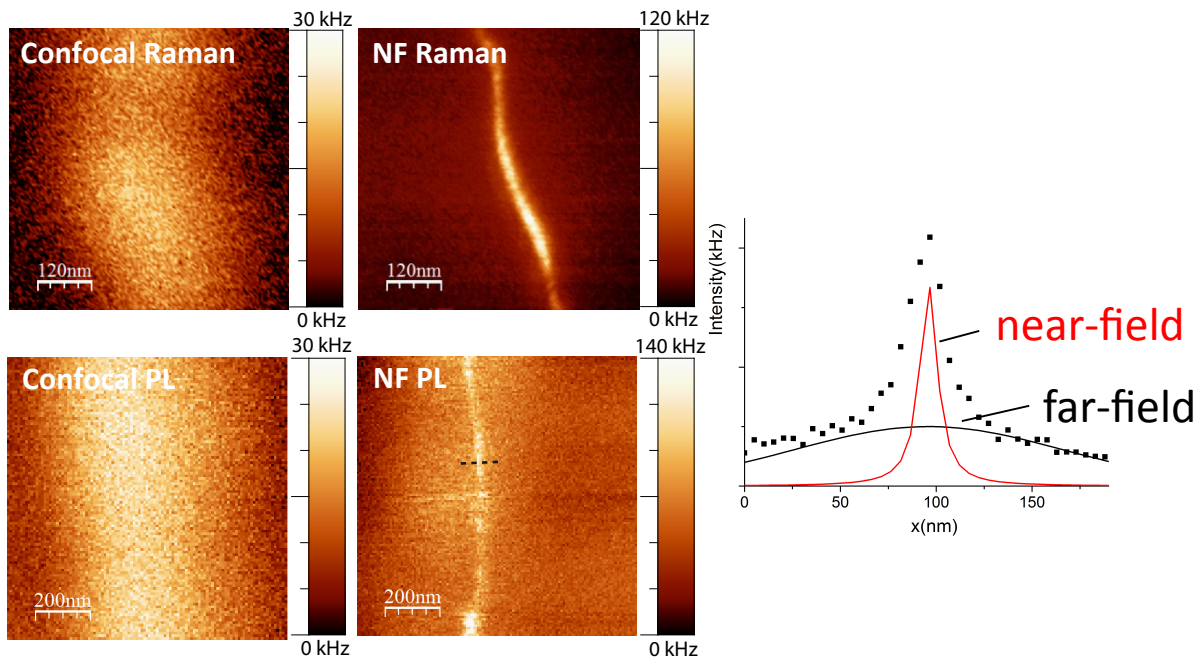


Figure 5.1: Far-field background signal is always present in conventional near-field images. Left: Confocal and Near-field Raman and PL images of SWCNTs. Black dashed lines represent the cross-section perpendicular to a tube. Right: Intensity profile along the white dashed line in near-field PL image. data points are labeled by black dots. The black and red curves represent far-field and near-field contributions respectively.

of all photon arrival times leading to enormous amount of data. A time-gating approach based on a cantilever AFM was presented by the Kawata group[205] in which the photons were detected only within the time intervals of smallest and largest tip-sample distance respectively using two gates. For tuning-fork based systems tip-sample distance modulation was first demonstrated by Hoepfner and co-workers[207]. They added a low-frequency (10 - 100 Hz) set-point modulation to a tuning fork based system and rejected the background signal through signal demodulation at this external frequency. One disadvantage is that the modulation frequency must be low so that the feedback can follow, and this leads to slow scanning rates. In addition, the maximum tip-sample distance is limited into the range in which a force between tip and sample can be detected, at this point some near-field signal still exists but gets eliminated by signal demodulation. In principle, A new scheme with simple configuration, little tip perturbation and suitability to tuning fork-based systems is still in demand.

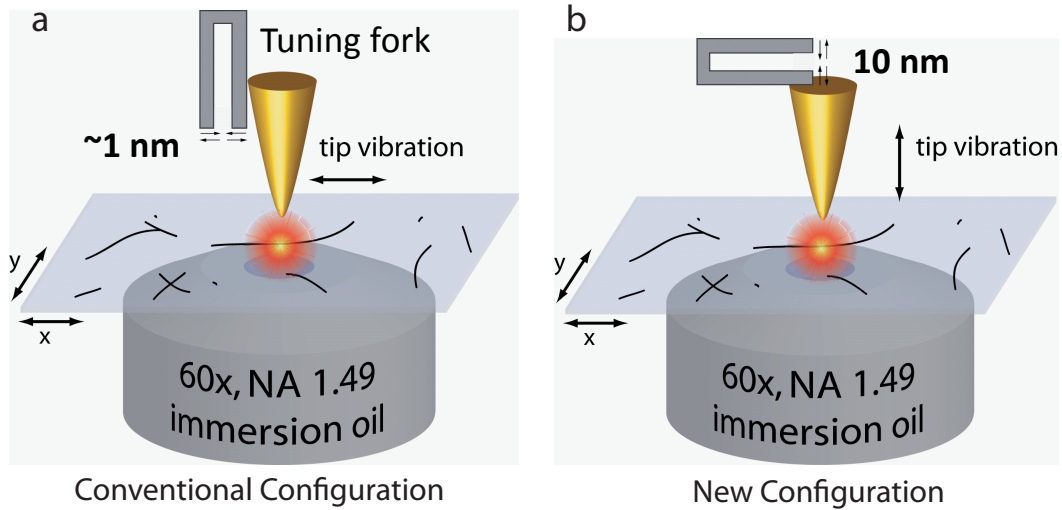


Figure 5.2: The schemes of conventional and new tuning fork-tip configurations. (a) Conventional configuration. The tuning fork oscillation amplitude is set below 1 nm. (b) New configuration. The tuning fork is oriented parallel with respect to sample surface and the tip vibrates along the z direction. The oscillation amplitude needs to be large at around 10nm. To highlight the tip, its relative size with respect to the tuning fork is sketched much larger than in the real situation.

It has been theoretically predicted and experimentally proved that the enhanced near-field is very much confined to the tip apex within less than 10 nms range, and the field intensity decays approximately exponentially with tip-sample distance[132, 208, 137]. Based on this, our basic idea is to orient the tuning fork vibration perpendicular to the sample surface and drive an oscillation amplitude larger than the near-field decay length. When the tip gets closest to the sample, the near-field signal is “on”; when the tip moves to the farthest point, the sample is out of the near-field interaction range and the near-field signal

is “off”. In our conventional configuration, the tuning fork together with the tip vibrates parallel to sample surface and we use the so-called shear-force to control tip-sample distance; In the new configuration, we bend the tuning fork legs by 90° and orient it parallel to sample surface so that the tip vibrates in z direction. The schemes of conventional and new configurations are shown in Figure 5.2.

This new configuration works similar to a tapping mode AFM and the normal force between tip and sample is used to determine the tip-sample distance. Unlike most AFM systems which employ mechanically stable tips, we exploit soft gold tips which are needed for efficient signal enhancement (See section 2.3). Compared with a conventional shear-force tuning fork configuration, the normal force applied to the tip is magnitudes larger than the shear force. This is a challenging experimental condition and the feedback needs to be more carefully controlled.

5.1 Near-field signal extraction using Lock-in amplifier

After the setup modification, the most straightforward idea is to make use of the lock-in amplifier and extract the near-field part in phase with the tip vibration. Figure 5.3 is a schematic diagram of the lock-in connections. The APD output goes to the input channel and the easy PLL detector (See Figure 3.1) sends the sine wave tuning fork signal with frequency f into the lock-in reference channel. The output of the lock-in is connected to SPM controller and read out in the scanning software.

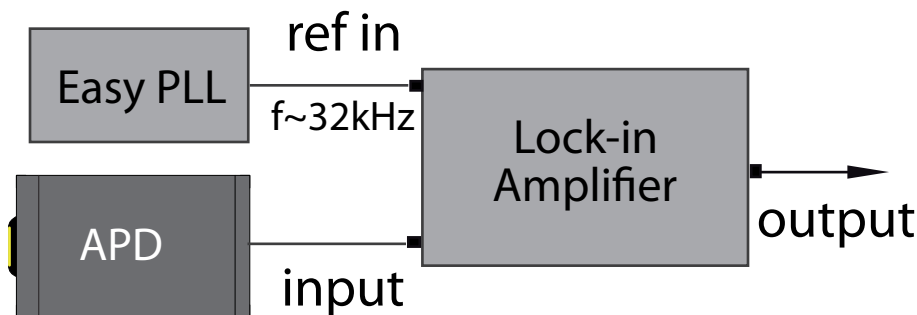


Figure 5.3: The schematic of the lock-in amplifier connections. The Lock-in takes the APD signal as input and the tuning fork signal as reference.

To test if the new arrangement can work as expected, we started from line scans with increasing tuning fork/tip vibration amplitudes. Figure 5.4 (a) shows a near-field PL image of (6,5) SWCNT achieved with the conventional configuration. This nanotube exhibited

very bright PL and the spatial resolution is seen to be around 20 nm. After recording the image, we switched to the new configuration, kept making the same line scan (labeled by the white dashed line) and monitored the lock-in output under different tuning fork signal peak values (tip vibration amplitudes). We assume the near-field intensity decays exponentially with tip-sample distance, then the near-field PL intensity can be expressed as:

$$I_{PL} = e^{-\frac{1}{L}(Z_0 + Z_{mod}(\cos(\omega t)))} = e^{-\frac{Z_0}{L}} e^{-\frac{Z_{mod}}{L}(\cos(\omega t))} \quad (5.1)$$

Here L is the near-field decay length, Z_0 is the average tip-sample distance and Z_{mod} is the tuning fork vibration amplitude or modulation depth. If we do Fourier transformation to the function $\exp(-\frac{Z_{mod}}{L}(\cos(\omega t)))$, The lock-in output is proportional to the amplitude of the first Fourier coefficient A_1 . We calculated how the lock-in output changes with varying Z_{mod}/L in Matlab. The result is plotted in Figure 5.4 (b). There is a linear relationship when $Z_{mod}/L < 1$, but the lock-in output increases faster when the tuning fork vibration amplitude is larger than the decay length. We should note that this only applies to the case of strong signals such as in s-SNOM. In the case of very weak emitters, the signal intensity and the associated noise have to be considered as we will discuss in the next section. This leads to an optimal Z_{mod}/L ratio.

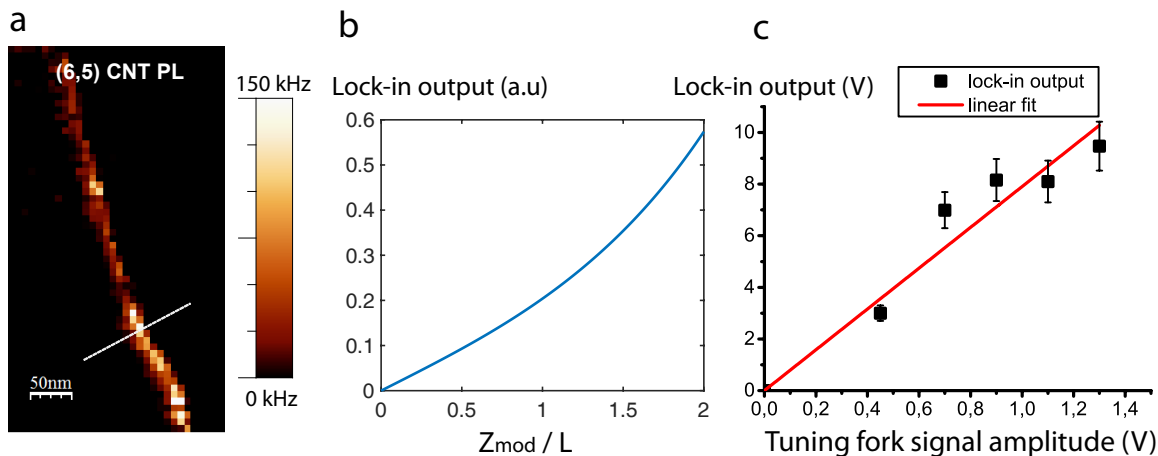


Figure 5.4: Lock-in detection of the near-field PL of a SWCNT. (a) Near-field PL image of a single SWCNT achieved by conventional configuration. The spatial resolution is around 20 nm. (b) The calculated Lock-in output against Z_{mod}/L . When the tip vibration amplitude is smaller than the near-field decay length, a linear relationship between lock-in output and Z_{mod}/L exists. (c) Lock-in output plotted against the tuning fork signal amplitude in the new configuration. The red line represents the linear fit.

The corresponding experimental result is plotted in Figure 5.4 (c). In the conventional configuration, the tuning fork signal amplitude is usually set below 0.4 V with its real

travel range less than 1 nm. Here we increased the amplitude stepwise until it approached 1.3 V which is 3-4 times the normal value. Given that the typical near-field decay length of a gold tip is around 10 nm [132], our data points still lie within the region where $Z_{mod}/L < 1$ and they should follow a linear relationship. The red line in (c) represents the linear fit. Generally there is a good agreement between the data and the linear fit. Possible error origins are tip scattered light and noise. Hereby we confirmed the near-field signal could be extracted and observed that the demodulated near-field signal by the lock-in increased with the tuning fork/tip vibration amplitude.

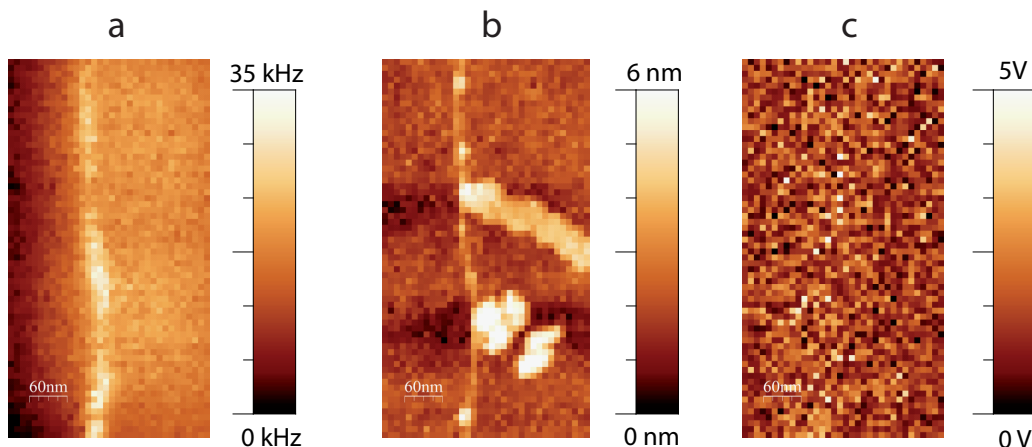


Figure 5.5: Near-field measurements on a single SWCNT with the new configuration. (a) Near-field PL. The spatial resolution is around 25 nm. (b) Topography. (c) Lock-in output. No substantial extracted signal could be observed.

After test measurements, the goal was to obtain lock-in detected near-field signal repeatedly and stably in a scanning image. Typical measurement results are shown in Figure 5.5. (a) shows distinct NF PL and (b) displays clear nanotube topography together with some features with a few nms height possibly due to residual surfactants or impurities. This proves that the feedback is working fine and the setup can be operated in the new normal mode configuration. However, in (c) no lock-in output signal can be observed as in Figure 5.4 (b).

The reason is that the optical signal is too weak to distinguish a substantial signal modulation. In Figure 5.5 the near-field PL intensity is below 35 kHz, meaning that on average we have only one photon per modulation period. Only when the count rate is way larger than the modulation frequency 32 kHz, as the case in Figure 5.4, a significant signal modulation can be expected. However, due to photostability issues, the PL intensity of SWCNT usually can't stably stay above 40 kHz in a near-field scanning image, as shown in Figure 5.5.

To sum up, we proved that we can modify the tip vibration perpendicular to the sample surface and successfully conducted near-field measurements in normal-mode operation. The

lock-in amplifier, indeed, can extract the near-field contribution but only with a sufficiently large signal, i.e. with count rates substantially larger than the modulation frequency, which is unrealistic for SWCNTs and a wide variety of other nanomaterials. This requires us to further develop the technique and broaden its application range.

5.2 Far-field signal separation and subtraction exploiting tunable switch

In this section we will introduce how we separated the far-field background and removed it from the detected signal employing a tunable switch. The basic idea is still the same: the tip vibrates in z direction and we strongly drive the tuning fork so that the near-field signal changes substantially within the tip's travel range.

The upper part of Figure 5.6 shows an approach curve in which the PL intensity was plotted against tip-sample distance. It was taken when the feedback was turned off and we forced the tip to go up or down by changing the z-piezo voltage. Black crosses are the measured data points and the red curve is a fit using an exponential decay. The decay length is approximately 10 nm.

The lower part of Figure 5.6 displays the periodic tuning fork signal. As already mentioned in the previous section, the amplitude of the sine wave represents the travel range of the tip. Since the near-field signal decays rapidly with distance, if the tip vibration amplitude is large enough, one can reach a distance where the near-field contribution is very weak and the far-field signal dominates. This region is labeled in yellow. If we are able to separate this part and remove the corresponding signal contribution from the overall signal, what is left would be mostly the near-field part.

The separation of the far-field signal was accomplished with the help of a tunable switch. Figure 5.7 shows how the switch works. The input channel accepts the APD TTL pulses, and an additional reference channel takes in the tuning fork signal. The switch has a tunable threshold. Only when the tuning fork signal magnitude is larger than its threshold, the switch is on and TTL pulses can go through. In this way, we can distinguish the signal generated when the tip is relatively far from the sample, and control which fraction of the input signal goes through by adjusting the threshold value. Compared with the method using lock-in amplifier described in the previous section, the main difference is that we can adjust the threshold while lock-in detection corresponds to a fixed set point.

The experimental setup including the switch is shown in Figure 5.8. The Easy PLL controller provides the tuning fork signal to the switch through the reference channel. A copy of the APD signal goes to the input channel. In the experiment we obtain the APD output (total signal) and switch output (far-field) simultaneously. The far-field suppressed signal is calculated by subtracting the switch output from APD output with a scaling factor, which will be described in the next section.

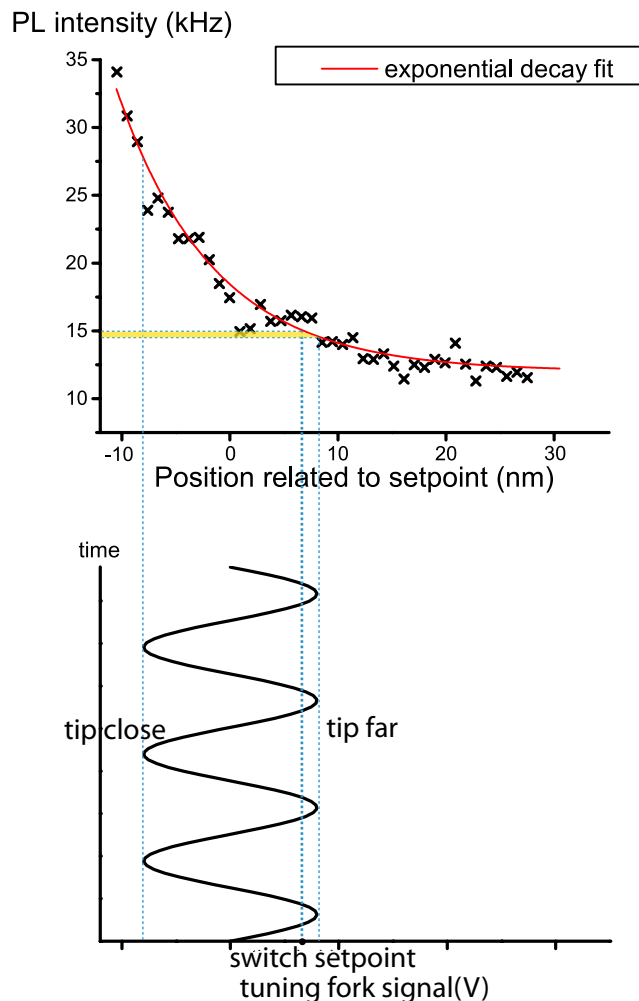


Figure 5.6: Upper part: PL approach curve measured on a single SWCNT using the new configuration with the tuning fork oscillating normal to the surface. Lower part: periodical oscillation of tuning fork & tip and its correlation with the approach curve. With a sufficiently large vibrational amplitude, when the tip moves to the farthest point, the far-field contribution dominates the signal. This range is marked in yellow.

5.2.1 Theoretical calculations

In this experiment there are two tunable variables: the modulation depth, i.e. tip vibration amplitude Z_{mod} and the switch threshold Z_t . In order to separate the far-field signal and meanwhile reserve the near-field contribution, these two variables need to be optimized. We first performed theoretical calculations to find the optimal Z_{mod} and Z_t and to guide the following experiments.

Our model is based on the following assumptions:

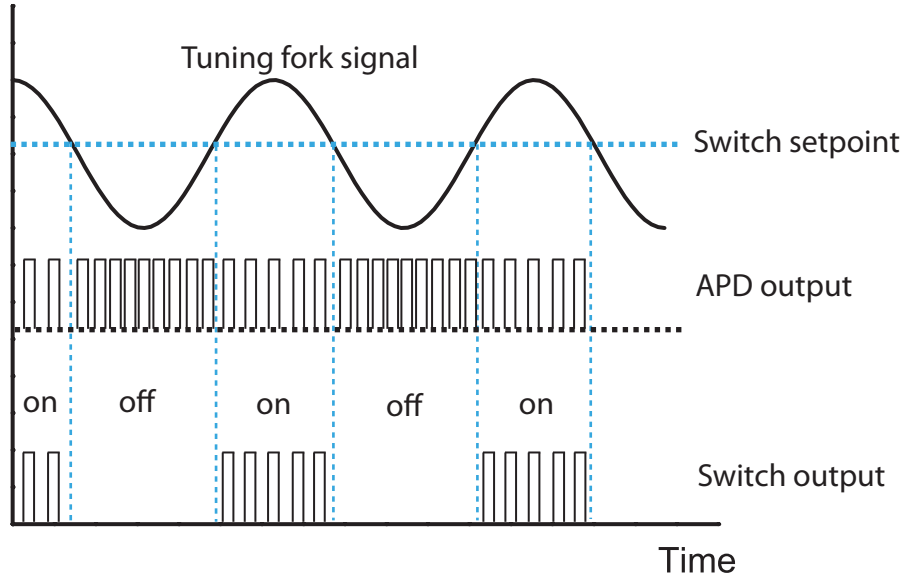


Figure 5.7: An illustration explaining how the switch works. It is on only when the tuning fork signal is larger than the setpoint. One can tune the setpoint to determine which part of the detected APD counts pass through.

- The near-field signal intensity features an exponential decay with distance. The decay length is called L . From figure 5.6 this is a fair assumption, and we start with $L = 10\text{nm}$.
- The far-field background is constant with time.
- The smallest tip-sample distance is a fixed value l . We start with $l = 2\text{nm}$.
- We only consider the shot noise associated with the detection of Poisson distributed photons. If I is the measured signal, the shot noise follows $dI \sim \sqrt{I}$ [209].
- A certain dark count I_{DC} exists.

Besides Z_{mod} and Z_t , we define Z_0 as the average tip-sample distance when the tip is at mid-point. It's easy to find $Z_0 = Z_{mod} + l$. t_t is defined as the time when the tuning fork signal equals the threshold value for the first time, $Z_{mod} \cdot \cos(t_t) = Z_t$. T is the vibration period. These variables are shown in Figure 5.9.

In one vibrational period, the total signal I_{zm} can be expressed as:

$$I_{zm} = \int_0^T e^{-\frac{1}{L}(z_0 + Z_{mod}\cos(\omega t))} dt + I_{DC} \quad (5.2)$$

The output signal of the switch is calculated by the same integral, although limited to the time interval 0 to t_t . The factor 2 takes into account the second period in which the

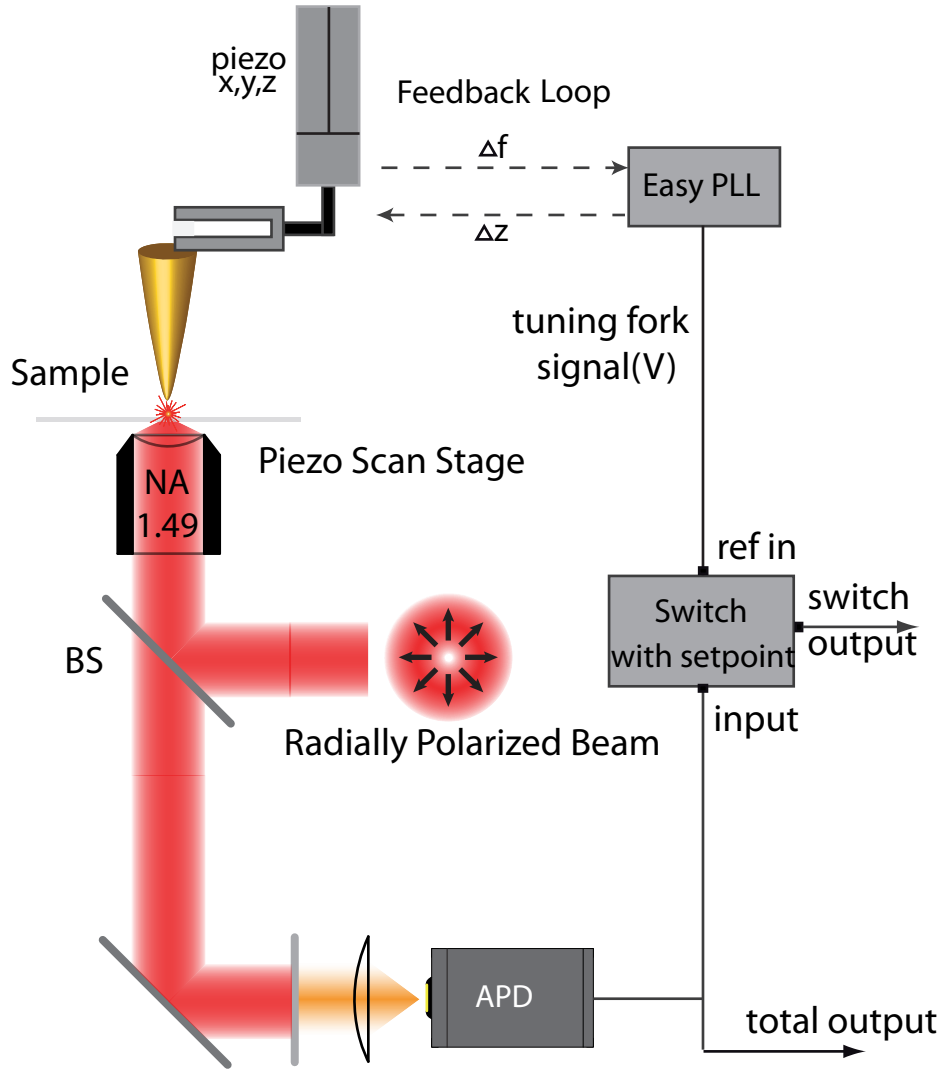


Figure 5.8: Experimental setup with the switch connected. The tuning fork signal is provided by the Easy PLL controller. We monitor the APD output and switch output at the same time. The far-field suppressed signal is calculated by subtracting the switch output from APD output with a scaling factor, which will be described in the next section.

tuning fork signal surpasses Z_t (see Figure 5.9). For the dark signal I_{DC} we need to take a scaling factor $c = T/(2t_t)$ into consideration, so we have:

$$I_{zt} = 2 \int_0^{t_t} e^{-\frac{1}{L}(z_0 + Z_{mod} \cos(\omega t))} dt + I_{DC}/c \quad (5.3)$$

The total far-field signal is c times of I_{zt} , thus the background subtracted signal $S = I_{zm} - c \cdot I_{zt}$

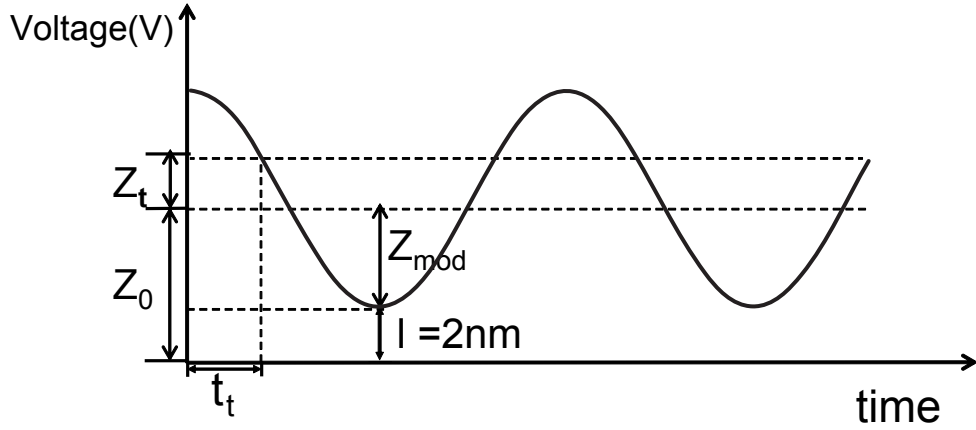


Figure 5.9: An illustration of the parameters used in the calculation.

The noise of S is:

$$dS = \sqrt{\left(\frac{\partial S}{\partial I_{zm}}\right)^2 (dI_{zm})^2 + \left(\frac{\partial S}{\partial I_{zt}}\right)^2 (dI_{zt})^2} = \sqrt{(dI_{zm})^2 + c^2 (dI_{zt})^2} = \sqrt{I_{zm} + c^2 I_{zt}} \quad (5.4)$$

The final signal to noise ratio is S/dS :

$$S/dS = \frac{I_{zm} - c \cdot I_{zt}}{\sqrt{I_{zm} + c^2 I_{zt}}} \quad (5.5)$$

In a first step, we ignore the effect of I_{DC} , i.e. we set $I_{DC} = 0$. Then we plotted signal S , signal to noise ratio S/dS against the modulation depth Z_{mod} and the threshold value Z_t/Z_{mod} in Figure 5.10.

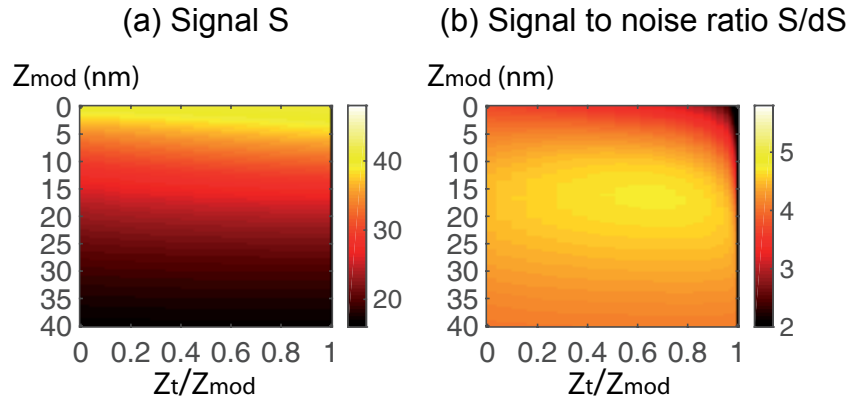


Figure 5.10: Calculated S and S/dS against the modulation depth Z_{mod} and the switch threshold Z_t/Z_{mod} when $I_{DC} = 0$.

In the left part of Figure 5.10, we could see that the far-field background subtracted signal remarkably drops with larger modulation depth, because the near-field intensity decays very fast in z direction. Even a small increase of Z_{mod} requires a very large Z_t/Z_{mod} value to make up for the loss of near-field signal. However, in the right part of Figure 5.10, we don't have the best signal to noise ratio when signal is the strongest. Instead, the largest S/dS appears at the point with $Z_{mod} \approx 15nm$, $Z_t/Z_{mod} \approx 0.65$. This means that the optimal Z_{mod} and Z_t/Z_{mod} always come from a compromise. If Z_{mod} is too large or Z_t/Z_{mod} is too small, we lose the signal enhancement because the tip is too far away or the near-field is subtracted together with the background; if Z_{mod} is too small or Z_t/Z_{mod} is too large, i.e. the time interval in which the far-field contribution is determined ($2 \times t_t$) becomes very short and hence c becomes very large, the shot noise becomes substantial and reduces the S/N ratio.

Next we investigated how S/dS is affected by different levels of the dark count I_{DC} . The results are shown in Figure. 5.11. From left to right I_{DC} was set to be 0, 1% of maximum I_{zm} and 10% of maximum I_{zm} respectively.

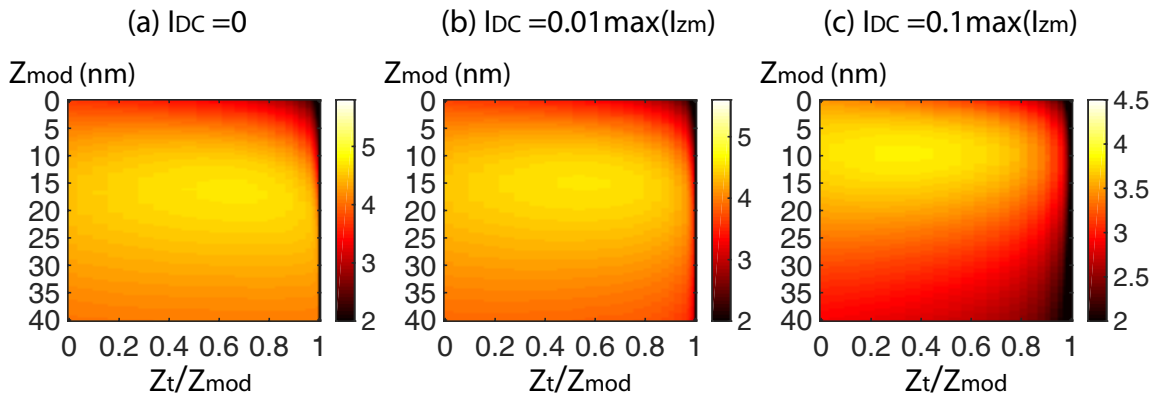


Figure 5.11: Calculated signal to noise ratio S/dS against the modulation depth Z_{mod} and the switch threshold Z_t/Z_{mod} under different dark count levels. From left to right, I_{DC} was set as 0, 1% of maximum I_{zm} and 10% of maximum I_{zm} respectively.

Figure. 5.11 shows that the existence of dark counts lowers the S/N ratio and reduces the optimal value of both Z_{mod} and Z_t/Z_{mod} . In equation 5.5, I_{DC} is canceled out in S and only exists in $dS = \sqrt{I_{zm} + c^2 I_{zt}}$. With a moderate I_{DC} , we just need to reduce c a little to compensate the extra noise signal in I_{zm} and I_{zt} , therefore in Figure 5.11(b) Z_t/Z_{mod} drops a bit. However, with a strong I_{DC} both I_{zm} and I_{zt} gets much larger, besides reducing c one must also decrease Z_{mod} to have a substantial near-field signal. That's why we observe a clear shift in Figure 5.11(c). This also reminds us to suppress the dark counts in experiments.

Subsequently we studied the influence of the smallest tip-sample distance l which indicates how close the tip can approach the sample surface. I_{DC} is kept constant at 1% of

the near-field signal (as in Figure. 5.11(b)), l is set as 2 nm, 5 nm and 10 nm respectively. Figure. 5.12 displays the calculation results.

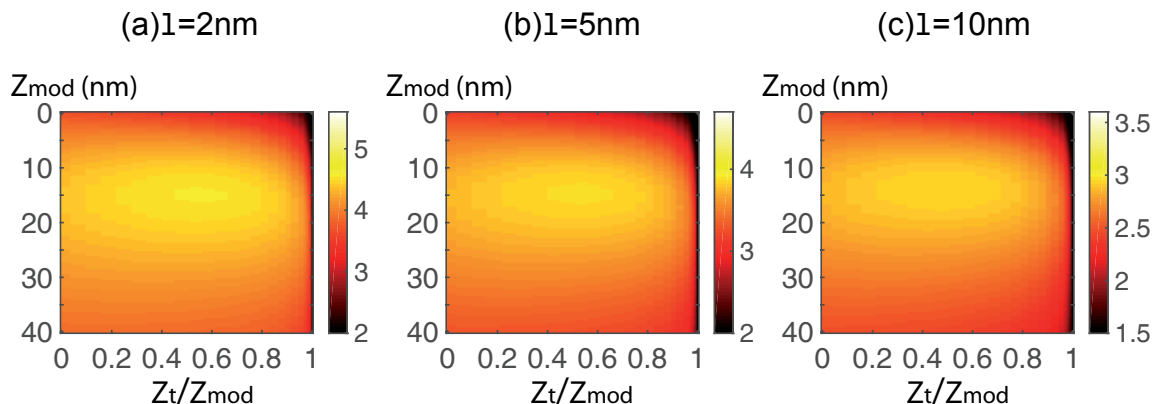


Figure 5.12: Calculated signal to noise ratio S/dS against the modulation depth Z_{mod} and the switch threshold Z_t/Z_{mod} with different smallest tip-sample distance l . From (a) to (c), l equals to 2 nm, 5 nm, 10 nm.

A greater tip-sample distance means the tip is farther away and the effective near-field signal gets lower, therefore the best S/N ratio drops from (a) to (c). We also noticed that the optimal Z_{mod} doesn't depend on l but the optimal Z_t/Z_{mod} slightly decreases with l going from 2 nm to 10 nm. With the same modulation depth, a greater l means the tip is generally closer to far-field region, so Z_t/Z_{mod} needs to be reduced to distinguish the far-field contribution. Generally, the effect of l is not very strong. This is somewhat surprising given the rapid exponential decay of the near-field contribution with a decay length of 10 nm.

Finally we looked at the impact of the near-field decay length L . We fixed $l = 2$ nm and I_{DC} as 1% of the near-field intensity, then did the calculations with $L = 5$ nm, 10 nm and 15 nm. The range of Z_{mod} is from 0 to $4L$. The outcome is illustrated in Figure 5.13.

The first conclusion is that an ascending decay length L brings a larger S/N ratio, because the near-field signal decays slower and gets stronger with respect to far-field counterpart and noise. Regardless of the difference of the modulation depth range (y-axis), these three figures exhibit a very similar pattern. The best S/N ratio always shows up when $Z_{mod} \approx 1.5L$ and $Z_t/Z_{mod} \approx 0.6$. This indicates Z_t/Z_{mod} is independent from L but Z_{mod} strongly relies on L . Basically, the modulation depth must be larger than L so that tip can enter far-field dominated region, but meanwhile it can't be too large to lose signal enhancement. In our model, 1.5 times of decay length seems to be the trade-off point. The strong dependence of Z_{mod} on L agrees with previous work[203].

All of the aforementioned calculations were done in Matlab. The Matlab script is attached in appendix A.

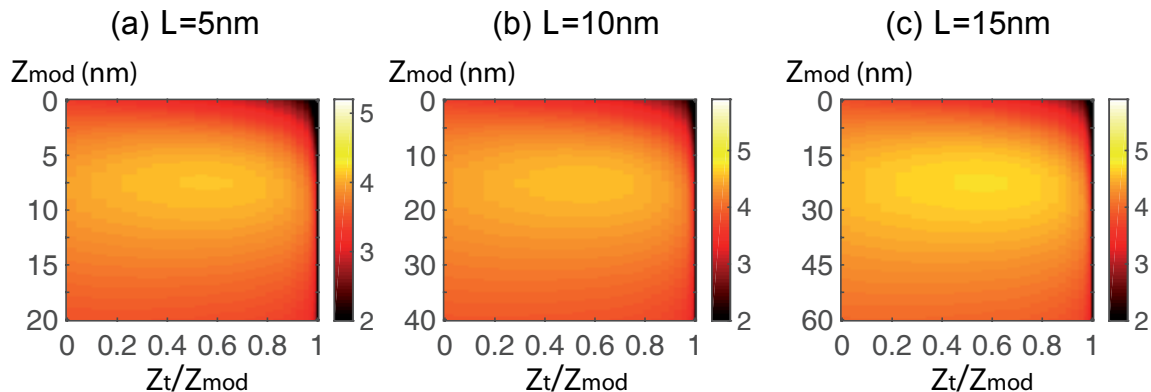


Figure 5.13: Calculated signal to noise ratio S/dS against the modulation depth Z_{mod} and the switch threshold Z_t/Z_{mod} with different near-field decay length L . From left to right, L was set as 5 nm, 10 nm, 15 nm.

To sum up, we looked into how the S/N ratio changes as a function of Z_{mod} and Z_t/Z_{mod} under various conditions. It was revealed that a lower noise level, a larger near-field decay length and a smaller minimum tip-sample distance promote a better S/N ratio. Furthermore, these factors also have a huge effect on the optimal modulation depth and switch threshold. For instance, the optimal Z_{mod} firmly depends on the near-field decay length with a relationship $Z_{mod} \approx 1.5L$. Dark counts and other sources of noise could take both Z_{mod} and Z_t/Z_{mod} down to a large extent. The calculations provided us with valuable guidelines for parameters selection in the experiments.

5.2.2 Experimental Realization

We applied the new scheme (presented in section 5.2.1) to PL detection of SWCNTs. In the experiments we obtained the APD signal I_{zm} and switch output I_{zt} simultaneously from two data channels (See Figure 5.8), then we calculated the background subtracted signal using $S = I_{zm} - c \cdot I_{zt}$. Representative data are presented in Figure 5.14.

Figure 5.14 (a) shows the total APD signal (total output). The spatial resolution is seen to be about 25 nm. Both sharp near-field PL of the nanotube and considerable far-field background could be observed. Figure 5.14 (b) illustrates the switch output which is dominated by the far-field signal. This means the extraction of far-field contribution works. Figure 5.14 (c) is the background subtracted signal. The far-field background is remarkably reduced and the profile of the nanotube PL is much more clear than in (a).

To further confirm the separation of the near-field signal, we looked at the intensity profile (labeled by blue dashed line) crossing the nanotube in the total output and the background subtracted images. They are shown in Figure 5.14 (d) and (e). The profile in (a) consists of two parts: a spatially confined sharp near-field peak and a widely spread far-

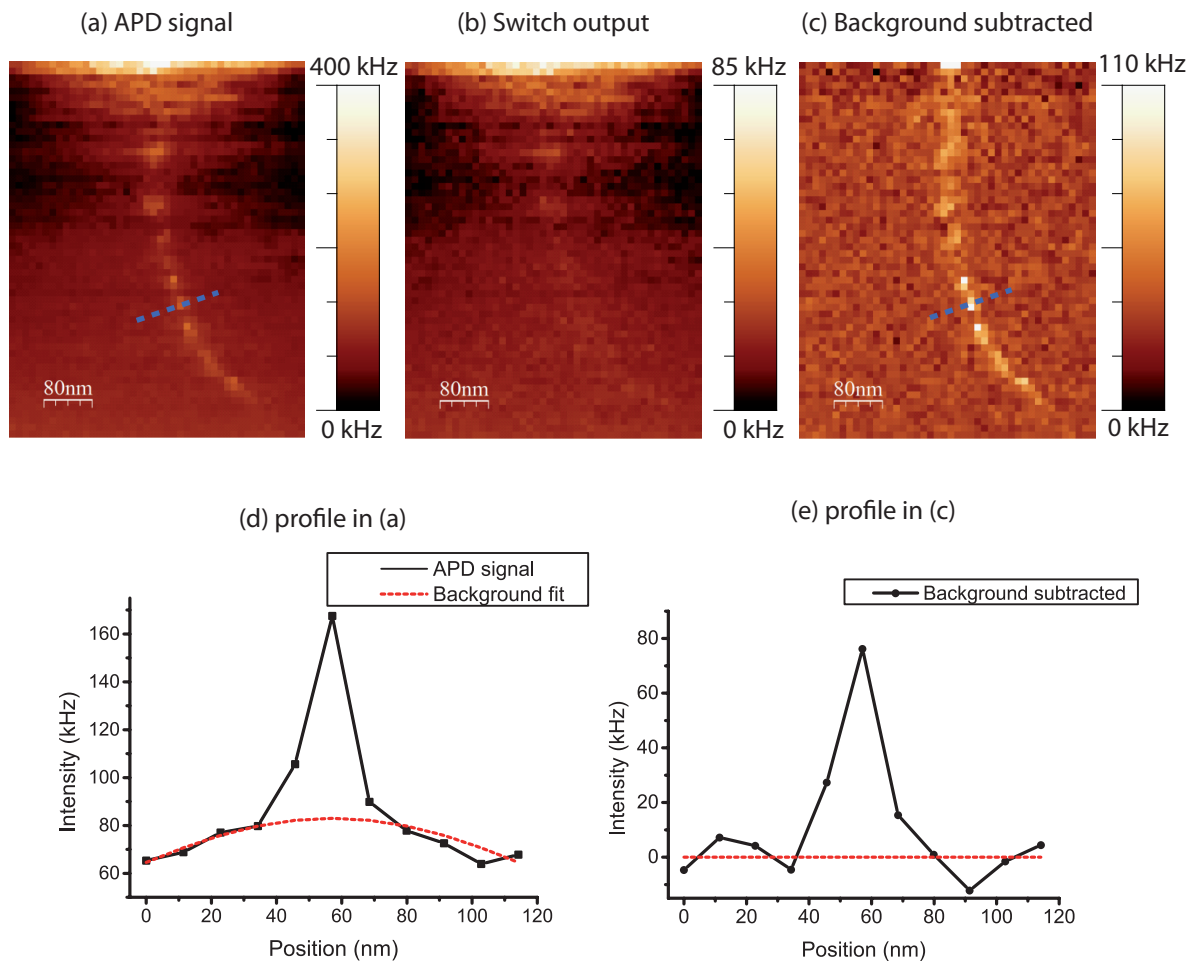


Figure 5.14: (a) APD signal includes both near-field and far-field signal. (b) Switch output is dominated by far-field contribution. (c) background subtracted signal $S = I_{zm} - c \cdot I_{zt}$. Far-field background is significantly reduced. (d) The intensity profile along the nanotube in (a). Both near-field and far-field signal could be observed. Far-field signal exhibits a quasi-Gaussian peak. (e) The intensity profile crossing the nanotube in (c). The spatially confined near-field peak is reserved and the background counts fluctuate around 0.

field background. The background can be fitted using a Gaussian peak function (red dashed line in (d)). After subtraction, in (e) the near-field peak persists but the background counts fluctuate around 0, indicating that the far-field part is greatly suppressed. The signal to background ratio in (c) is significantly higher than the original image (a).

In this measurement the tuning fork signal peak was 2V, and the real tip amplitude is estimated to be around 10 nm[210, 182]. The switch threshold was set with $Z_t/Z_{mod} \approx 0.8$. It is a little different from the optimal value predicted in section 5.2.1. The possible reason for this deviation could be the scattered light from the gold tip and the potential interference between light scattered by tip and sample, which were not included in our model. They could modify the signal and alter the S/N ratio.

In conclusion, we implemented a new tuning fork configuration in which the tip oscillates normal to the sample surface in our TENOM setup and successfully conducted near-field measurements on SWCNT PL with the new configuration. In order to separate near-field and far-field contributions, we explored two different approaches: first, using a lock-in amplifier to extract the near-field signal and second, implementing a tunable switch to determine the far-field signal. With the first method, we observed that the extracted near-field signal increased with a larger tip vibration amplitude. However, this method requires the count rate of the input signal to be much greater than the tuning fork frequency 32 kHz, and the limited photo-stability of SWCNT PL prevents us from achieving a complete scanning image. The second method involves a switch with a tunable threshold above which the input signal can go through. We first performed a series of theoretical model calculations to find the optimal modulation depth Z_{mod} and switch threshold Z_t/Z_{mod} . It was found that the optimal Z_{mod} and Z_t/Z_{mod} values are determined from a compromise between a substantial signal enhancement and a reasonable shot noise level. The dark counts and other noises can stiffly bring down both values. Under a certain noise level, Z_{mod} only depends on the decay length L and Z_t/Z_{mod} only relies on the smallest tip-sample distance l . Then the new configuration was applied to SWCNT PL imaging. We proved that the signal to background ratio was drastically enhanced after subtraction of the far-field signal. Our calculation is applicable to all s-SNOM setups and can provide insight on the tip-sample distance selection for near-field measurements. Although the experiments were focused on PL, our technique is ready to be used for other spectroscopic processes such as Raman scattering or absorption. It is expected to find applications for a wide range of nanomaterials, especially the ones with weak optical response which require high detection sensitivity.

Summary and Outlook

In this thesis, we utilized the advantages of TENOM to investigate the optical and optoelectronic properties of single-walled carbon nanotubes (SWCNTs), then further modified the configuration for an enhanced signal to background ratio and a higher detection sensitivity.

In the first part of the thesis, simultaneous near-field Raman, PL and topography images were recorded on individual polymer wrapped SWCNTs. The uniform near-field Raman intensity indicated the structural homogeneity of the nanotubes. On the contrary, the near-field PL intensity showed substantial fluctuations along the nanotube, which could not be observed in confocal images. The PL intensity fluctuation reflects the quenching effect from defects, nanotube ends or charges and exciton localization due to a local energy minima. The level of PL intensity fluctuation was quantitatively evaluated by a newly introduced statistical parameter C_v . A larger value of C_v means a stronger fluctuation and indicates a more frequent occurrence of exciton trapping and quenching sites. The comparison of C_v values from different SWCNT samples reveals important information on the sample quality and polymer/SWCNT interaction. In the literature a large number of polymers/surfactants have been used to prevent the aggregation of SWCNTs and sort out a single chirality for practical applications. In our work, we studied SWCNT samples with two commonly used wrapping agents, PFO-BPy and single stranded DNA. In addition, to look into the possible effect of post-synthesis treatment, we used both commercially available CoMoCAT nanotubes (with acid treatment to remove catalysts) and CVD-synthesized nanotubes (without treatment). Based on the measurement data on a sufficient number of individual SWCNTs, it was found that PFO-BPy wrapped SWCNTs generally showed a smaller C_v value than DNA-wrapped ones, therefore PFO-BPy is a more suitable wrapping agent for the applications that require exciton diffusion such as organic solar cells. In addition, PFO-BPy wrapped CoMoCAT and CVD-synthesized SWCNTs exhibited similar C_v average values but the CoMoCAT nanotubes had a wider distribution. This indicates that the intrinsic properties of SWCNT don't have a strong influence and PFO-BPy wrapping can improve the optical homogeneity of nanotubes with a moderate defect concentration.

The significance of the aforementioned work lies in the following aspects: (1) To our knowledge, this is the first time the near-field PL intensity variation is quantitatively characterized and connected to the polymer/SWCNT interaction. The statistical parameter introduced in our analysis is ready to be applied to other 1D or 2D nanomaterials. (2) We compared the effects from different wrapping agents and post-synthesis treatment. This

provides useful information for the fabrication of SWCNT-based devices.

Possible error sources include: (1) the far-field background which is always present in the near-field images recorded with the used scheme. Although we selected the images with a large signal enhancement factor, i.e. the near-field intensity should be much larger than the confocal background, the far-field signal could still slightly change the C_v value. (2) The possible blinking of nanotubes during measurement. This could cause an abrupt change in PL intensity. Based on that, we suggest the following steps for further investigations: (1) Refine the technique to suppress the influence of far-field background. This is realized in the second part of the thesis. (2) Conduct the measurement at low temperature in vacuum or inert gas. Firstly, this could significantly suppress the blinking or bleaching, which is usually assisted by oxygen or water in the air. Secondly, this would enable us to get clear spectroscopic data. There were some attempts for spectroscopic imaging, i.e. recording the emission energy along the nanotube. However, in order to collect a substantial signal, we had to use a high excitation power and long integration time, and most of the experiments were not successful due to photobleaching. Moreover, at room temperature the PL peak from single nanotubes is quite broad owing to exciton-phonon interactions (See section 4.2). At low temperature the PL linewidth would decrease and emission energy shift is easier to be observed. (3) Include more types of wrapping agents and enlarge the dataset. Only two types of wrapping agents were compared in this work. There are other widely used surfactants such as DOC well worth studying. Furthermore, it is known that different PFO derivatives show selectivity for different SWCNT chiralities, like PFO for (7,5) and PFO-BPy for (6,5), thus it would be interesting to compare the wrapping effect between them.

In the second part of the thesis, we implemented a new tuning fork configuration in which the tip oscillates normal to the sample surface. In this way, the normal-force between tip and sample, which is magnitudes larger than the shear-force, is used to control the tip-sample distance. For a long time the gold tip has been considered not fit for normal-force feedback due to its softness. However, we showed that with careful handling, TENOM measurements could also be successfully conducted with the new configuration. As the next step, we drove a large tip oscillation amplitude and explored two approaches to separate the near-field and far-field signal. The first approach is the signal demodulation at the tip vibration frequency using a lock-in amplifier. We found that this method is useful only when the count rate of the input signal is much greater than the tuning fork frequency of 32 kHz. The second approach involves a switch with a tunable threshold above which the input signal can pass. The idea is to extract a certain part of the far-field signal and subtract the far-field contribution from the overall signal with a scaling factor. In this approach there are two variable parameters: the modulation depth Z_{mod} and the switch threshold Z_t/Z_{mod} . Through a series of theoretical calculations, we found that the optimal Z_{mod} and Z_t/Z_{mod} values are determined from a comprise between a substantial signal enhancement and a reasonable shot noise level. A higher level of dark counts and other noises would bring down both optimal values. Below a certain noise level, Z_{mod} only depends on the decay length L of the enhanced near-field and Z_t/Z_{mod} only relies on the smallest tip-sample distance l .

Finally the new configuration was applied to PL imaging of SWCNT, and we proved that the signal to background ratio was significantly improved after subtraction of the far-field signal.

The significance of this part of work lies in the following aspects: (1) we demonstrated that our TENOM setup can be operated using the new configuration with normal-force feedback, (2) our theoretical calculations provided general guidelines for parameters selection in SNOM measurements, and (3) we developed a new approach to enhance the signal to background ratio in TENOM measurements and experimentally proved it. Suggestions for further investigations include: (1) A supplement measurement for the real amplitude of tuning fork. Knowing the real modulation depth would enable us to optimize the switch threshold Z_t/Z_{mod} according to the calculation. (2) Extend the application of this technique to 2D nanomaterials. Compared with 1D nanomaterials like SWCNT, the near-field signal of 2D materials is more difficult to detect because of the larger far-field background. We believe that our technique would have great application prospects in this field.

Appendix: Matlab Scripts

Script A

The relationship between lock-in amplifier output with tip modulation depth Z_t/Z_{mod} (Please see section 5.1 figure 5.4).

```
function [f, yf, yy] = fourierOfTip(k, omega)
    noPoints = 2^18;
    dt = 2*pi/ omega / 100;
    df = 1/dt/noPoints;
    t = (0:noPoints-1) * dt;
    y = exp(-k*cos(omega * t));
    f = (0:noPoints-1) * df;
    yf = dt * fft(y);
    yy = sum (dt* y);
end

k = 0.2;
[f, yf, yy] = fourierOfTip(k, 1.885e5);
plot(f, abs(yf))
xlim([0,10])

ks = 0. : 0.01: 2;
res = 0 * ks;
m = 0* ks;
for i = 1:length(ks)
    [f, yf, yy] = fourierOfTip(ks(i), 1.885e5);
    res(i) = sum(abs(yf(1.336e5:1.338e5)));
    m(i) = res(i) /yy;
end

figure(2)
plot(ks, res)
```

We note it again that this model ignores the shot noise and only applies to very strong signals.

Script B

The calculation of optical modulation depth and switch threshold (See section 5.2.1)

```
clear all
wtsteps=100;

%omega*t
wt=linspace(0,2*pi,wtsteps);

%ztzm z_threshold / z_modulation
nztzm=100;
ztzm=linspace(0,1,nztzm);

%exponential decay length
L=10;

%modulation steps
nzm=100;
%modulation depth zm
zm=linspace(0,4*L,nzm);

%l
l=2;

%z0
z0=zm+l;

%Total Intensity with modulation
Izm=zeros(1,nzm);

%Intensity above threshold
Izt=zeros(nzm,nztzm);
%Signal
S=zeros(nzm,nztzm);

%Variance as sqrt(s)
DS=zeros(nzm,nztzm);

%far-field in one period, this value doesn't depend on any parameter
FF=exp(-1/L);

%Dark counts
%DC=sum(exp(-1/L*(z0(1)+zm(1).*cos(wt))))./100;
%this DC depends on l, exp(-1/L)
```

```
DC=wtsteps*exp(-2/L)./100
%DC=0;
%t_threshold /2
wtt=round(acos(ztzm).*wtsteps/(2*pi));

%scaling factor
c=wtsteps./(4*wtt);

for n=1:nzm
    Izm(n)=sum(exp(-1/L*(z0(n)+zm(n).*cos(wt))))+DC;
    for m=1:nztzm
        Izt(n,m)=2.*sum(exp(-1/L*(z0(n)+zm(n).*cos(wt(1:wtt(m))))))+DC.*(1/c(m));
        S(n,m)=Izm(n)-c(m).*Izt(n,m);
        DS(n,m)=sqrt(Izm(n)+c(m).^2.*Izt(n,m));
    end
end

SDS=S./DS;
figure(1)
imagesc(ztzm,zm,SDS)
colormap (hot)
colorbar
```


Bibliography

- [1] S. Diao, J. L. Blackburn, G. Hong, A. L. Antaris, J. Chang, J. Z. Wu, B. Zhang, K. Cheng, C. J. Kuo, and H. Dai, “Fluorescence imaging in vivo at wavelengths beyond 1500nm,” *Angewandte Chemie*, vol. 127, no. 49, pp. 14971–14975, 2015.
- [2] Z. Liu, J. T. Robinson, S. M. Tabakman, K. Yang, and H. Dai, “Carbon materials for drug delivery & cancer therapy,” *Materials Today*, vol. 14, no. 7, pp. 316 – 323, 2011.
- [3] P. Simon and Y. Gogotsi, “Capacitive energy storage in nanostructured carbonelectrolyte systems,” *Accounts of Chemical Research*, vol. 46, no. 5, pp. 1094–1103, 2013. PMID: 22670843.
- [4] G. J. Brady, A. J. Way, N. S. Safron, H. T. Evensen, P. Gopalan, and M. S. Arnold, “Quasi-ballistic carbon nanotube array transistors with current density exceeding si and gaas,” *Science Advances*, vol. 2, no. 9, 2016.
- [5] L. Bodiou, Q. Gu, M. Guzo, E. Delcourt, T. Batt, J. Lemaitre, N. Lorrain, M. Guendouz, H. Folliot, J. Charrier, K. S. Mistry, J. L. Blackburn, J.-L. Doualan, A. Braud, and P. Camy, “Guided photoluminescence from integrated carbon-nanotube-based optical waveguides,” *Advanced Materials*, vol. 27, no. 40, pp. 6181–6186, 2015.
- [6] S. Kruss, A. J. Hilmer, J. Zhang, N. F. Reuel, B. Mu, and M. S. Strano, “Carbon nanotubes as optical biomedical sensors,” *Advanced Drug Delivery Reviews*, vol. 65, no. 15, pp. 1933 – 1950, 2013. Carbon Nanotubes in Medicine and Biology: Therapy and Diagnostics & Safety and Toxicology.
- [7] N. Mauser and A. Hartschuh, “Tip-enhanced near-field optical microscopy,” *Chem. Soc. Rev.*, vol. 43, pp. 1248–1262, 2014.
- [8] J. Steidtner and B. Pettinger, “Tip-enhanced raman spectroscopy and microscopy on single dye molecules with 15 nm resolution,” *Phys. Rev. Lett.*, vol. 100, p. 236101, Jun 2008.
- [9] F. M. Huang, F. Festy, and D. Richards, “Tip-enhanced fluorescence imaging of quantum dots,” *Applied Physics Letters*, vol. 87, no. 18, p. 183101, 2005.

- [10] C. Georgi, M. Böhmler, H. Qian, L. Novotny, and A. Hartschuh, “Probing exciton propagation and quenching in carbon nanotubes with near-field optical microscopy,” *physica status solidi (b)*, vol. 246, no. 11-12, pp. 2683–2688, 2009.
- [11] C. Georgi, A. A. Green, M. C. Hersam, and A. Hartschuh, “Probing exciton localization in single-walled carbon nanotubes using high-resolution near-field microscopy,” *ACS Nano*, vol. 4, no. 10, pp. 5914–5920, 2010. PMID: 20857945.
- [12] M. Bhmler, Z. Wang, A. Myalitsin, A. Mews, and A. Hartschuh, “Optical imaging of cdse nanowires with nanoscale resolution,” *Angewandte Chemie International Edition*, vol. 50, no. 48, pp. 11536–11538, 2011.
- [13] J. Stadler, T. Schmid, and R. Zenobi, “Nanoscale chemical imaging of single-layer graphene,” *ACS Nano*, vol. 5, no. 10, pp. 8442–8448, 2011. PMID: 21957895.
- [14] M. Rahaman, R. D. Rodriguez, G. Plechinger, S. Moras, C. Schller, T. Korn, and D. R. T. Zahn, “Highly localized strain in a mos2/au heterostructure revealed by tip-enhanced raman spectroscopy,” *Nano Letters*, vol. 17, no. 10, pp. 6027–6033, 2017. PMID: 28925710.
- [15] N. Rauhut, M. Engel, M. Steiner, R. Krupke, P. Avouris, and A. Hartschuh, “Antenna-enhanced photocurrent microscopy on single-walled carbon nanotubes at 30 nm resolution,” *ACS Nano*, vol. 6, no. 7, pp. 6416–6421, 2012. PMID: 22632038.
- [16] S. Iijima and T. Ichihashi, “Single-Shell Carbon Nanotubes of 1-nm Diameter,” *Nature*, vol. 363, pp. 603–605, 1993.
- [17] S. Maruyama, “Nanotube Coordinate Generator with a Viewer for Windows.” <http://www.photon.t.u-tokyo.ac.jp/maruyama/wrapping3/wrapping.html>.
- [18] G. Dukovic, M. Balaz, P. Doak, N. D. Berova, M. Zheng, R. S. McLean, and L. E. Brus, “Racemic Single-Walled Carbon Nanotubes Exhibit Circular Dichroism when Wrapped with DNA,” *J. Am. Chem. Soc.*, vol. 128, pp. 9004–9005, 2006.
- [19] T. Gokus, *Time-Resolved Photoluminescence and Elastic White Light Scattering Studies of Individual Carbon Nanotubes and Optical Characterization of Oxygen Plasma Treated Graphene*. Ludwig-Maximilians-Universitat M’unchen, 2011. PhD thesis.
- [20] K. F. Mak, L. Ju, F. Wang, and T. F. Heinz, “Optical Spectroscopy of Graphene: From the Far Infrared to the Ultraviolet,” *Solid State Communications*, vol. 152, pp. 1341 – 1349, 2012.
- [21] M. Dresselhaus, G. Dresselhaus, R. Saito, and A. Jorio, “Raman spectroscopy of carbon nanotubes,” *Physics Reports*, vol. 409, no. 2, pp. 47 – 99, 2005.

- [22] M. Machón, S. Reich, C. Thomsen, D. Sánchez-Portal, and P. Ordejón, “Ab initio calculations of the optical properties of 4- μm diameter single-walled nanotubes,” *Phys. Rev. B*, vol. 66, p. 155410, Oct 2002.
- [23] R. Saito, G. Dresselhaus, and M. S. Dresselhaus, *Physical Properties of Carbon Nanotubes*. Imperial College Press, 1998.
- [24] M. A. H. Vozmediano, “Renormalization group aspects of graphene,” *Philosophical Transactions of the Royal Society of London A: Mathematical, Physical and Engineering Sciences*, vol. 369, no. 1946, pp. 2625–2642, 2011.
- [25] N. Hamada, S.-i. Sawada, and A. Oshiyama, “New one-dimensional conductors: Graphitic microtubules,” *Phys. Rev. Lett.*, vol. 68, pp. 1579–1581, Mar 1992.
- [26] R. Saito, M. Fujita, G. Dresselhaus, and M. S. Dresselhaus, “Electronic structure of graphene tubules based on c_{60} ,” *Phys. Rev. B*, vol. 46, pp. 1804–1811, Jul 1992.
- [27] R. Saito, M. Hofmann, G. Dresselhaus, A. Jorio, and M. S. Dresselhaus, “Raman spectroscopy of graphene and carbon nanotubes,” *Advances in Physics*, vol. 60, no. 3, pp. 413–550, 2011.
- [28] C. L. Kane and E. J. Mele, “Size, shape, and low energy electronic structure of carbon nanotubes,” *Phys. Rev. Lett.*, vol. 78, pp. 1932–1935, Mar 1997.
- [29] M. Ouyang, J.-L. Huang, C. L. Cheung, and C. M. Lieber, “Energy gaps in mm-metallic single-walled carbon nanotubes,” *Science*, vol. 292, no. 5517, pp. 702–705, 2001.
- [30] S. Reich, J. Maultzsch, C. Thomsen, and P. Ordejón, “Tight-binding description of graphene,” *Phys. Rev. B*, vol. 66, p. 035412, Jul 2002.
- [31] J. W. Mintmire and C. T. White, “Universal density of states for carbon nanotubes,” *Phys. Rev. Lett.*, vol. 81, pp. 2506–2509, Sep 1998.
- [32] P. Kim, T. W. Odom, J.-L. Huang, and C. M. Lieber, “Electronic density of states of atomically resolved single-walled carbon nanotubes: Van hove singularities and end states,” *Phys. Rev. Lett.*, vol. 82, pp. 1225–1228, Feb 1999.
- [33] A. Jorio, A. G. Souza Filho, G. Dresselhaus, M. S. Dresselhaus, R. Saito, J. H. Hafner, C. M. Lieber, F. M. Matinaga, M. S. S. Dantas, and M. A. Pimenta, “Joint density of electronic states for one isolated single-wall carbon nanotube studied by resonant raman scattering,” *Phys. Rev. B*, vol. 63, p. 245416, Jun 2001.
- [34] H. Kataura, Y. Kumazawa, Y. Maniwa, I. Umezū, S. Suzuki, Y. Ohtsuka, and Y. Achiba, “Optical properties of single-wall carbon nanotubes,” *Synthetic Metals*, vol. 103, no. 1, pp. 2555 – 2558, 1999. International Conference on Science and Technology of Synthetic Metals.

- [35] X. Wei, T. Tanaka, Y. Yomogida, N. Sato, R. Saito, and H. Kataura, “Experimental determination of excitonic band structures of single-walled carbon nanotubes using circular dichroism spectra,” *Nature Communications*, vol. 7, p. 12899, Oct. 2016.
- [36] K.-C. Chuang, A. Nish, J.-Y. Hwang, G. W. Evans, and R. J. Nicholas, “Experimental study of coulomb corrections and single-particle energies for single-walled carbon nanotubes using cross-polarized photoluminescence,” *Phys. Rev. B*, vol. 78, p. 085411, Aug 2008.
- [37] Y. Miyauchi, H. Ajiki, and S. Maruyama, “Electron-hole asymmetry in single-walled carbon nanotubes probed by direct observation of transverse quasidark excitons,” *Phys. Rev. B*, vol. 81, p. 121415, Mar 2010.
- [38] Y. Miyauchi, “Photoluminescence studies on exciton photophysics in carbon nanotubes,” *J. Mater. Chem. C*, vol. 1, pp. 6499–6521, 2013.
- [39] F. Wang, G. Dukovic, L. E. Brus, and T. F. Heinz, “The optical resonances in carbon nanotubes arise from excitons,” *Science*, vol. 308, no. 5723, pp. 838–841, 2005.
- [40] J. Maultzsch, R. Pomraenke, S. Reich, E. Chang, D. Prezzi, A. Ruini, E. Molinari, M. S. Strano, C. Thomsen, and C. Lienau, “Exciton binding energies in carbon nanotubes from two-photon photoluminescence,” *Phys. Rev. B*, vol. 72, p. 241402, Dec 2005.
- [41] S. K. Doorn, P. T. Araujo, K. Hata, and A. Jorio, “Excitons and exciton-phonon coupling in metallic single-walled carbon nanotubes: Resonance raman spectroscopy,” *Phys. Rev. B*, vol. 78, p. 165408, Oct 2008.
- [42] S. Uryu, H. Ajiki, and T. Ando, “Excitonic two-photon absorption in semiconducting carbon nanotubes within an effective-mass approximation,” *Phys. Rev. B*, vol. 78, p. 115414, Sep 2008.
- [43] J. Lefebvre and P. Finnie, “Excited excitonic states in single-walled carbon nanotubes,” *Nano Letters*, vol. 8, no. 7, pp. 1890–1895, 2008. PMID: 18505302.
- [44] T. Hertel, V. Perebeinos, J. Crochet, K. Arnold, M. Kappes, and P. Avouris, “Inter-subband decay of 1-d exciton resonances in carbon nanotubes,” *Nano Letters*, vol. 8, no. 1, pp. 87–91, 2008. PMID: 18069868.
- [45] S. Lebedkin, F. Hennrich, O. Kiowski, and M. M. Kappes, “Photophysics of carbon nanotubes in organic polymer-toluene dispersions: Emission and excitation satellites and relaxation pathways,” *Phys. Rev. B*, vol. 77, p. 165429, Apr 2008.
- [46] T. Ando, “Effects of valley mixing and exchange on excitons in carbon nanotubes with aharonovbohm flux,” *Journal of the Physical Society of Japan*, vol. 75, no. 2, p. 024707, 2006.

- [47] H. Zhao and S. Mazumdar, "Electron-electron interaction effects on the optical excitations of semiconducting single-walled carbon nanotubes," *Phys. Rev. Lett.*, vol. 93, p. 157402, Oct 2004.
- [48] W. Zhou, D. Nakamura, H. Liu, H. Kataura, and S. Takeyama, "Relative ordering between bright and dark excitons in single-walled carbon nanotubes," *Sci. Rep.*, vol. 4, p. 6999, Nov. 2014.
- [49] J. L. Blackburn, J. M. Holt, V. M. Irurzun, D. E. Resasco, and G. Rumbles, "Confirmation of k-momentum dark exciton vibronic sidebands using ^{13}C -labeled, highly enriched (6,5) single-walled carbon nanotubes," *Nano Letters*, vol. 12, no. 3, pp. 1398–1403, 2012. PMID: 22313425.
- [50] A. Hagen, G. Moos, V. Talalaev, and T. Hertel, "Electronic structure and dynamics of optically excited single-wall carbon nanotubes," *Applied Physics A*, vol. 78, pp. 1137–1145, May 2004.
- [51] M. Jones, C. Engtrakul, W. K. Metzger, R. J. Ellingson, A. J. Nozik, M. J. Heben, and G. Rumbles, "Analysis of photoluminescence from solubilized single-walled carbon nanotubes," *Phys. Rev. B*, vol. 71, p. 115426, Mar 2005.
- [52] J. Crochet, M. Clemens, and T. Hertel, "Quantum yield heterogeneities of aqueous single-wall carbon nanotube suspensions," *Journal of the American Chemical Society*, vol. 129, no. 26, pp. 8058–8059, 2007. PMID: 17552526.
- [53] A. Hagen, M. Steiner, M. B. Raschke, C. Lienau, T. Hertel, H. Qian, A. J. Meixner, and A. Hartschuh, "Exponential decay lifetimes of excitons in individual single-walled carbon nanotubes," *Phys. Rev. Lett.*, vol. 95, p. 197401, Oct 2005.
- [54] S.-Y. Ju, W. P. Kopcha, and F. Papadimitrakopoulos, "Brightly fluorescent single-walled carbon nanotubes via an oxygen-excluding surfactant organization," *Science*, vol. 323, no. 5919, pp. 1319–1323, 2009.
- [55] Y. Miyauchi, H. Hirori, K. Matsuda, and Y. Kanemitsu, "Radiative lifetimes and coherence lengths of one-dimensional excitons in single-walled carbon nanotubes," *Phys. Rev. B*, vol. 80, p. 081410, Aug 2009.
- [56] C. Georgi, N. Hartmann, T. Gokus, A. A. Green, M. C. Hersam, and A. Hartschuh, "Photoinduced luminescence blinking and bleaching in individual single-walled carbon nanotubes," *ChemPhysChem*, vol. 9, no. 10, pp. 1460–1464, 2008.
- [57] D. M. Harrah, J. R. Schneck, A. A. Green, M. C. Hersam, L. D. Ziegler, and A. K. Swan, "Intensity-dependent exciton dynamics of (6,5) single-walled carbon nanotubes: Momentum selection rules, diffusion, and nonlinear interactions," *ACS Nano*, vol. 5, no. 12, pp. 9898–9906, 2011. PMID: 22077149.

- [58] T. Hertel, S. Himmelein, T. Ackermann, D. Stich, and J. Crochet, "Diffusion limited photoluminescence quantum yields in 1-d semiconductors: Single-wall carbon nanotubes," *ACS Nano*, vol. 4, no. 12, pp. 7161–7168, 2010. PMID: 21105744.
- [59] S. Moritsubo, T. Murai, T. Shimada, Y. Murakami, S. Chiashi, S. Maruyama, and Y. K. Kato, "Exciton diffusion in air-suspended single-walled carbon nanotubes," *Phys. Rev. Lett.*, vol. 104, p. 247402, Jun 2010.
- [60] S. Mouri, Y. Miyauchi, and K. Matsuda, "Dispersion-process effects on the photoluminescence quantum yields of single-walled carbon nanotubes dispersed using aromatic polymers," *The Journal of Physical Chemistry C*, vol. 116, no. 18, pp. 10282–10286, 2012.
- [61] L. Cognet, D. A. Tsyboulski, J.-D. R. Rocha, C. D. Doyle, J. M. Tour, and R. B. Weisman, "Stepwise quenching of exciton fluorescence in carbon nanotubes by single-molecule reactions," *Science*, vol. 316, no. 5830, pp. 1465–1468, 2007.
- [62] K. Yoshikawa, K. Matsuda, and Y. Kanemitsu, "Exciton transport in suspended single carbon nanotubes studied by photoluminescence imaging spectroscopy," *The Journal of Physical Chemistry C*, vol. 114, no. 10, pp. 4353–4356, 2010.
- [63] J. J. Crochet, J. G. Duque, J. H. Werner, and S. K. Doorn, "Photoluminescence imaging of electronic-impurity-induced exciton quenching in single-walled carbon nanotubes," *Nat Nano*, vol. 7, pp. 126–132, Feb. 2012.
- [64] Y. Murakami and J. Kono, "Nonlinear photoluminescence excitation spectroscopy of carbon nanotubes: Exploring the upper density limit of one-dimensional excitons," *Phys. Rev. Lett.*, vol. 102, p. 037401, Jan 2009.
- [65] T. Koyama, Y. Miyata, H. Kishida, H. Shinohara, and A. Nakamura, "Photophysics in single-walled carbon nanotubes with (6,4) chirality at high excitation densities: Bimolecular auger recombination and phase-space filling of excitons," *The Journal of Physical Chemistry C*, vol. 117, no. 4, pp. 1974–1981, 2013.
- [66] S. Ghosh, S. M. Bachilo, R. A. Simonette, K. M. Beckingham, and R. B. Weisman, "Oxygen doping modifies near-infrared band gaps in fluorescent single-walled carbon nanotubes," *Science*, vol. 330, no. 6011, pp. 1656–1659, 2010.
- [67] Y. Miyauchi, M. Iwamura, S. Mouri, T. Kawazoe, M. Ohtsu, and K. Matsuda, "Brightening of excitons in carbon nanotubes on dimensionality modification," *Nat Photon*, vol. 7, pp. 715–719, Sept. 2013.
- [68] A. H. Brozena, J. D. Leeds, Y. Zhang, J. T. Fourkas, and Y. Wang, "Controlled defects in semiconducting carbon nanotubes promote efficient generation and luminescence of trions," *ACS Nano*, vol. 8, no. 5, pp. 4239–4247, 2014. PMID: 24669843.

- [69] Y. Piao, B. Meany, L. R. Powell, N. Valley, H. Kwon, G. C. Schatz, and Y. Wang, “Brightening of carbon nanotube photoluminescence through the incorporation of sp³ defects,” *Nat Chem*, vol. 5, pp. 840–845, Oct. 2013.
- [70] J. Ramirez, M. L. Mayo, S. Kilina, and S. Tretiak, “Electronic structure and optical spectra of semiconducting carbon nanotubes functionalized by diazonium salts,” *Chemical Physics*, vol. 413, no. Supplement C, pp. 89 – 101, 2013. Photophysics of carbon nanotubes and nanotube composites.
- [71] N. F. Hartmann, K. A. Velizhanin, E. H. Haroz, M. Kim, X. Ma, Y. Wang, H. Htoon, and S. K. Doorn, “Photoluminescence dynamics of aryl sp³ defect states in single-walled carbon nanotubes,” *ACS Nano*, vol. 10, no. 9, pp. 8355–8365, 2016. PMID: 27529740.
- [72] J. Mu, Y. Ma, H. Yin, C. Liu, and M. Rohlfing, “Photoluminescence of single-walled carbon nanotubes: The role of stokes shift and impurity levels,” *Phys. Rev. Lett.*, vol. 111, p. 137401, Sep 2013.
- [73] J. Lefebvre, J. Fraser, Y. Homma, and P. Finnie, “Photoluminescence from single-walled carbon nanotubes: a comparison between suspended and micelle-encapsulated nanotubes,” *Applied Physics A*, vol. 78, pp. 1107–1110, May 2004.
- [74] C. Fantini, A. Jorio, M. Souza, M. S. Strano, M. S. Dresselhaus, and M. A. Pimenta, “Optical transition energies for carbon nanotubes from resonant raman spectroscopy: Environment and temperature effects,” *Phys. Rev. Lett.*, vol. 93, p. 147406, Sep 2004.
- [75] M. Rohlfing, “Redshift of excitons in carbon nanotubes caused by the environment polarizability,” *Phys. Rev. Lett.*, vol. 108, p. 087402, Feb 2012.
- [76] N. Ai, W. Walden-Newman, Q. Song, S. Kalliakos, and S. Strauf, “Suppression of blinking and enhanced exciton emission from individual carbon nanotubes,” *ACS Nano*, vol. 5, no. 4, pp. 2664–2670, 2011. PMID: 21375256.
- [77] P. Finnie and J. Lefebvre, “Photoinduced band gap shift and deep levels in luminescent carbon nanotubes,” *ACS Nano*, vol. 6, no. 2, pp. 1702–1714, 2012. PMID: 22308958.
- [78] M. S. Dresselhaus, A. Jorio, A. G. Souza Filho, and R. Saito, “Defect characterization in graphene and carbon nanotubes using raman spectroscopy,” *Philosophical Transactions of the Royal Society of London A: Mathematical, Physical and Engineering Sciences*, vol. 368, no. 1932, pp. 5355–5377, 2010.
- [79] A. C. Ferrari and D. M. Basko, “Raman Spectroscopy as a Versatile Tool for Studying the Properties of Graphene,” *Nat. Nanotechnol.*, vol. 8, pp. 235–246, 2013.

- [80] J. Wang, J. Yang, D. Zhang, and Y. Li, "Structure dependence of the intermediate-frequency raman modes in isolated single-walled carbon nanotubes," *The Journal of Physical Chemistry C*, vol. 116, no. 44, pp. 23826–23832, 2012.
- [81] P. T. Araujo, S. K. Doorn, S. Kilina, S. Tretiak, E. Einarsson, S. Maruyama, H. Chacham, M. A. Pimenta, and A. Jorio, "Third and fourth optical transitions in semiconducting carbon nanotubes," *Phys. Rev. Lett.*, vol. 98, p. 067401, Feb 2007.
- [82] S. Doorn, D. Heller, P. Barone, M. Usrey, and M. Strano, "Resonant raman excitation profiles of individually dispersed single walled carbon nanotubes in solution," *Applied Physics A*, vol. 78, pp. 1147–1155, May 2004.
- [83] S. Uryu and T. Ando, "Exciton absorption of perpendicularly polarized light in carbon nanotubes," *Phys. Rev. B*, vol. 74, p. 155411, Oct 2006.
- [84] Y. Miyauchi, M. Oba, and S. Maruyama, "Cross-polarized optical absorption of single-walled nanotubes by polarized photoluminescence excitation spectroscopy," *Phys. Rev. B*, vol. 74, p. 205440, Nov 2006.
- [85] A. G. Souza Filho, A. Jorio, G. Dresselhaus, M. S. Dresselhaus, R. Saito, A. K. Swan, M. S. Ünlü, B. B. Goldberg, J. H. Hafner, C. M. Lieber, and M. A. Pimenta, "Effect of quantized electronic states on the dispersive raman features in individual single-wall carbon nanotubes," *Phys. Rev. B*, vol. 65, p. 035404, Dec 2001.
- [86] F. Tuinstra and J. L. Koenig, "Raman spectrum of graphite," *The Journal of Chemical Physics*, vol. 53, no. 3, pp. 1126–1130, 1970.
- [87] R. Vidano, D. Fischbach, L. Willis, and T. Loehr, "Observation of raman band shifting with excitation wavelength for carbons and graphites," *Solid State Communications*, vol. 39, no. 2, pp. 341 – 344, 1981.
- [88] M. Lucchese, F. Stavale, E. M. Ferreira, C. Vilani, M. Moutinho, R. B. Capaz, C. Achete, and A. Jorio, "Quantifying ion-induced defects and raman relaxation length in graphene," *Carbon*, vol. 48, no. 5, pp. 1592 – 1597, 2010.
- [89] A. G. Souza Filho, A. Jorio, A. K. Swan, M. S. Ünlü, B. B. Goldberg, R. Saito, J. H. Hafner, C. M. Lieber, M. A. Pimenta, G. Dresselhaus, and M. S. Dresselhaus, "Anomalous two-peak G' -band raman effect in one isolated single-wall carbon nanotube," *Phys. Rev. B*, vol. 65, p. 085417, Feb 2002.
- [90] R. Graupner, "Raman spectroscopy of covalently functionalized single-wall carbon nanotubes," *Journal of Raman Spectroscopy*, vol. 38, no. 6, pp. 673–683, 2007.
- [91] T. Fujigaya and N. Nakashima, "Non-covalent polymer wrapping of carbon nanotubes and the role of wrapped polymers as functional dispersants," *Science and Technology of Advanced Materials*, vol. 16, no. 2, p. 024802, 2015.

- [92] S. M. Fatemi and M. Foroutan, "Recent developments concerning the dispersion of carbon nanotubes in surfactant/polymer systems by md simulation," *Journal of Nanostructure in Chemistry*, vol. 6, pp. 29–40, Mar 2016.
- [93] J. L. Blackburn, "Semiconducting single-walled carbon nanotubes in solar energy harvesting," *ACS Energy Letters*, vol. 2, no. 7, pp. 1598–1613, 2017.
- [94] T. Guo, P. Nikolaev, A. Thess, D. Colbert, and R. Smalley, "Catalytic growth of single-walled nanotubes by laser vaporization," *Chemical Physics Letters*, vol. 243, no. 1, pp. 49 – 54, 1995.
- [95] M. JosYacamn, M. MikiYoshida, L. Rendn, and J. G. Santiesteban, "Catalytic growth of carbon microtubules with fullerene structure," *Applied Physics Letters*, vol. 62, no. 6, pp. 657–659, 1993.
- [96] M. F. L. De Volder, S. H. Tawfick, R. H. Baughman, and A. J. Hart, "Carbon nanotubes: Present and future commercial applications," *Science*, vol. 339, no. 6119, pp. 535–539, 2013.
- [97] J. Chen, H. Liu, W. A. Weimer, M. D. Halls, D. H. Waldeck, and G. C. Walker, "Noncovalent engineering of carbon nanotube surfaces by rigid, functional conjugated polymers," *Journal of the American Chemical Society*, vol. 124, no. 31, pp. 9034–9035, 2002. PMID: 12148991.
- [98] P. Gerstel, S. Klumpp, F. Hennrich, A. Poschlad, V. Meded, E. Blasco, W. Wenzel, M. M. Kappes, and C. Barner-Kowollik, "Highly selective dispersion of single-walled carbon nanotubes via polymer wrapping: A combinatorial study via modular conjugation," *ACS Macro Letters*, vol. 3, no. 1, pp. 10–15, 2014.
- [99] M. J. Shea, R. D. Mehlenbacher, M. T. Zanni, and M. S. Arnold, "Experimental measurement of the binding configuration and coverage of chirality-sorting polyfluorenes on carbon nanotubes," *The Journal of Physical Chemistry Letters*, vol. 5, no. 21, pp. 3742–3749, 2014. PMID: 26278744.
- [100] K. S. Mistry, B. A. Larsen, and J. L. Blackburn, "High-yield dispersions of large-diameter semiconducting single-walled carbon nanotubes with tunable narrow chirality distributions," *ACS Nano*, vol. 7, no. 3, pp. 2231–2239, 2013. PMID: 23379962.
- [101] T. Fukumaru, F. Toshimitsu, T. Fujigaya, and N. Nakashima, "Effects of the chemical structure of polyfluorene on selective extraction of semiconducting single-walled carbon nanotubes," *Nanoscale*, vol. 6, pp. 5879–5886, 2014.
- [102] O. Hiroaki, I. Natsuko, F. Tsuyohiko, N. Yasuro, and N. Naotoshi, "One-pot separation of highly enriched (6,5)-single-walled carbon nanotubes using a fluorene-based copolymer," *Chemistry Letters*, vol. 40, no. 3, pp. 239–241, 2011.

- [103] D. J. Bindl and M. S. Arnold, "Efficient exciton relaxation and charge generation in nearly monochiral (7,5) carbon nanotube/c60 thin-film photovoltaics," *The Journal of Physical Chemistry C*, vol. 117, no. 5, pp. 2390–2395, 2013.
- [104] T. Lei, X. Chen, G. Pitner, H.-S. P. Wong, and Z. Bao, "Removable and recyclable conjugated polymers for highly selective and high-yield dispersion and release of low-cost carbon nanotubes," *Journal of the American Chemical Society*, vol. 138, no. 3, pp. 802–805, 2016. PMID: 26731376.
- [105] F. Toshimitsu and N. Nakashima, "Semiconducting single-walled carbon nanotubes sorting with a removable solubilizer based on dynamic supramolecular coordination chemistry," *Nature Communications*, vol. 5, p. 5041, Oct. 2014.
- [106] E. Zaminpayma and K. Mirabbaszadeh, "Investigation of molecular interaction between single-walled carbon nanotubes and conjugated polymers," *Polymer Composites*, vol. 33, no. 4, pp. 548–554, 2012.
- [107] B. Pradhan, S. K. Batabyal, and A. J. Pal, "Electrical bistability and memory phenomenon in carbon nanotube-conjugated polymer matrixes," *The Journal of Physical Chemistry B*, vol. 110, no. 16, pp. 8274–8277, 2006. PMID: 16623507.
- [108] H. W. Lee, Y. Yoon, S. Park, J. H. Oh, S. Hong, L. S. Liyanage, H. Wang, S. Morishita, N. Patil, Y. J. Park, J. J. Park, A. Spakowitz, G. Galli, F. Gygi, P. H.-S. Wong, J. B.-H. Tok, J. M. Kim, and Z. Bao, "Selective dispersion of high purity semiconducting single-walled carbon nanotubes with regioregular poly(3-alkylthiophene)s," *Nat. Commun.*, vol. 2, p. 541, Nov. 2011.
- [109] Z. Zhang, L. Wei, X. Qin, and Y. Li, "Carbon nanomaterials for photovoltaic process," *Nano Energy*, vol. 15, no. Supplement C, pp. 490 – 522, 2015.
- [110] S. Ren, M. Bernardi, R. R. Lunt, V. Bulovic, J. C. Grossman, and S. Gradeak, "Toward efficient carbon nanotube/p3ht solar cells: Active layer morphology, electrical, and optical properties," *Nano Letters*, vol. 11, no. 12, pp. 5316–5321, 2011. PMID: 22023484.
- [111] M.-H. Ham, G. L. C. Paulus, C. Y. Lee, C. Song, K. Kalantar-zadeh, W. Choi, J.-H. Han, and M. S. Strano, "Evidence for high-efficiency exciton dissociation at polymer/single-walled carbon nanotube interfaces in planar nano-heterojunction photovoltaics," *ACS Nano*, vol. 4, no. 10, pp. 6251–6259, 2010. PMID: 20886891.
- [112] C.-K. Chang, J.-Y. Hwang, W.-J. Lai, C.-W. Chen, C.-I. Huang, K.-H. Chen, and L.-C. Chen, "Influence of solvent on the dispersion of single-walled carbon nanotubes in polymer matrix and the photovoltaic performance," *The Journal of Physical Chemistry C*, vol. 114, no. 24, pp. 10932–10936, 2010.

- [113] A. F. Nogueira, B. S. Lomba, M. A. Soto-Oviedo, C. R. D. Correia, P. Corio, C. A. Furtado, and I. A. Himmegen, "Polymer solar cells using single-wall carbon nanotubes modified with thiophene pedant groups," *The Journal of Physical Chemistry C*, vol. 111, no. 49, pp. 18431–18438, 2007.
- [114] D. J. Bindl, M.-Y. Wu, F. C. Prehn, and M. S. Arnold, "Efficiently harvesting excitons from electronic type-controlled semiconducting carbon nanotube films," *Nano Letters*, vol. 11, no. 2, pp. 455–460, 2011. PMID: 21166422.
- [115] G. I. Koleilat, M. Vosgueritchian, T. Lei, Y. Zhou, D. W. Lin, F. Lissel, P. Lin, J. W. F. To, T. Xie, K. England, Y. Zhang, and Z. Bao, "Surpassing the exciton diffusion limit in single-walled carbon nanotube sensitized solar cells," *ACS Nano*, vol. 10, no. 12, pp. 11258–11265, 2016. PMID: 28024326.
- [116] C. Li, Y. Chen, Y. Wang, Z. Iqbal, M. Chhowalla, and S. Mitra, "A fullerene-single wall carbon nanotube complex for polymer bulk heterojunction photovoltaic cells," *J. Mater. Chem.*, vol. 17, pp. 2406–2411, 2007.
- [117] Y. Chen, H. Gao, and Y. Luo, "Coaxial carbon nanotubepolythiophene core-shell nanowire for efficient hole transport in heterojunction photovoltaic device," *Applied Physics Letters*, vol. 99, no. 14, p. 143309, 2011.
- [118] S. Chaudhary, H. Lu, A. M. Miller, C. J. Bardeen, and M. Ozkan, "Hierarchical placement and associated optoelectronic impact of carbon nanotubes in polymer-fullerene solar cells," *Nano Letters*, vol. 7, no. 7, pp. 1973–1979, 2007. PMID: 17570731.
- [119] R. Radbeh, E. Parbaile, M. Chakaroun, B. Ratier, M. Aldissi, and A. Moliton, "Enhanced efficiency of polymeric solar cells via alignment of carbon nanotubes," *Polymer International*, vol. 59, no. 11, pp. 1514–1519, 2010.
- [120] R. Ihly, A.-M. Dowgiallo, M. Yang, P. Schulz, N. J. Stanton, O. G. Reid, A. J. Ferguson, K. Zhu, J. J. Berry, and J. L. Blackburn, "Efficient charge extraction and slow recombination in organic-inorganic perovskites capped with semiconducting single-walled carbon nanotubes," *Energy Environ. Sci.*, vol. 9, pp. 1439–1449, 2016.
- [121] S. N. Habisreutinger, R. J. Nicholas, and H. J. Snaith, "Carbon nanotubes in perovskite solar cells," *Advanced Energy Materials*, vol. 7, no. 10, pp. 1601839–n/a, 2017. 1601839.
- [122] L. Novotny and B. Hecht, *Principles of Nano-Optics*. Cambridge: Cambridge University Press, 2008.
- [123] P. Bharadwaj, B. Deutsch, and L. Novotny, "Optical antennas," *Adv. Opt. Photonics*, vol. 1, pp. 438–483, 2009.
- [124] L. Novotny and N. van Hulst, "Antennas for light," *Nat. Photonics*, vol. 5, pp. 83–90, 2011.

- [125] R. L. Olmon and M. B. Raschke, “Antenna-load interactions at optical frequencies: Impedance matching to quantum systems,” *Nanotechnology*, vol. 23, no. 44, p. 444001, 2012.
- [126] P. Anger, P. Bharadwaj, and L. Novotny, “Enhancement and quenching of single-molecule fluorescence,” *Phys. Rev. Lett.*, vol. 96, p. 113002, 2006.
- [127] K. B. Crozier, A. Sundaramurthy, G. S. Kino, and C. F. Quate, “Optical antennas: Resonators for local field enhancement,” *J. Appl. Phys.*, vol. 94, no. 7, pp. 4632–4642, 2003.
- [128] A. Kinkhabwala, Z. Yu, S. Fan, Y. Avlasevich, and K. M. . W. E. Moerner, “Large single-molecule fluorescence enhancements produced by a bowtie nanoantenna,” *Nat. Photonics*, vol. 3, pp. 654–657, 2009.
- [129] P. Chen, J. Liu, L. Wang, K. Jin, Y. Yin, and Z. Li, “Optimization and maximum potential of optical antennae in near-field enhancement,” *Appl. Opt.*, vol. 54, no. 18, pp. 5822–5828, 2015.
- [130] J. T. Krug, E. J. Sánchez, and X. S. Xie, “Design of near-field optical probes with optimal field enhancement by finite difference time domain electromagnetic simulation,” *J. Chem. Phys.*, vol. 116, no. 24, pp. 10895–10901, 2002.
- [131] L. Novotny, “Effective wavelength scaling for optical antennas,” *Phys. Rev. Lett.*, vol. 98, p. 266802, 2007.
- [132] L. Novotny, E. J. Snchez, and X. S. Xie, “Near-field optical imaging using metal tips illuminated by higher-order hermitegaussian beams,” *Ultramicroscopy*, vol. 71, no. 1, pp. 21 – 29, 1998.
- [133] A. L. Demming, F. Festy, and D. Richards, “Plasmon resonances on metal tips: Understanding tip-enhanced raman scattering,” *J. Chem. Phys.*, vol. 122, no. 18, p. 184716, 2005.
- [134] Z. Yang, J. Aizpurua, and H. Xu, “Electromagnetic field enhancement in ters configurations,” *J. Raman Spectrosc.*, vol. 40, no. 10, pp. 1343–1348, 2009.
- [135] I. Notingher, , and A. Elfick, “Effect of sample and substrate electric properties on the electric field enhancement at the apex of spm nanotips,” *J. Phys. Chem. B*, vol. 109, no. 33, pp. 15699–15706, 2005.
- [136] L. Aigouy, A. Lahrech, S. Grésillon, H. Cory, A. C. Boccara, and J. C. Rivoal, “Polarization effects in apertureless scanning near-field optical microscopy: an experimental study,” *Opt. Lett.*, vol. 24, pp. 187–189, Feb 1999.

- [137] N. Kazemi-Zanjani, S. Vedraïne, and F. Lagugné-Labarthet, “Localized enhancement of electric field in tip-enhanced raman spectroscopy using radially and linearly polarized light,” *Opt. Express*, vol. 21, pp. 25271–25276, Oct 2013.
- [138] T. Mino, Y. Saito, and P. Verma, “Quantitative analysis of polarization-controlled tip-enhanced raman imaging through the evaluation of the tip dipole,” *ACS Nano*, vol. 8, no. 10, pp. 10187–10195, 2014.
- [139] X. Zhang, W. Zhang, L. Liu, and Z. Shen, “Surface-enhanced raman of z-vibration mode in single-walled and multi-walled carbon nanotube,” *Chem. Phys. Lett.*, vol. 372, no. 3-4, pp. 497–502, 2003.
- [140] Y. Abate, S. Gamage, L. Zhen, S. B. Cronin, H. Wang, V. Babicheva, M. H. Javani, and M. I. Stockman, “Nanoscopy reveals metallic black phosphorus,” *Light Sci. Appl.*, vol. 5, p. e16162, June 2016.
- [141] W. Bao, N. J. Borys, C. Ko, J. Suh, W. Fan, A. Thron, Y. Zhang, A. Buyanin, J. Zhang, S. Cabrini, and P. D. Ashby, “Visualizing nanoscale excitonic relaxation properties of disordered edges and grain boundaries in monolayer molybdenum disulfide,” *Nat. Commun.*, vol. 6, p. 7993, Aug. 2015.
- [142] R. Ossikovski, Q. Nguyen, and G. Picardi, “Simple model for the polarization effects in tip-enhanced raman spectroscopy,” *Phys. Rev. B*, vol. 75, p. 045412, Jan 2007.
- [143] P. G. Gucciardi, M. Lopes, R. D eturche, C. Julien, D. Barchiesi, and M. L. de la Chapelle, “Light depolarization induced by metallic tips in apertureless near-field optical microscopy and tip-enhanced raman spectroscopy,” *Nanotechnology*, vol. 19, no. 21, p. 215702, 2008.
- [144] A. Hartschuh, E. J. S anchez, X. S. Xie, and L. Novotny, “High-resolution near-field raman microscopy of single-walled carbon nanotubes,” *Phys. Rev. Lett.*, vol. 90, p. 095503, Mar 2003.
- [145] N. Anderson, A. Hartschuh, S. Cronin, and L. Novotny, “Nanoscale vibrational analysis of single-walled carbon nanotubes,” *J. Am. Chem. Soc.*, vol. 127, no. 8, pp. 2533–2537, 2005.
- [146] K. L. A. Chan and S. G. Kazarian, “Finding a needle in a chemical haystack: Tip-enhanced raman scattering for studying carbon nanotubes mixtures,” *Nanotechnology*, vol. 21, no. 44, p. 445704, 2010.
- [147] B. Pettinger, K. F. Domke, D. Zhang, R. Schuster, and G. Ertl, “Direct monitoring of plasmon resonances in a tip-surface gap of varying width,” *Phys. Rev. B*, vol. 76, p. 113409, Sep 2007.

- [148] T. Deckert-Gaudig, E. Bailo, and V. Deckert, “Tip-enhanced raman scattering (TERS) of oxidised glutathione on an ultraflat gold nanoplate,” *Phys. Chem. Chem. Phys.*, vol. 11, pp. 7360–7362, 2009.
- [149] J. Stadler, B. Oswald, T. Schmid, and R. Zenobi, “Characterizing unusual metal substrates for gap-mode tip-enhanced raman spectroscopy,” *J. Raman Spectrosc.*, vol. 44, no. 2, pp. 227–233, 2013.
- [150] R. Zhang, Y. Zhang, Z. C. Dong, S. Jiang, C. Zhang, L. Chen, L. Zhang, Y. Liao, J. Aizpurua, Y. Luo, J. L. Yang, and J. G. Hou, “Chemical mapping of a single molecule by plasmon-enhanced raman scattering,” *Nature*, vol. 498, pp. 82–86, 2013.
- [151] S. F. Becker, M. Esmann, K. Yoo, P. Gross, R. Vogelgesang, N. Park, and C. Lienau, “Gap-plasmon-enhanced nanofocusing near-field microscopy,” *ACS Photonics*, vol. 3, no. 2, pp. 223–232, 2016.
- [152] P. Nordlander and E. Prodan, “Plasmon hybridization in nanoparticles near metallic surfaces,” *Nano Lett.*, vol. 4, no. 11, pp. 2209–2213, 2004.
- [153] B. Pettinger, P. Schambach, C. J. Villagómez, and N. Scott, “Tip-enhanced raman spectroscopy: Near-fields acting on a few molecules,” *Annu. Rev. Phys. Chem.*, vol. 63, no. 1, pp. 379–399, 2012.
- [154] H. Xu, J. Aizpurua, M. Käll, and P. Apell, “Electromagnetic contributions to single-molecule sensitivity in surface-enhanced raman scattering,” *Phys. Rev. E*, vol. 62, p. 4318, 2000.
- [155] M. Futamata, Y. Maruyama, and M. Ishikawa, “Local electric field and scattering cross section of ag nanoparticles under surface plasmon resonance by finite difference time domain method,” *J. Phys. Chem. B*, vol. 107, no. 31, pp. 7607–7617, 2003.
- [156] E. Hao and G. C. Schatz, “Electromagnetic fields around silver nanoparticles and dimers,” *J. Chem. Phys.*, vol. 120, no. 1, pp. 357–366, 2004.
- [157] K. J. Savage, M. M. Hawkeye, R. Esteban, A. G. Borisov, J. Aizpurua, and J. J. Baumberg, “Revealing the quantum regime in tunnelling plasmonics,” *Nature*, vol. 491, pp. 574–577, Nov. 2012.
- [158] R. W. Rendell and D. J. Scalapino, “Surface plasmons confined by microstructures on tunnel junctions,” *Phys. Rev. B*, vol. 24, p. 3276, Sep 1981.
- [159] M. Brack, “The physics of simple metal clusters: self-consistent jellium model and semiclassical approaches,” *Rev. Mod. Phys.*, vol. 65, pp. 677–732, Jul 1993.
- [160] W. Zhu, R. Esteban, A. G. Borisov, J. J. Baumberg, P. Nordlander, H. J. Lezec, J. Aizpurua, and K. B. Crozier, “Quantum mechanical effects in plasmonic structures with subnanometre gaps,” *Nat. Commun.*, vol. 7, p. 11495, June 2016.

- [161] R. Fuchs and F. Claro, “Multipolar response of small metallic spheres: Nonlocal theory,” *Phys. Rev. B*, vol. 35, pp. 3722–3727, Mar 1987.
- [162] A. Liebsch and W. L. Schaich, “Influence of a polarizable medium on the nonlocal optical response of a metal surface,” *Phys. Rev. B*, vol. 52, pp. 14219–14234, Nov 1995.
- [163] F. J. Garca de Abajo, “Nonlocal effects in the plasmons of strongly interacting nanoparticles, dimers, and waveguides,” *J. Phys. Chem. C*, vol. 112, no. 46, pp. 17983–17987, 2008.
- [164] J. Zuloaga, E. Prodan, and P. Nordlander, “Quantum Plasmonics: Optical Properties and Tunability of Metallic Nanorods,” *ACS Nano*, vol. 4, pp. 5269–5276, 2010.
- [165] M. Barbry, P. Koval, F. Marchesin, R. Esteban, A. G. Borisov, J. Aizpurua, and D. Sánchez-Portal, “Atomistic Near-Field Nanoplasmonics: Reaching Atomic-Scale Resolution in Nanooptics,” *ACS Nano*, vol. 15, pp. 3410–3419, 2015.
- [166] S. Trautmann, J. Aizpurua, I. Gotz, A. Undisz, J. Dellith, H. Schneidewind, M. Rettenmayr, and V. Deckert, “A classical description of subnanometer resolution by atomic features in metallic structures,” *Nanoscale*, vol. 9, pp. 391–401, 2017.
- [167] F. Benz, M. K. Schmidt, A. Dreismann, R. Chikkaraddy, Y. Zhang, A. Demetriadou, C. Carnegie, H. Ohadi, B. de Nijs, R. Esteban, J. Aizpurua, and J. J. Baumberg, “Single-molecule optomechanics in “picocavities”,” *Science*, vol. 354, no. 6313, pp. 726–729, 2016.
- [168] S. Berweger and M. B. Raschke, “Signal Limitations in Tip-Enhanced Raman Scattering: the Challenge to Become a Routine Analytical Technique,” *Anal. Bioanal. Chem.*, vol. 396, pp. 115–123, 2010.
- [169] P. Roelli, C. Galland, N. Piro, and T. J. Kippenberg, “Molecular cavity optomechanics as a theory of plasmon-enhanced raman scattering,” *Nat. Nanotechnol.*, vol. 11, pp. 164–169, 2015.
- [170] M. K. Schmidt, R. Esteban, A. González-Tudela, G. Giedke, and J. Aizpurua, “Quantum mechanical description of raman scattering from molecules in plasmonic cavities,” *ACS Nano*, vol. 10, pp. 6291–6298, 2016.
- [171] E. J. Ayars, H. D. Hallen, and C. L. Jahncke, “Electric field gradient effects in raman spectroscopy,” *Phys. Rev. Lett.*, vol. 85, p. 4180, 2000.
- [172] L. Meng, Z. Yang, J. Chen, and M. Sun, “Effect of Electric Field Gradient on Sub-nanometer Spatial Resolution of Tip-enhanced Raman Spectroscopy,” *Sci. Rep.*, vol. 5, p. 9240, 2015.

- [173] S. Duan, G. Tian, Y. Ji, J. Shao, Z. Dong, and Y. Luo, "Theoretical modeling of plasmon-enhanced raman images of a single molecule with subnanometer resolution," *J. Am. Chem. Soc.*, vol. 137, no. 30, pp. 9515–9518, 2015.
- [174] C. Zhang, B.-Q. Chen, and Z.-Y. Li, "Optical origin of subnanometer resolution in tip-enhanced raman mapping," *J. Phys. Chem. C*, vol. 119, no. 21, pp. 11858–11871, 2015.
- [175] C. Zhang, B.-Q. Chen, and Z. Y. Li, "Influence of tip geometry on the spatial resolution of tip enhanced raman mapping," *Chin. Phys. B*, vol. 25, p. 095203, 2016.
- [176] L. Novotny, R. X. Bian, and X. S. Xie, "Theory of nanometric optical tweezers," *Phys. Rev. Lett.*, vol. 79, pp. 645–648, Jul 1997.
- [177] R. Dorn, S. Quabis, and G. Leuchs, "Sharper focus for a radially polarized light beam," *Phys. Rev. Lett.*, vol. 91, p. 233901, Dec 2003.
- [178] G. Binnig and H. Rohrer, "Scanning tunneling microscopy," *Surface Science*, vol. 126, no. 1, pp. 236 – 244, 1983.
- [179] G. E. Poirier, "Characterization of organosulfur molecular monolayers on au(111) using scanning tunneling microscopy," *Chemical Reviews*, vol. 97, no. 4, pp. 1117–1128, 1997. PMID: 11851444.
- [180] B. C. Stipe, H. J. Mamin, T. D. Stowe, T. W. Kenny, and D. Rugar, "Noncontact friction and force fluctuations between closely spaced bodies," *Phys. Rev. Lett.*, vol. 87, p. 096801, Aug 2001.
- [181] J. R. Zurita-Sánchez, J.-J. Greffet, and L. Novotny, "Friction forces arising from fluctuating thermal fields," *Phys. Rev. A*, vol. 69, p. 022902, Feb 2004.
- [182] K. Karra and R. D. Grober, "Piezo-electric tuning fork tipsample distance control for near field optical microscopes," *Ultramicroscopy*, vol. 61, no. 1, pp. 197 – 205, 1995. Selected Papers from the 3rd International Conference on Near-Field Optics and Related Techniques.
- [183] Y. Joo, G. J. Brady, M. S. Arnold, and P. Gopalan, "Dose-controlled, floating evaporative self-assembly and alignment of semiconducting carbon nanotubes from organic solvents," *Langmuir*, vol. 30, no. 12, pp. 3460–3466, 2014. PMID: 24580418.
- [184] A. Nish, J.-Y. Hwang, J. Doig, and R. J. Nicholas, "Highly selective dispersion of single-walled carbon nanotubes using aromatic polymers," *Nature Nanotechnology*, vol. 2, p. 640, Sept. 2007.
- [185] J. M. Kinder and E. J. Mele, "Nonradiative recombination of excitons in carbon nanotubes mediated by free charge carriers," *Phys. Rev. B*, vol. 78, p. 155429, Oct 2008.

- [186] T. Liu and Z. Xiao, “Exact and closed form solutions for the quantum yield, exciton diffusion length, and lifetime to reveal the universal behaviors of the photoluminescence of defective single-walled carbon nanotubes,” *The Journal of Physical Chemistry C*, vol. 115, no. 34, pp. 16920–16927, 2011.
- [187] M. S. Hofmann, J. No, A. Kneer, J. J. Crochet, and A. Hgele, “Ubiquity of exciton localization in cryogenic carbon nanotubes,” *Nano Letters*, vol. 16, no. 5, pp. 2958–2962, 2016. PMID: 27105355.
- [188] X. Ma, O. Roslyak, J. G. Duque, X. Pang, S. K. Doorn, A. Piryatinski, D. H. Dunlap, and H. Htoon, “Influences of exciton diffusion and exciton-exciton annihilation on photon emission statistics of carbon nanotubes,” *Phys. Rev. Lett.*, vol. 115, p. 017401, Jul 2015.
- [189] X. Ma, L. Adamska, H. Yamaguchi, S. E. Yalcin, S. Tretiak, S. K. Doorn, and H. Htoon, “Electronic structure and chemical nature of oxygen dopant states in carbon nanotubes,” *ACS Nano*, vol. 8, no. 10, pp. 10782–10789, 2014. PMID: 25265272.
- [190] T. Inaba and Y. Homma, “Atmospheric ions as the origin of photoinduced degrading of photoluminescence from a single-walled carbon nanotube,” *Applied Physics Letters*, vol. 107, no. 7, p. 071907, 2015.
- [191] R. Matsunaga, Y. Miyauchi, K. Matsuda, and Y. Kanemitsu, “Symmetry-induced nonequilibrium distributions of bright and dark exciton states in single carbon nanotubes,” *Phys. Rev. B*, vol. 80, p. 115436, Sep 2009.
- [192] H. Maki, T. Sato, and K. Ishibashi, “Direct observation of the deformation and the band gap change from an individual single-walled carbon nanotube under uniaxial strain,” *Nano Letters*, vol. 7, no. 4, pp. 890–895, 2007. PMID: 17358091.
- [193] A. Ozao, S. Chiashi, S. Watanabe, G. Yamaguchi, H. Kato, and Y. Homma, “Gold deposition effects on photoluminescence and raman scattering spectra of suspended single-walled carbon nanotubes,” *Japanese Journal of Applied Physics*, vol. 54, no. 5, p. 055102, 2015.
- [194] L. Valkunas, Y.-Z. Ma, and G. R. Fleming, “Exciton-exciton annihilation in single-walled carbon nanotubes,” *Phys. Rev. B*, vol. 73, p. 115432, Mar 2006.
- [195] K. Matsuda, T. Inoue, Y. Murakami, S. Maruyama, and Y. Kanemitsu, “Exciton dephasing and multiexciton recombinations in a single carbon nanotube,” *Phys. Rev. B*, vol. 77, p. 033406, Jan 2008.
- [196] M. Zheng, A. Jagota, M. S. Strano, A. P. Santos, P. Barone, S. G. Chou, B. A. Diner, M. S. Dresselhaus, R. S. Mclean, G. B. Onoa, G. G. Samsonidze, E. D. Semke, M. Usrey, and D. J. Walls, “Structure-based carbon nanotube sorting by sequence-dependent dna assembly,” *Science*, vol. 302, no. 5650, pp. 1545–1548, 2003.

- [197] R. R. Johnson, A. T. C. Johnson, and M. L. Klein, “Probing the structure of dnanarbon nanotube hybrids with molecular dynamics,” *Nano Letters*, vol. 8, no. 1, pp. 69–75, 2008. PMID: 18069867.
- [198] J. Xie, T. Inaba, R. Sugiyama, and Y. Homma, “Intrinsic diffusion length of excitons in long single-walled carbon nanotubes from photoluminescence spectra,” *Phys. Rev. B*, vol. 85, p. 085434, Feb 2012.
- [199] E. L. Elson and D. Magde, “Fluorescence correlation spectroscopy. i. conceptual basis and theory,” *Biopolymers*, vol. 13, no. 1, pp. 1–27, 1974.
- [200] X. Shi, N. Coca-Lpez, J. Janik, and A. Hartschuh, “Advances in tip-enhanced near-field raman microscopy using nanoantennas,” *Chemical Reviews*, vol. 117, no. 7, pp. 4945–4960, 2017. PMID: 28212025.
- [201] C. Xie, C. Mu, J. R. Cox, and J. M. Gerton, “Tip-enhanced fluorescence microscopy of high-density samples,” *Applied Physics Letters*, vol. 89, no. 14, p. 143117, 2006.
- [202] P. G. Gucciardi, G. Bachelier, and M. Allegrini, “Far-field background suppression in tip-modulated apertureless near-field optical microscopy,” *Journal of Applied Physics*, vol. 99, no. 12, p. 124309, 2006.
- [203] B. D. Mangum, C. Mu, and J. M. Gerton, “Resolving single fluorophores within dense ensembles: contrast limits of tip-enhanced fluorescence microscopy,” *Opt. Express*, vol. 16, pp. 6183–6193, Apr 2008.
- [204] J. M. Gerton, L. A. Wade, G. A. Lessard, Z. Ma, and S. R. Quake, “Tip-enhanced fluorescence microscopy at 10 nanometer resolution,” *Phys. Rev. Lett.*, vol. 93, p. 180801, Oct 2004.
- [205] T. aki Yano, T. Ichimura, A. Taguchi, N. Hayazawa, P. Verma, Y. Inouye, and S. Kawata, “Confinement of enhanced field investigated by tip-sample gap regulation in tapping-mode tip-enhanced raman microscopy,” *Applied Physics Letters*, vol. 91, no. 12, p. 121101, 2007.
- [206] B. D. Mangum, E. Shafran, C. Mu, and J. M. Gerton, “Three-dimensional mapping of near-field interactions via single-photon tomography,” *Nano Letters*, vol. 9, no. 10, pp. 3440–3446, 2009. PMID: 19711903.
- [207] C. Hppener, R. Beams, and L. Novotny, “Background suppression in near-field optical imaging,” *Nano Letters*, vol. 9, no. 2, pp. 903–908, 2009.
- [208] Z. Yang, J. Aizpurua, and H. Xu, “Electromagnetic field enhancement in ters configurations,” *Journal of Raman Spectroscopy*, vol. 40, no. 10, pp. 1343–1348, 2009.
- [209] Y. Blanter and M. Bttiker, “Shot noise in mesoscopic conductors,” *Physics Reports*, vol. 336, no. 1, pp. 1 – 166, 2000.

-
- [210] C. Schnenberger and S. F. Alvarado, "A differential interferometer for force microscopy," *Review of Scientific Instruments*, vol. 60, no. 10, pp. 3131–3134, 1989.

Acronyms

0D	zero-dimensional
1D	one-dimensional
2D	two-dimensional
AFM	atomic force microscopy
APD	avalanche photo diode
ATPE	aqueous two-phase extraction
BIPV	building-integrated photovoltaics
BS	beam splitter
BWF	Breit-Wigner-Fano
BZ	Brillouin zone
CB	conduction band
CCD	charged coupled device
CoMoCat	cobalt-molybdenum catalyst
CTAB	cetyltrimethylammonium bromide
CVD	chemical vapor deposition
DGU	density gradient ultracentrifugation
DOS	density of states

EL	electroluminescence
FET	field-effect transistor
FM	flippable mirror
FWHM	full width half maximum
HiPCO	high pressure carbon monoxide
i	in-plane
IR	infrared
LED	light emitting diode
LF	line filter
LO	longitudinal optical
LSPR	localized surface plasmon resonance
MD	molecular dynamic
NA	numerical aperture
NF	notch filter
NIR	near infrared
OSC	organic solar cell
PALM	photoactivated localization microscopy
PC	photocurrent
PH	pinhole
PL	photoluminescence
PLL	phase-locked-loop

QY	quantum yield
RBM	radial breathing mode
SDS	sodium dodecyl sulfate
SERS	surface-enhanced Raman scattering
SNOM	scanning near-field optical microscopy
SPE	selective polymer extraction
SPM	scanning probe microscope
s-SNOM	scattering scanning near-field optical microscopy
STED	stimulated emission depletion microscopy
STM	scanning tunneling microscopy
STORM	stochastic optical reconstruction microscopy
SWCNT	single-walled carbon nanotube
TDDFT	time-dependent density functional theory
TEM	transmission electron microscopy
TENOM	tip-enhanced near-field optical microscopy
TERS	tip-enhanced Raman scattering
TMDC	transition metal dichalcogenide
TO	transverse optical
TTL	transistor-transistor logic
VB	valence band
vHs	van-Hove singularity

List of Figures

1.1	Construction of a (6,5) SWCNT unit cell by rolling up a rectangular stripe of graphene with chiral vector \vec{C}_h , translation vector \vec{T} and the graphene lattice vectors \vec{a}_1 and \vec{a}_2	6
1.2	a) Real space lattice of graphene, b) Reciprocal space lattice of graphene.	8
1.3	The first Brillouin zone of (4,2) nanotube.	9
1.4	a) Electronic energy dispersion relation of graphene in the first Brillouin zone with nearest neighbour tight-binding approximation, b) Linear energy dispersion relation near dirac point.	12
1.5	Zone-folding approach for a (3,3) nanotube.	13
1.6	a) Conductivity of different chiralities of SWCNTs. b)- d) SWCNTs can be divided into 3 types: metallic, semiconducting type I and semiconducting type II.	14
1.7	Energy bands and corresponding density of states of a) a metallic (6,6) SWCNT and b) a semiconducting (5,0) SWCNT.	16
1.8	Kataura plot: transition energies E_{ii} as a function of $1/d_t$	17
1.9	Selection rules for transitions in semiconducting SWCNTs depending on the incident light polarization.	18
1.10	Schematic of SWCNT band structure with a substantial E_b , different exciton energy levels for one sub-band transition and multiple exciton states corresponding to different sub-bands.	19
1.11	Exciton fine structures.	20
1.12	Illustration of Aryl sp^3 defected SWCNTs.	22
1.13	Stokes and anti-Stokes Raman Scattering.	23
1.14	Energy level diagrams of non-resonant and resonant Raman Scattering.	24
1.15	Typical Raman spectrum of semiconducting SWCNTs.	26
2.1	Schematic of light propagation from a single point source.	33
2.2	Illustration of the Abbe limit in optical microscopy.	35
2.3	Characteristics of an optical antenna.	37
2.4	The tip modifies the polarization of the incoming field.	39
2.5	The dependence of lateral confinement w on tip-sample distance d in simulation.	40
2.6	Schematics of optomechanical systems.	46

2.7	Schematics of electric field and electric field gradient intensity distribution in the plane between the tip and substrate in TERS configuration.	47
3.1	A sketch of the confocal microscope setup.	51
3.2	Generation of a radially polarized beam and its field distributions.	53
3.3	Schematic of the shear-force feedback system for tip-sample distance control.	54
3.4	Schematic diagram of gold tip fabrication and SEM image of a sharp gold tip.	56
4.1	Confocal PL and near-field Raman, PL, topography images of PFO-BPy sorted CoMoCAT (6,5) SWCNTs.	58
4.2	Confocal PL and near-field Raman, PL and topography images of PFO-BPy sorted CVD (6,5) SWCNTs.	60
4.3	Confocal PL and near-field Raman, PL and topography images of DNA wrapped CoMoCAT (6,5) SWCNTs.	61
4.4	A qualitative illustration of exciton localization in SWCNTs.	62
4.5	An example of near-field PL intensity heterogeneity analysis.	63
4.6	A typical PL peak of (6,5) SWCNT at room temperature.	64
4.7	The C_v values of individual nanotubes from different samples.	65
4.8	Near-field PL images of a PFO-BPy SWCNT consecutively recorded at roughly 2 mW/ μm^2 excitation intensity.	67
4.9	The length of PL quenched segments yields information about the exciton diffusion range.	68
4.10	Autocorrelation curves of the scan series on the SWCNT in Figure 4.8.	69
5.1	The presence of far-field background signal in near-field images.	72
5.2	The schemes of conventional and new tuning fork-tip configurations.	73
5.3	The schematic of the lock-in amplifier connections.	74
5.4	Lock-in detection of the near-field PL of a SWCNT.	75
5.5	Near-field measurements on a single SWCNT with the new configuration.	76
5.6	PL approach curve and its correlation with the periodic tuning fork signal in our experiment.	78
5.7	The operation of tunable switch.	79
5.8	Experimental setup with the switch.	80
5.9	An illustration of the parameters used in the calculation.	81
5.10	Calculated S and S/dS against the modulation depth Z_{mod} and the switch threshold Z_t/Z_{mod} when $I_{DC} = 0$	81
5.11	Calculated signal to noise ratio S/dS against the modulation depth Z_{mod} and the switch threshold Z_t/Z_{mod} under different dark count levels.	82
5.12	Calculated signal to noise ratio S/dS against the modulation depth Z_{mod} and the switch threshold Z_t/Z_{mod} with different smallest tip-sample distance l.	83
5.13	Calculated signal to noise ratio S/dS against the modulation depth Z_{mod} and the switch threshold Z_t/Z_{mod} with different near-field decay length L.	84

5.14 Extraction and subsequent subtraction of far-field signal on SWCNT PL imaging.	85
---------------------------------------------------------------------------------------------	----

List of Publications

During the course of my PhD research, the following peer-reviewed papers have been published:

- Harald Budde, Nicolás Coca-López, Xian Shi, Richard Ciesielski, Antonio Lombardo, Duhee Yoon, Andrea C. Ferrari, Achim Hartschuh, „Raman Radiation Patterns of Graphene“, *ACS Nano* 10, 1756 (2016).
- Xian Shi, Nicolás Coca-López, Julia Janik, Achim Hartschuh, „Advances in Tip-Enhanced Near-Field Raman Microscopy Using Nanoantennas“, *Chemical Reviews* 117(7), 4945 (2017).
- Xian Shi, Image Namal, Kerstin Müller, Matthias Kastner, Tobias Hertel, Achim Hartschuh, „Optical Homogeneity Analysis of Single-walled Carbon Nanotube/Polymer Conjugates by Tip-enhanced Near-field Optical Microscopy“, In preparation.

List of Conferences

- POCAONTAS first meeting, Madrid (Spain), 11.12. - 12.12.2013
Oral Presentation: Near-field Optical and Electro-Optical Probing of Polymer-SWCNT
- POCAONTAS summer school, Ventotene (Italy), 01.06. - 06.06.2014
Oral Presentation: Tip-Enhanced Optical Microscopy of SWCNTs
- CeNS Workshop Venice 2014, San Servolo (Italy), 21.09. - 26.09.2014
Poster: Tip-enhanced Raman Spectroscopy (TERS) - Excitation Power Dependence?
- POCAONTAS mid-term meeting, Madrid (Spain), 04.11.2014
Oral Presentation: Near-field Optical and Electro-Optical Probing of Polymer-SWCNT
- DPG Frühjahrstagung 2015, Berlin (Germany), 15.03. - 20.03.2015
Oral Presentation: Near-field Optical Imaging of (6,5) SWCNT/PFO-BPy Conjugates
- POCAONTAS scientific panel meeting, Madrid (Spain), 27.04 - 30.04.2015
Oral Presentation: Near-field Optical Imaging of (6,5) SWCNT/PFO-BPy Conjugates
- WONTON 2015, Kloster Banz (Germany), 31.05. - 04.06.2015
Poster: Near-field Optical Imaging of (6,5) SWCNT/PFO-BPy Conjugates
- POCAONTAS winter school, London (UK), 25.01 - 29.01.2016
Oral Presentation: Near-field Optical Imaging of (6,5) SWCNT/PFO-BPy Conjugates
- POCAONTAS scientific panel meeting, Würzburg (Germany), 03.04 - 08.04.2016
Oral Presentation: Near-field Optical Imaging of (6,5) SWCNT/PFO-BPy Conjugates
- WNMO 2016, Niederstetten (Germany), 04.10. - 06.10.2016
Oral Presentation and Poster: Separate the near-field from far-field: Tip-sample distance modulation
- ICES 2017, Munich (Germany), 04.09. - 07.09.2017
Poster: Separate the near-field from far-field: Tip-sample distance modulation

Acknowledgements

First of all, I would like to thank my advisor **Prof. Dr. Achim Hartschuh** for accepting me into the group and his support and guidance all these years. He is not only an excellent physicist but also a very nice and friendly person. I learned a lot in his group and enjoyed the time I spent here.

I also want to thank **Prof. Dr. Tobias Hertel** for kindly providing good quality samples for my measurement and being my co-advisor for the thesis and defense. My thanks also goes to **Dr. Larry Lüer** for his coordination of POCAONTAS network.

I especially thank my former colleagues **Harald Budde**, **Nina Mauser** and **Tobia Mancabelli** for their help. I did my first project with Harry and learned basic experimental operations from him. Nina guided me in my first few near-field measurements and introduced a lot of things to me. After Nina graduated, I benefited a lot from the discussions with Tobia.

I thank **Nico** and **Richard** for all the fun we had. My big thanks also goes to other working colleagues **Alberto**, **Nicolai**, **Julia**, **Veit**, **Frank**, **Matthias**, **Irene**, **Kathi**, **Alex** for their support.

I'm also grateful to our secretary **Römling Rita**. She is always friendly, helpful and never impatient.

I'm thankful to my parents for their encouragement and love in my life. I also thank my wife, Lijing Yu for entering my life and making it so colorful. Particularly I wanna thank my grandma, with whom I grew up before going to school. Although she passed away nearly 5 years ago, I hope she can see all of this somewhere.